Multifunctional Micro-Scale Sensors for Water Safety Monitoring with Only Bare Platinum Electrodes

by

Wen-Chi Lin

A dissertation submitted in partial fulfillment
of the requirements for the degree of
Doctor of Philosophy
(Chemical Engineering)
in the University of Michigan
2017

Doctoral Committee:

      Professor Mark A. Burns, Chair
      Professor Ronald G. Larson
      Professor Levi T. Thompson
      Professor Euisik Yoon

Wen-Chi Lin

wclin@umich.edu

ORCID iD: 0000-0002-5444-4657

DEDICATION

To my beloved friends and family, and those in need.

ACKNOWLEDGEMENTS

TABLE OF CONTENTS

LIST OF FIGURES

LIST OF TABLES

ABSTRACT

End-point monitoring at home is crucial to secure water safety because water can be contaminated in the drinking water distribution system (DWDS), like the Flint water crisis in 2014. The contamination can come from overgrown algae, pipe corrosion, or even pipe leakage from construction vibration. Though end-point monitoring is crucial, it is still not practical for most users to have home water monitoring device. Water safety analysis involves a number of variables, and a single variable can not represent the quality of water. Thus water monitoring typically performed using multiple sensors, which cost $100 each and the total cost is around thousands. The total size, cost, and the maintenance difficulties of the water sensors are still barriers for most families to secure water safety.

This dissertation develops an integrated practical micro-scale sensor for water monitoring. The sensor can measure seven important variables: flow-rate, temperature, ionic conductivity, pH, oxidation-reduction-potential (ORP), lead ions, and other heavy metal ions. The flow-rate, temperature and ionic conductivity sensors are optimized from previous technology. These sensors are simplified for low fabrication cost and easy integration. The flow rate and temperature sensors are capable of measuring 0.5-2.0 GPM in 10-50 ℃. The conductivity sensor can measure 0-8000 µS/cm in 10-50 ℃ water. The pH, ORP, lead, and other heavy metal ions sensors are developed with original methods. These sensors require no reference electrodes, sample pre-treatment, surface labeling through chemical reactions, or

membrane coating. The sensors measure the targeted ions by controlling the surface reactions on simple platinum electrodes. The pH and ORP sensor can measure pH 4 to 10 and ORP 200 to 800 mV simultaneously with only bare platinum electrodes. The four-electrode heavy metal sensor can distinguish lead from other heavy metals. The sensor is capable of being embedded in the DWDS and detecting Pb at action level (15 ppb). All of the seven sensors presented in this dissertation are composed of only a single layer PVD Ti/Pt. Due to the simple structure and fabrication, the sensors can be easily integrated, and the entire device costs only about 10 cents.

This dissertation demonstrates a method to achieve end-point water monitoring at home. The simple structure of these sensors make them promising for long-term applications under strong hydraulic force. The lead and other heavy metal sensors are also operated two months to validate the possibility of long-term monitoring. Though these sensors are not optimized for energy consumption and response time yet, this dissertation presents promising, unique, and practical sensors designed for residential water monitoring.

CHAPTER 1

Introduction

1.1 The Difficulties in Water Monitoring

Water monitoring is a research area of considerable importance in both developing [1] and developed countries [2], because ideal water monitoring is not easy to achieve. Water monitoring typically performed using multiple sensors since the analysis involves a number of variables. A single variable can not represent the quality of water, thus multiple variables need to be monitored simultaneously. Each variable requires a separate meter and these conventional sensors are usually costly and hard to maintain. The total size, cost, and the maintenance difficulties of the water quality sensors make end-point monitoring at the consumers' side not practical.

End-point monitoring is crucial for the safety of the users, though water monitoring at the end-point is a great challenge. Many people consider water in developed countries is safe, but water contamination commonly occurs downstream the water treatment plants. In the other word, though the water leaving the treatment plants is clean and safe, it may get contaminated in the service lines. End-point monitoring at home is necessary to ensure the water safety. As described above, the overall size and cost of water sensors are too much for most family because it is

necessary to consider several variables simultaneously to achieve meaningful analysis. The development of scalable, stable, and versatile integrated sensors that can be widely applied is needed.

Ideal water sensors also need to be strong and long lasting with little maintenance. Water monitoring sensors need to be distributed to the entire water distribution system for effective monitoring. Because industrial contamination and pipe corruption can happen at anywhere in the distribution system, the sensors should be installed in upstream and downstream through the service pipes. Even inside a user's house, the sensors should be installed at every water outlet. This is especially important for heavy metal detection or any other contamination from pipe corruption. The heavy metal leakage, such as toxic Pb, can only be detected downstream the corruption. That is, if you installed a Pb sensor in the kitchen you will never know if there is a Pb leakage in the bathroom. Due to the number of the sensors should be installed, it is not practical to maintain or change the sensors regularly like conventional water sensors needed. Moreover, water-monitoring sensors are operated in complicated environment containing microorganisms and strong chemical under strong hydraulic force. The sensors need to be really robust or they can be easily deactivated or destroyed.

The other challenge is the tradeoff between the sensor performance and the cost [3]. Water sensors must be affordable to most families for meaningful applications. Water is considered cheap in most developed countries, so it is not attracting for most family to buy an expensive equipment for water. Moreover, one family probably needs more than 10 sensors in a living unit as described above, but there is a tradeoff between the sensitivity and the senor cost. Sensitive minimized sensors usually require complicated fabrication steps, thus the fabrication cost of these sensors are relatively high. These complicated sensors are also usually very fragile.

As described in the previous paragraph, it is crucial to keep the sensor simple for practical operation. Long-lasting sensors with acceptable sensitivity based on simple and cost effective fabrication methods are desired.

1.2 The Goals and Contribution of this Dissertation

This thesis focuses on developing an ideal sensor for end-point water monitoring. The thesis focuses on the possibility to minimize and integrate multiple crucial sensors for water safety onto a single device by using only bare platinum electrodes. The thesis focuses on seven crucial variables: flow-rate, temperature, conductivity, pH, oxidation reduction potential (ORP), lead, and other heavy metal ions. The final device is about the size of a rice grain, and the small size ensures the sensor can be easily installed into pipes, swimming pools, or bathtubs to offer real-time water quality measurements. With only minor adjustment, it is also possible to use in chemical pipes, which are common in the industry. The sensor is about 10 cents to fabricate and if mass-produced, the entire device should cost less than a dollar.

The final device will equip the multi-function micron-scale sensors and use a Bluetooth module and a coin cell to offer continuous, on-time signal. It can also use Radio-frequency identification (RFI) to provide information only when needed. Implementation of the project idea is shown in Figure 1.1: the small multi-functional sensors are attached in the fluid pipe. The pipe wall protects the Bluetooth and coin cell module, which are attached to the backside of the sensor. The sensors proposed in this thesis can be a possible method for long-term monitoring at home to secure water safety.
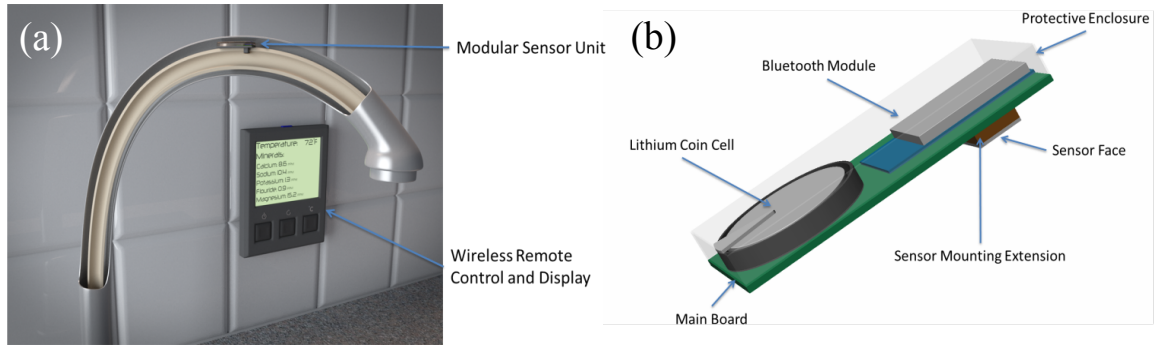
Figure 1.1 Illustration of project idea: (a) the integrated sensor can be inserted into residential pipe with its small size, and the monitored variables are displayed on the panel. (b) The entire module with Bluetooth and coin cell.

1.3 Organization of this Dissertation

This dissertation will primarily discuss the development of the prototype water sensors. The overview of Chapter 1 is the introduction of water monitoring. Chapter 1 covers the need and challenges in the field. Chapter 2 extends the discussion in Chapter 1 by introducing the previous work of other researchers. Previous research in flow-rate, temperature, conductivity, pH, ORP, lead, and other heavy metals sensing is discussed to validate the contribution of this dissertation.

The experimental design and results are presented in Chapter 3 to Chapter 6. Chapter 3 presents flow-rate and temperature sensor based on thermal resistance by both COMSOL simulation and experiment. The sensors achieve high sensitivity by changing sensor surface area, substrate material, and supplied power. Two identical sensors were fabricated on each device with an upstream sensor functioning as a temperature sensor, and the voltage difference between the two sensors indicating the water flow rate. The sensors were constructed on glass substrates, chosen for their low price, efficient thermal isolation, and compatibility with current water supply systems. The variation of water temperature of the flowing fluid from 10 to 50 ˚C was accounted for by normalizing the voltage readings. The dimensions of the sensors ranged from

71 μm by 80 μm to 430 μm by 480 μm with the smaller sensors having a higher sensitivity. Sensitivity also increased with increasing input power up to the point when boiling occurred. The optimized sensor, which was 71 μm by 80 μm on a 3 mm by 3 mm glass substrate, could be operated with only 2.75 mW of power in 10 to 50 ˚C water, providing an economic and energy efficient method to measure large water flow rates of 0.1-0.5 gallon per minute (GPM).

Conductivity, pH, and ORP are measured with the same sensor, which is composed of only bare platinum electrodes. The performance of the conductivity measurement is described in Chapter 4 and the pH and ORP measurement is presented in Chapter 5. The sensor can measure conductivity up to 8000 μS/cm at 10-50˚C, and the sensor can also measure pH from 4-10 while simultaneously measuring ORP from 150-800 mV. All of these measurements can be made even if the water samples contain common ions found in residential water.

Chapter 6 presents heavy metal sensors that have strong affinity to lead ions and suitable for long-term monitoring. Leakage of lead and other heavy metals into drinking water is a significant health risk and one that is not easily detected. The two-electrode sensor can identify the existence of a variety of heavy metals in drinking water, and the four-electrode sensor can distinguish lead from other heavy metals in solution. No false-positive response is generated when the sensors are placed in simulated and actual tap water contaminated by heavy metals. Lead detection on the four-electrode sensor is not affected by the presence of common ions in tap water. Experiment results suggest the sensors can be embedded in water service lines for long time use until lead or other heavy metals are detected.

Chapter 7 concludes the dissertation and contains both reflections on work done and a look toward future directions for the work presented. All of the sensors presented in this paper contain only platinum electrodes on glass substrate thus they are easy to be integrated and cheap

to fabricate. The overall sensor is inexpensive (*i.e.* ~$0.10/unit) with sensing area below 1 mm^2, suggesting that the unit is cost-efficient, robust, and widely applicable. The inert materials of the sensor suggest there is no theoretical lifetime of the sensor. Overall, this dissertation primarily presents a possible solution for water quality long-term monitoring.

CHAPTER 2

Background and Related Work

2.1 Flow Rate and Temperature Detection in Turbulent Liquid

Thermal flow sensors are chosen among various micro-sized flow-rate sensing methods. Micron-sized flow rate devices can be classified as three categories: magnetic, ultrasonic or thermal sensors. Measurements collected via magnetic methods will be drifted by ion concentration and pH value. Since these properties are not stable in residential water, choosing a flow rate measurement related to magnetic methods is unwise. On the other hand, the performance of ultrasonic sensors is determined by pipe size, particle size, and concentration limitations. Versatile ultrasonic sensors are thus hard to design. Therefore, thermal sensors are chosen in this dissertation.

Micro-fabricated thermal flow sensors have attracted considerable interest recently due to their small size, low power consumption, easy installation, and low per unit cost (less than a dollar if mass-produced). Thermal flow-rate sensors can be divided into three categories: time of flight, hot wire, and calorimetric [4]. Time of flight methods sense travel time for a heated bolus of fluid over a set distance [5]. These sensors are restricted in velocity measurements by data collection rates, and, in practice, their highest velocity detection is on the order of 10 cm/s. However, they have the advantage of directional detection of flow. Hot wire sensors detect the

flow rate directly by changes in heater resistance. In most applications, these sensors cannot measure the direction of flow. Calorimetric sensors, ones that measure the temperature distribution around a heater, can detect the direction of the flow [6], [7].

Previous research in flow rate sensors has focused on calorimetric and hot wire methods measuring aerodynamic flow and small liquid flow in laminar region at the level of µl/min or ml/min [4], [8]–[11]. Shikada et al. have adapted micro-fabricated flow rate sensors for large-scale air flow, which is about 800 L/s (Figure 2.1(a)(b)) [12], [13]. Others have developed a lower limit of a few nanoliters per minute (Figure 2.1(c)) [8], most of which are fluid temperature dependent. To compensate for the influence of fluid temperature, Ma *et al.* integrated a temperature sensor with the flow sensor [14], and the device worked successfully for air flow measurements. Koizumi et al. presented a fluid temperature-independent flow rate sensor, but it was only suitable over a small range (0.13-1.0 ml/min of water [4]).
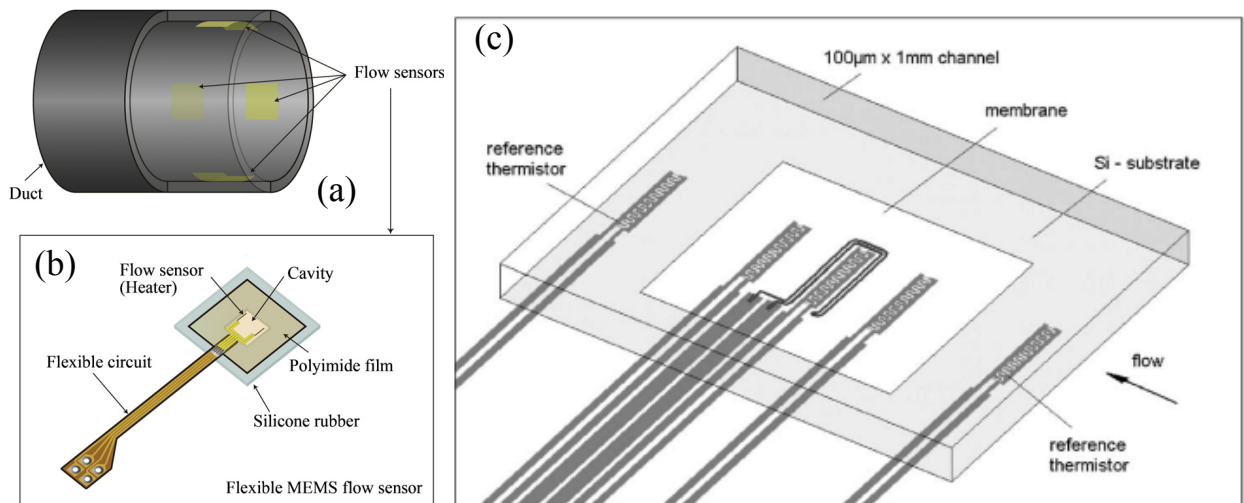
Figure 2.1 (a) The installation and (b) sensor schematic of the thermal flow meter for large air flow by Shikada et al [13]. (c) The schematic of flow sensor designed for small liquid flow in micro-channel by Ernst et al [8].

Many of these sensors could have wide-spread use in applications such as municipal water supplies or chemical production facilities. However, flow rates on the order of GPM are

common in these applications, and micro-fabricated flow sensors are rarely studied in this range. Aleksic et al. presented a flow sensor suitable for such flows, but the sensor was 25.4 mm by 6.35 mm and consumed 0.3-0.5 W of power [15]. Here we present a simple, cheap, small, and low-power sensor for high flow-rate liquid measurement. Using the micro thermal-capacitance technique, the sensor can measure water flow rates on the order of GPM in water temperatures of 10-50 ˚C translating to velocities of 10-250 cm/s. These flow rates and velocities in a one-inch-diameter pipe are common conditions in residential water supply systems.

2.2 Ionic Conductivity Measurement for Residential Water

Ionic conductivity represents the total dissolved solids (TDS) in water. Higher conductivity represents more dissolved solids and worse quality. According to EPA, the TDS of drinking water should be less than 500 mg/L, which translates to a conductivity of around 800 µS/cm. Swimming pools, on the other hand, are not considered dangerous until their conductivity exceeds 4000 µS/cm. Generally, increased conductivity can represent industrial pollution, pipe corrosion, and low flow or stale condition. Since conductivity of water change with temperature, temperature monitoring is an important variable related to conductivity measurement.

Conductivity sensors can be divided into two categories: electrodes [16], [17]or inductive sensors [18]. Electrode conductivity sensors measure conductivity, σ, directly by measuring the impedance of the water. The geometry of the sensor must be designed to match the targeted conductivity region [19]. Inductive conductivity sensors contain two coils. The first coil generates an electric current and the second coil detects the induced current, which is proportional to the conductivity of the solution. Between the two categories, electrode

conductivity sensor is more common in micro-scale sensor for its simple structure and wide measurement range.

Though scaled-down electrode conductivity sensor have been developed [16], there is a strong need to research the possibility of integrating conductivity sensors and other water quality sensors. Micron conductivity sensors can be achieved with two or four parallel platinum electrodes. AC voltage with high frequency is applied to the electrodes to avoid electrolysis, and the average current passing through the electrodes is positive relative to conductivity. Some applications cover the electrodes with dielectric layers to avoid direct contact while the others use bare Pt electrodes.

In this dissertation, a conductivity sensor with two bare platinum electrodes is designed. The sensor shared the same geometry with the pH and ORP sensor, so the same sensor can measure all of the three variables. The simple structure of the sensor implies the sensor can be fabricated in a small cost and be easily integrated with other sensors.

2.3 pH and ORP Measurement with Bare Platinum Electrodes

The pH and ORP of water are important indicators for water quality. Though the water pH value may be influenced by the local geology and some other factors, a sudden pH decrement commonly represents industrial pollution, overgrown algae, and pipe corrosion. ORP represents the overall ability of the ions to be reduced in the water. A sudden increment of ORP commonly implies industrial pollutions that strong oxidants are released into the water. According to United States Environmental Protection Agency (EPA), the ORP of drinking water should be around 250 mV and the pH should be 6.5 to 8.5. The ORP of swimming pools should be above 650 mV for disinfection. There are many other examples (e.g., aqueous process flow streams) for which accurate measurements would be beneficial.

The conventional pH and ORP sensors are electrochemical sensors, which are open circuits connecting a reference electrode and a sensing electrode. The potential on the sensing electrode changes with the pH or ORP, and the reference electrode offers a stable potential as a reference the potential change. The ORP-sensing electrode is commonly a bare platinum electrode, while the pH-sensing electrode is a Ag/AgCl electrode protected by H^+ permeable glass.

The development of micro-scale pH and ORP sensors is limited by the instability of micro-scale reference electrodes. Previous studies have focused on developing stable Ag/AgCl solid-state reference electrodes (SSREs), but Ag/AgCl SSREs have limited lifetimes because the deposited AgCl electrodes eventually dissolve into the test solutions [20]. The lifetime of the SSREs can be extended by using barrier layers over the deposited AgCl to lower the AgCl dissolution rate [21]–[23]. Substantial research has also focused on the identification of new stable SSRE chemistries [24]–[26] but most of them still require membranes to block the interfering ions from the solution.

The other challenging component other than SSRE is the pH sensing chemistries because the pH sensor has to be insensitive to the environment except for the existence of hydronium ions. Some researchers focus on pH sensitive antimony [27] or Ir/IrO_2 electrodes [24], [28], and other researchers focus on silicon nanowire pH sensors [29]–[31]. Though trade-offs between sensitivity and stability of silicon nanowires is commonly observed [30], silicone nanowires draw great attention for their fast response and high sensitivity [31]. Despite the great accuracy, these pH sensing chemistries still need a stable SSRE with long lifetime. The other approach is the development of a conductive membrane of which the electric resistance changes with pH

[32], [33]. This chemiresistor pH sensor requires no reference electrode but the sensitivity is relatively low [3].
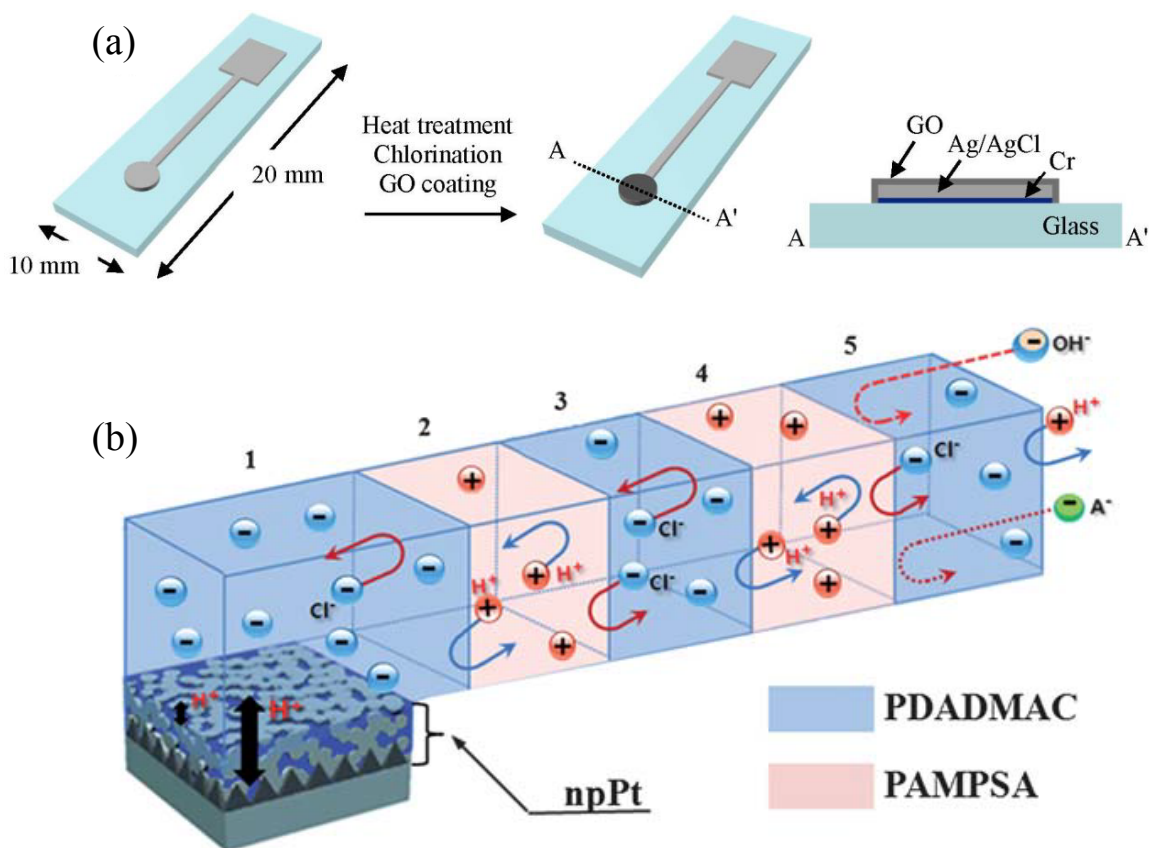
Figure 2.2 The SSRE achieved by (a) graphene oxide coated Ag/AgCl [21] and (b) polymer [26] nanoporous Pt electrodes

This dissertation presents a sensing method that only requires three simple platinum electrodes to detect conductivity, ORP, and pH of water. The electrodes on our sensor require no membranes or nanostructure and contain only a single layer of PVD Ti/Pt. The sensor controls the surface reactions on the electrode to perform the measurement. This label-free sensor is the first and only using the unique technology requiring no chemical to target specific ions. The relatively simple fabrication suggests low cost of the sensors, and the units can be easily integrated with other devices. The small area of the three electrodes (< 1 mm^2) and robust materials suggest that this sensor is suitable to be embedded at the end-points in the service lines.

Since scalable, cost-efficient, end-point monitoring with few maintenance is crucial for water safety, the method proposed is a potential approach for water monitoring.

2.4 Heavy Metal Sensors Focus On Lead Detection with only Bare Platinum Electrodes

Heavy metals such as lead in drinking water are dangerous to humans, and regulations for the maximum allowable concentrations of these metals in the water have been established to protect consumers. Lead causes neurological damage even at low levels of lead exposure, especially in infants and children [34][35][36]. The Environmental Protection Agency (EPA) states that zero lead is allowed in maximum contaminant level (MCL), and 15 ppb of lead is listed as the action level [37][38]. In addition to lead, copper is another dangerous heavy metal that causes liver and kidney damage after long-term exposure. The MCL for copper is 1.3 mg/L and the secondary maximum contaminant levels (SMCL) is 1.0 mg/L [39]. SMCLs suggest ions that cause bad taste, color, and order should be minimized in drinking water. Zinc and iron are other two common elements in drinking water that are regulated by SMCLs of 5 mg/L and 0.3 mg/L, respectively [39].

Lead leakage into tap water is a major concern in the US [36][40][41]. Houses in the US built before 1986 commonly contain lead in the service lines or valves. When water flows through the lead components, lead can leach into the water through a variety of complex electrochemical, geochemical, and hydraulic mechanisms [36][42]. The leaching often occurs without the awareness of the users because lead can be colorless and odorless. Thus users are at risk from lead exposure through contaminated water if the metal contaminant is not detected.

Early detection of lead is important to prevent long-term exposure but is difficult to achieve using current technology. Because water is contaminated inside the structure of a house,

end-point detection by home-monitoring is crucial for lead leakage detection. The only qualified method suggested by EPA is inductively coupled plasma mass spectrometry (ICPMS) at qualified national testing labs. Since lead leakage typically happens unexpectedly, the suggested method requires the self-awareness of the users to regularly send the water out for examination. As such, several researchers have been developing minimized sensors that are suitable for home-monitoring through electrochemical potentialmetric [43]–[46], colorimetric [47], [48], and chemiresistor sensor [49]. Nevertheless, most potentialmetric sensors have short lifetimes due to the limitation of minimized reference electrodes. Colorimetric and chemiresistor sensors are typically single use. There is still a strong need to develop a lead detector that can operate for a long time without input from the users.

The ideal sensor for lead detection needs to be long lasting, strong, and cheap. The sensor needs to be inserted into the pipes for years until lead leakage happens. The sensor needs to inform the users automatically without regular examination. As discussed in chapter 1, it is not practical to maintain the sensors because the sensors need to be inserted in every end point of water service line. Further, Toxic lead exposure through drinking water commonly occurs in old houses belong to families with low income. The cost of the sensor must be affordable for most families.

This dissertation presents sensors that cost less than 10 cents and are only about the size of a rice grain (~1 mm^3). The small size of the sensors allows them to be inserted in pipes, and they require only simple circuits and two AAA batteries for operation. The sensor separates lead ions by controlling the electrochemical reactions instead of pre-treated with lead-targeting ligands. The sensor is the first and only using this unique technology to monitor heavy metal ions

without ligands. The sensors are made with inert platinum electrodes, and experimental results suggest the sensors are suitable for long-term monitoring.

CHAPTER 3

Flow Rate and Temperature Detection in Turbulent Liquid

3.1 Sensor Fabrication and Experimental Methods

This section describes the experimental detail and fabrication methods of the flow rate and temperature sensor. The section includes the setup of COMSOL simulation, the fabrication of the sensor, and the experimental setup for the flow rate measurement.

3.1.1   Setup of COMSOL Simulation

The simulation was done with COMSOL version 4.3.0.184 operated on OSX version 10.9.2. The simulation was modified from the COMSOL non-isothermal flow package for turbulent flow. All material properties were imported form the COMSOL library. The Geometry was composed of 6mm wide and 2.9 mm tall water, and a 3 mm wide and 499 μm tall substrate on the top of which is a 3 mm wide, 1 μm thick film. The thin film was composed of five glass rectangles. Their lower boundaries were defined as boundary heat sources. The silicon and glass substrates were 499 μm thick. Fabricated film substrate was a combination of 1 μm nitride and 498 μm thick air. Heat transfer of film and substrate was defined as heat transfer in solid. The left boundary of the water was defined as an inlet with constant temperature. Turbulent water from 0.062 m/s to 0.248 m/s velocity entered the region. The velocity was 0.5-2.0 GPM in a 1 in

diameter pipe. The right boundary was defined as outlet with heat outflow, and upper and lower boundaries were defined as open boundaries.

In the simulation comapring the influence of substrates, the boundary heaters were 100 µm long and 2 mm apart from each other. Upstream and downstream sensors were provided with 5 W/m and 50 W/m power per length, which was equal to 0.5 mW and 5 mW for 100 µm wide sensors. Initial temperature was 30 °C. In the simulation comapring the influence of sensor size, the length of the heaters were 50 ,100, 200, 300 and 400 mm. In the influence of water-temperature test, the heaters were 50 mm long.

3.1.2 The Fabrication of Flow Rate and Temperature Sensor

RTDs made of Ti/Pt 300/1000 Å were deposited on glass wafer and protected by PECVD 1 µm glass film and 40 nm nitride film. Two identical heaters, 2 mm apart from each other, were aligned in the direction of flow on each probe. The upstream RTD worked as a temperature sensor and the downstream RTD worked as a flow rate sensor. The sensors were fabricated into the five different sizes shown in Table 3.1. The voltage on each RTD was measured as output. Sensor resistances at different temperatures were measured with a multimeter to calculate the temperature coefficient of resistance (TCR), which should be 0.15 to 0.25 % and depends on the deposited thickness of platinum. The TCR of XS sensor was 0.24 %.

Table 3.1 The resistance size of the flow and temperature sensor

Size	XS	S	M	L	XL
Longitude (µm)	71	107.5	215	320	430
Width (µm)	80	120	240	350	480

3.1.3 The Experimental Setup of Flow Rate and Temperature Detection

The schematic of the test setup was shown in Figure 3.1. Each probe was put into a one-inch-diameter pipe connected with a digital flow rate meter, a valve, and a circulating bath. Data was collected in different flow rate or flowing water temperature and repeated three times. The voltage difference of the two sensors was chosen to measure flow rate and avoid drift. The upstream temperature sensor was supplied with 0.5 mW.
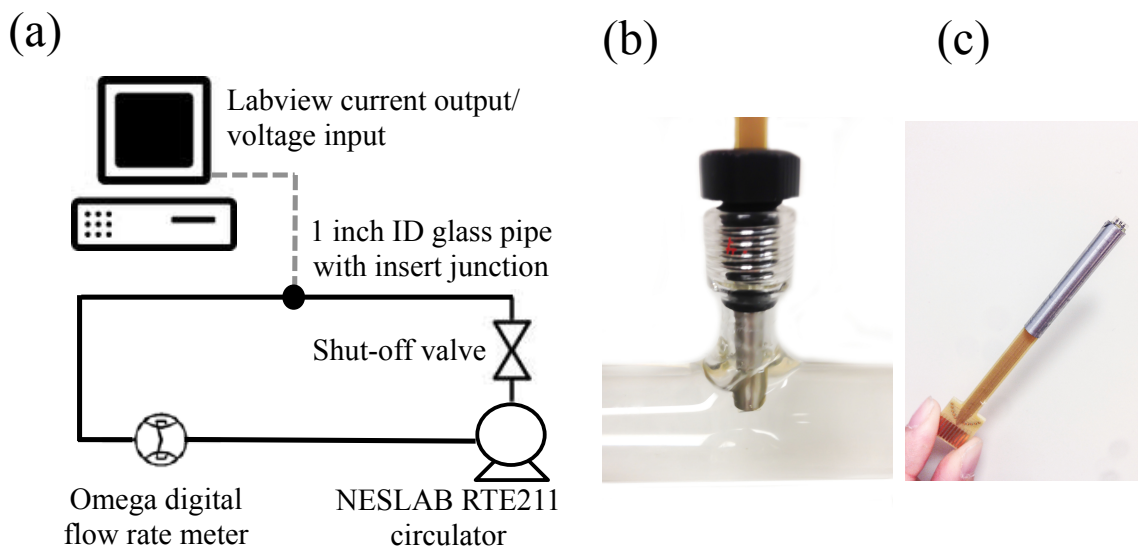
Figure 3.1 (a) The schematic of the experiment setup, (b) the glass tube insert junction, and (c) the integrated sensor probe.

The water temperature and input power of the downstream RTD varied in different testings. For heater size optimization, each probe was put in 30 °C flowing water and tested between 0.5-2.0 GPM. The upstream temperature sensor was supplied with constant 0.5 mW while the downstream flow rate sensor was supplied with 5 mW with constant DC current. For different water temperature tests, the XS probe was supplied 0.5 mW and 2.75 mW and exposed to 10, 20, 30, 40, and 50 ˚C water. Each experiment was repeated three times at each flow rate.

3.2 Heat Transfer Analysis of Micro-scale Thermal Flow Sensor

3.2.1 General Operation of Thermal Flow Rate Sensor
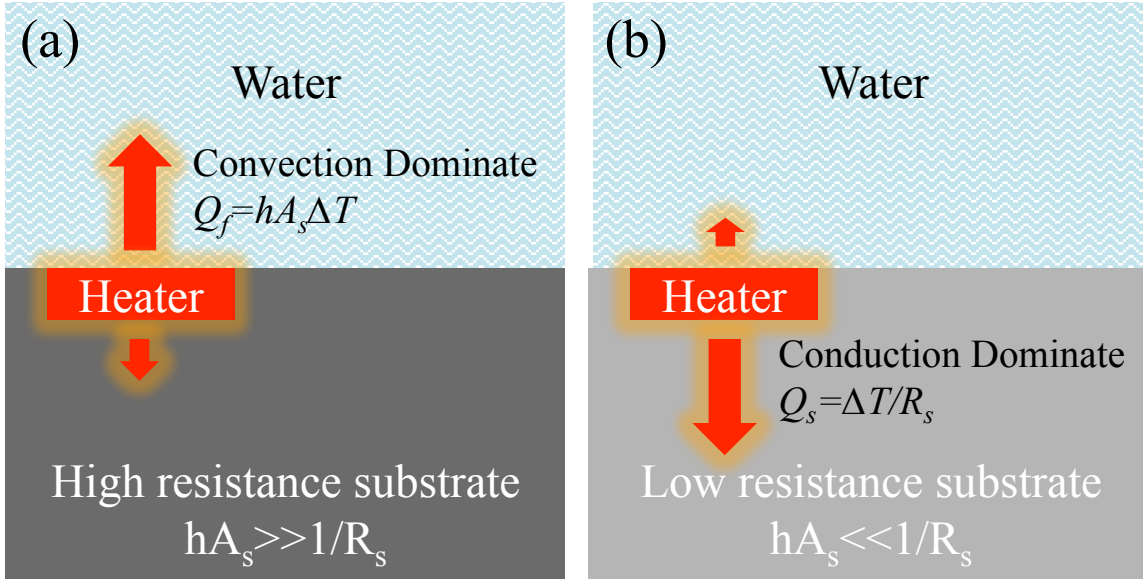
Figure 3.2 (a) Convection dominant and (b) Conduction dominant heat transfer.

Heat transfer on micro-scale thermal flow sensors is analyzed in this section to design high sensitivity flow rate sensor. The temperature difference, ΔT, between the heater on the sensor and the flowing fluid is an indication of the liquid flow rate. As shown in Figure 3.2, when the heater is supplied with a constant power, P, this power is equal to the convective heat flux transferred to the flowing fluid, Q_f, plus the conductive heat flux transferred to the substrate, Q_s. The Nusselt number (i.e., the ratio of convective to conductive heat transfer) varies from 30 to 150 in this system, and, thus, the conductive heat flux transferred to the flowing fluid can be neglected. Q_f and Q_s can thus be defined by Equations 3.1 and 3.2：

$$Q_f = hA_s\Delta T \tag{3.1}$$

$$Q_s = \frac{\Delta T}{R_s} \tag{3.2}$$

in which h is heat transfer coefficient, A_s is the heater size, and Rs is the substrate thermal resistance. ΔT is therefore defined by Equation 3.3:

$$\Delta T = \frac{P}{\dfrac{1}{R_s} + hA_s} \qquad (3.3)$$

where R_s is defined as:

$$R_s = \frac{L}{kA_c} \qquad (3.4)$$

with k being the thermal conductive coefficient, L the distance to the edge of the substrate, and A_c the cross section area of the substrate.

A large value for R_s (i.e., small Q_s) is necessary for the sensor to function [10]. As shown in Figure 3.2(a), when R_s is large, Q_f is much larger than Q_s, the first term of the denominator in Equation 3.3 is much smaller than the second term, and ΔT is dominated by convective heat transfer. Given that h is highly dependent on the liquid velocity, ΔT becomes a direct indicator of the flow rate. Note that, as shown in Figure 3.2(b), if R_s is small, which means Q_f is much smaller than Q_s, ΔT would be independent of the flow rate.

3.2.2   Conductive Heat Transfer of the Sensor Substrates

The necessary high R_s value can be achieved through either material selection or microstructure fabrication. Material selection decreases k and microstructure fabrication decreases A_c, and they both increase R_s. For material selection, two common materials of 500 μm, the typical wafer thickness, were investigated and simulated: silicon and glass, with k values of 130 W/m.K and 1.38 W/m.K and thermal resistances of 3.5 K/W and 338 K/W, respectively. For microstructure fabrication, a thin film of 1 μm nitride was selected. With a k value of 18.5 W/m.K (not as insulating as glass), the R_s of the film is around 105 K/W with a small A_c.
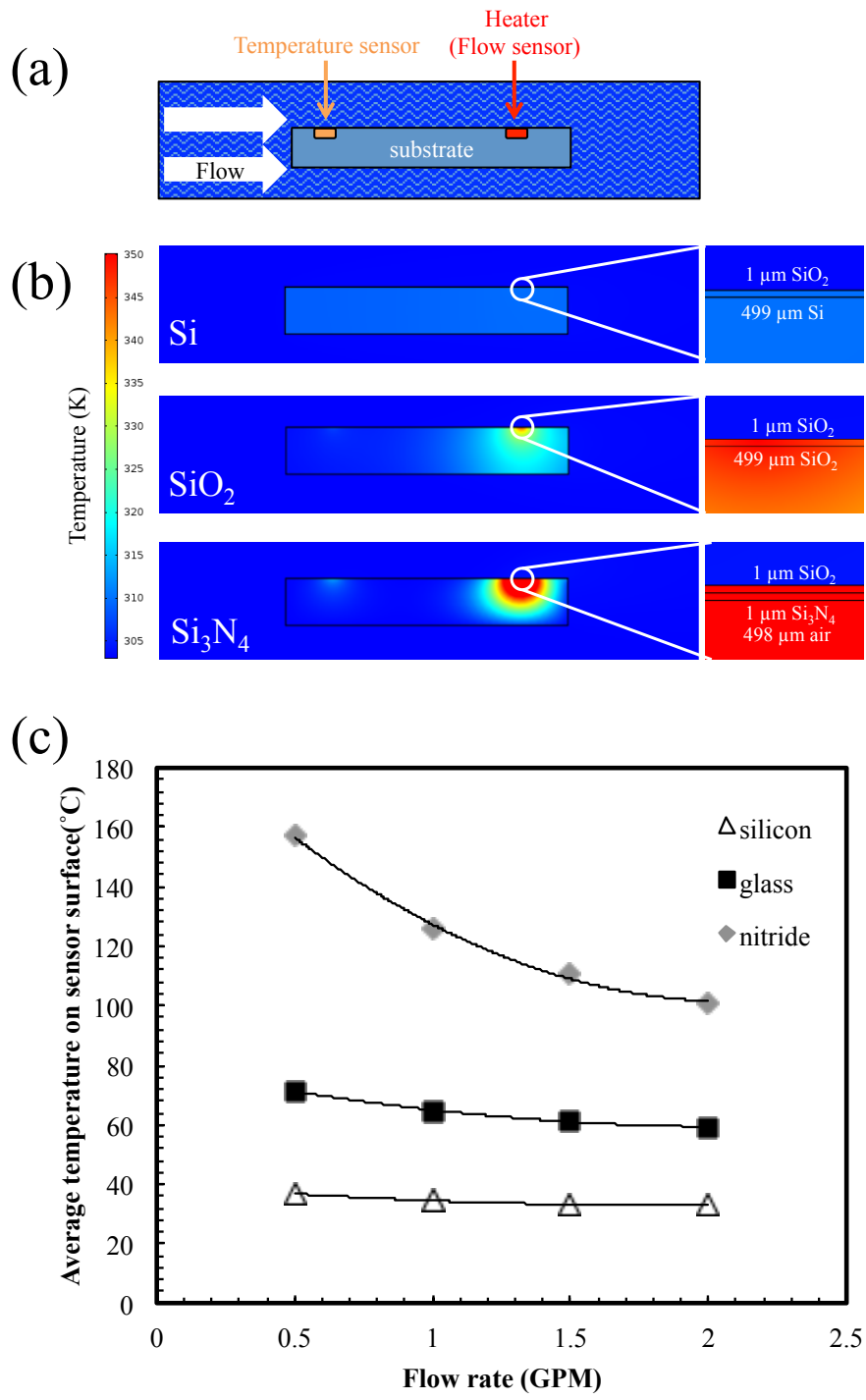
Figure 3.3 (a) The schematic of the sensor (b) The temperature field at 0.5 GPM and (c) The correlation of heater temperature and flow rate of COMSOL simulation on different substrate.

As expected, the glass substrate performed much better than the silicon substrate. The influence of substrate materials is illustrated in a steady state 2D COMSOL simulation, as shown in Figure 3.3. Figure 3.3(a) is the schematic of the simulated sensors. Figure 3.3(b) illustrates the temperature distribution at 0.5 GPM while Figure 3.3(c) demonstrates the sensitivity, or the rate the temperature changes due to changes in the flow rate. In both Figure 3.3(b) and (c), glass was preferable to silicon because it produced greater temperature changes. Further, silicon wafers need pre-deposition of an oxide film for electrical isolation. Using glass substrates improves device sensitivity and is also relatively inexpensive. The nitride thin film performed best, but production of this type of sensor is money- and time-intensive. Based on these results, their low price, and their compatibility with current water supply systems, we chose glass wafers for our experimental studies.

3.3 Results and Discussion of the Flow Rate and Temperature Detection

3.3.1   Influence of the Resistor Thermal Detector (RTD) Surface Area

A smaller heater improves the device sensitivity and results in a higher ΔT in Equation 3.3. Figure 3.4 illustrates the correlation between the silmulated temperature on the sensor surface and A_s. Smaller sensors reached higher surface temperatures, resulting in a greater ΔT between the sensor and the flowing fluid. The temperature on the upstream temperature sensors changed 10 times smaller than the temperature on the downstream flow rate sensors. The temperature sensors that were 2000 μm away from the flow sensors were independent of water flow rate and, thus, could be used to measure water temperature.
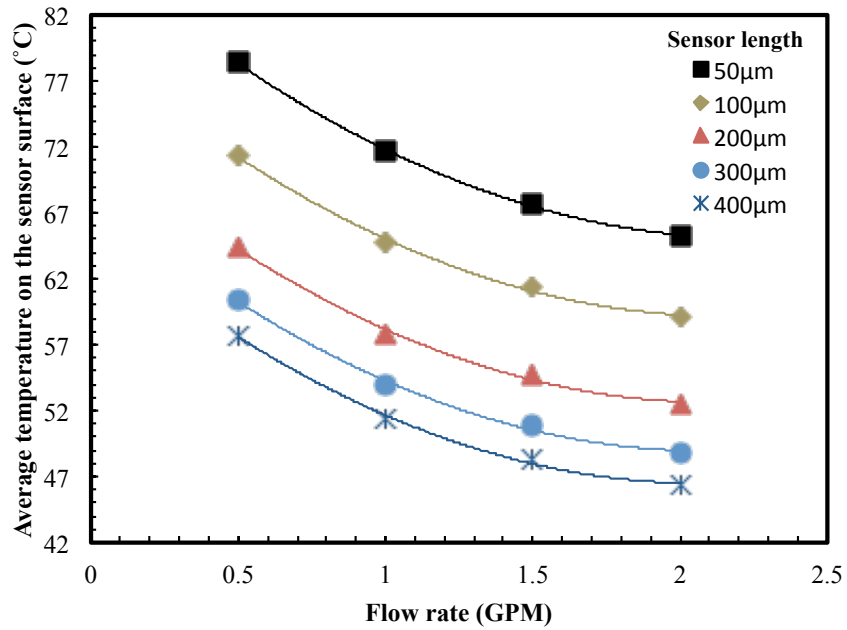
Figure 3.4 The temperature on the sensor surfaces in COMSOL simulation in various water flow-rate. The heaters were supplied with 50 W/m
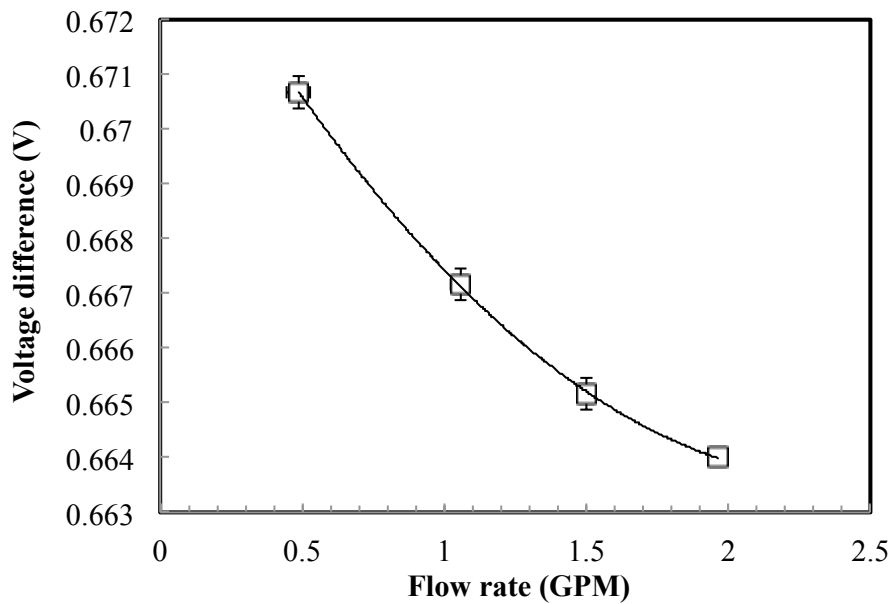
Figure 3.5 The experimental flow-rate sensing with XS sensor in 30°C water

The experimental results matched the simulations and indicated that smaller heaters improve device sensitivity for a given power input. The experimetal results using the XS probe are shown in Figure 3.5. As expected, higher flow rates produced lower voltage differences between the temperature sensor and the flow-rate sensor, thus allowing calculation of the flow rate. Fig 3.6**.**(a) illustrates the correlation between heater size and sensitivity using simulations, and Fig 3.6**.**(b) shows the experimental results. Although the 2D simulation is not an accurate representation of the experimental situation, both the simulation and experiments showed sensitivity decreasing with increasing sensor size. Sensitivity was defined by Equation 3.5, in which ΔV is the voltage difference change, V_{avg} is the average voltage difference, and ΔQ is the flow-rate change. Sensitivity of the simulation was calculated by translating simulated ΔT to ΔV with Equation 3.6, in which the temperature coefficient of resistance, α, was 0.2 % according to literature, the original resistance, R_0, was 200 Ω, and the heater input power was 5 mW.

(a)   (b)
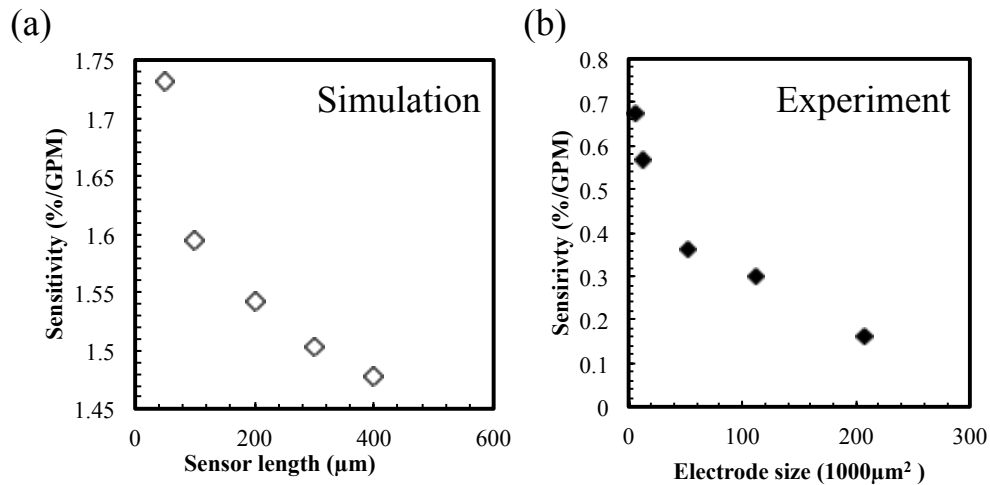
Figure 3.6 The sensitivity of various sensor sizes in (a) the simulation and (b) the experiment.

$$Sensitivity = \frac{\Delta V}{V_{avg}\Delta Q} \qquad\qquad (3.5)$$

$$R = R_0(1 + \alpha T) \qquad\qquad \textbf{(3.6)}$$

3.3.2　　Influence of the Flowing Fluid Temperature

By using the water temperature sensor and the flow-rate sensor, the device can measure the water flow rate at different flowing water temperatures. Figure 3.7(a) is the voltage readout of the temperature sensor on the device, which can be used to calculate the water temperature. Figure 3.7(b) is the voltage difference between the voltage on the flow-rate sensor and the voltage on the temperature sensor. If the temperature sensor indicates the flowing water is 40 ˚C, the flow rate can be found by using the dash line and matching the voltage difference to the flow-rate line. Figure 3.7(c) is the same data as in Figure 3.7(b) plotted versus flow rate instead of temperature, and the curves show the relationship between voltage difference and flow rate at a given temperature. These curves can be collapsed into a single curve (Figure 3.7(d)) by using a translated voltage difference, ΔV_m, defined by Equation 3.7. ΔV_{ref} is the readout at 2 GPM in the same water temperature.

$$\Delta V_m = \Delta V - \Delta V_{ref} \qquad\qquad \textbf{(3.7)}$$
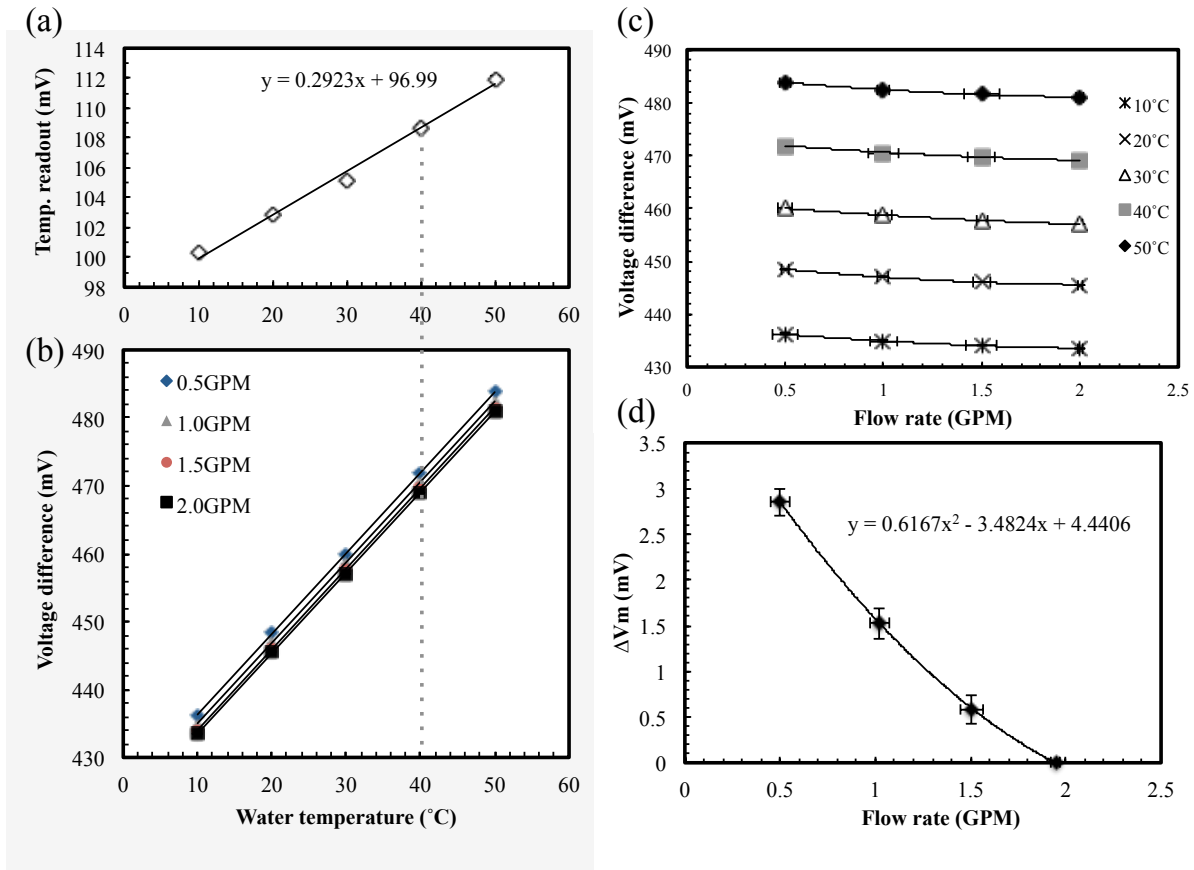
Figure 3.7 (a) The temperature sensor readout versus the water temperature. The dash line is an illustration that 109 mV temperature readout indicates 40°C of water, and the flow rate can be looked up by (b) the voltage difference or the flow-rate readout in different water temperature. (c) Voltage difference versus flow rate (d) Normalized curve ΔV_m defined by Equation 3.7.

With the same sensor size, ΔT is higher in lower water temperatures, but ΔT can be normalized by theoretical or empirical translation. The ΔT of the COMSOL simulations for different water temperatures is shown in Figure 3.8(a). To normalize the data, the functional form of h was derived from Equation 3.8.

$$Nu_{object} = 0.6Re_p^{0.5}Pr^{1/3} = \frac{hD}{k_w} \qquad \textbf{(3.8)}$$
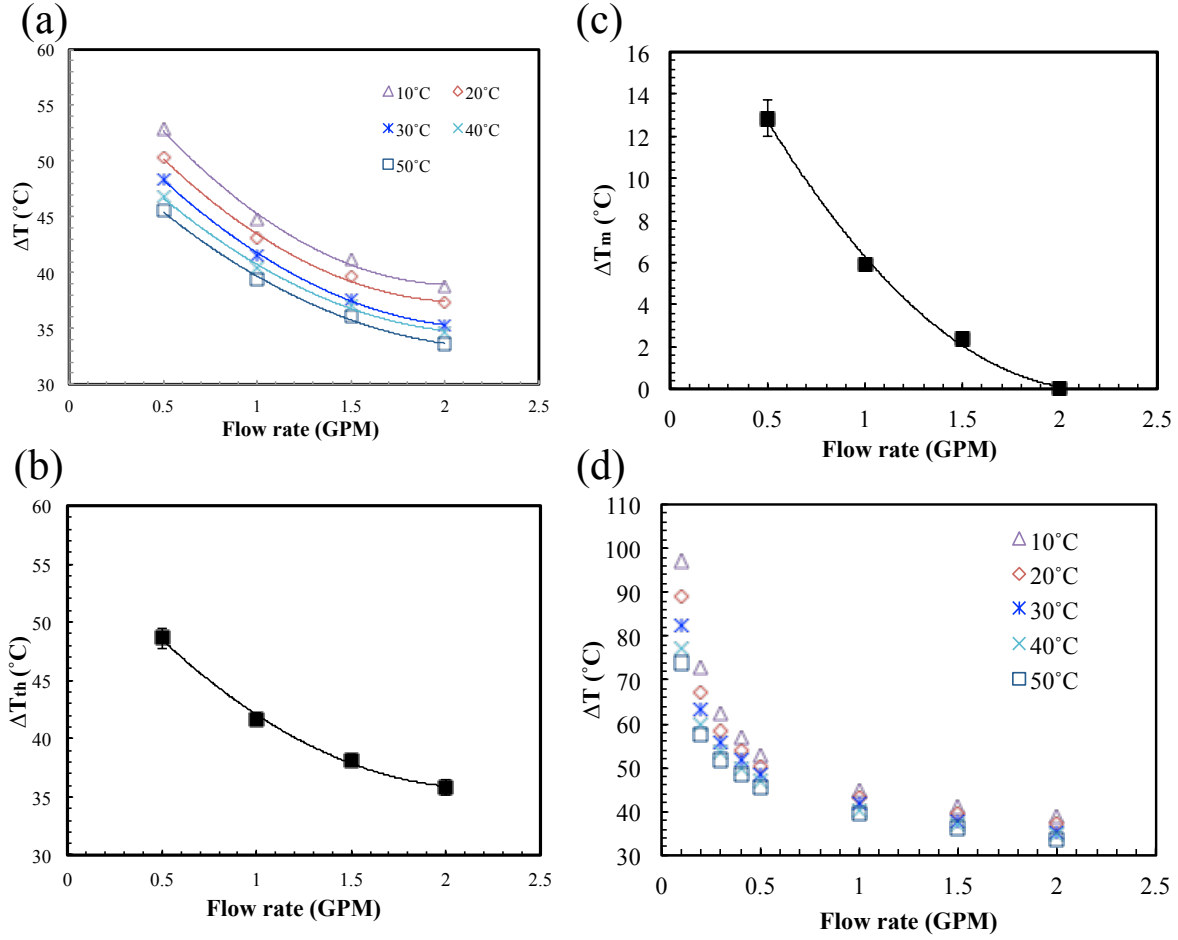
Figure 3.8 COMSOL simulation in different water temperature of (a) ΔT and (b) ΔT_{th} (c) ΔT_m and (d) ΔT in 0.1-2.0 GPM.

In Equation 3.8 Nu_{object} is the Nussult number around a non-spherical object, k_w is the thermal conductivity coefficient of water, D is the conduit diameter, Re_p the Renolds number around a particle, and Pr is the Prandtl number. Pr and the kinematic viscosity, v, in Re_p change with the temperature of water, T, thus h is a function of T. The general form of that function can be derived from Equation 3.8 and is shown in Equation 3.9, in which B_1 is a constant.

$$h(T) = B_1 v^{-0.5} Pr^{1/3} \tag{3.9}$$

Thus, to define a temperature difference between the heater and the water, ΔT_{th}, which is independent of T, Equation 3.3 can be modified into:

40

$$\Delta T = \frac{P}{\frac{1}{R_s} + hA_s} = \frac{\Delta T_{th}}{Bv^{-0.5}Pr^{1/3}} \tag{3.10}$$

The constant B in Equation 10 was set as 0.51 to let ΔT_{th} has the same average temperature as ΔT. All curves in Figure 3.8(a) can be normalized to Figure 3.8(b) with Equation 3.11:

$$\Delta T_{th} = \Delta T(0.51v^{-0.5}Pr^{\frac{1}{3}}) \tag{3.11}$$

The curves in Figure 3.8(a) can also be collapsed into a single curve (Figure 3.8c)) by using a empirically translated temperature difference, ΔT_m

$$\Delta T_m = \Delta T - \Delta T_{ref} \tag{3.12}$$

In which ΔT_{ref} is the ΔT that occurs at the highest flow rate (i.e., 2.0 GPM) in the same water temperature.

Figure 3.8(a)-(c) shows that the sensor could measure 0.5-2.0 GPM in 10-50 ˚C water and that the influence of water temperature could be normalized. The sensor could also measure smaller flow rates, as shown in Figure 3.8(d). The sensor could detect 0.1-2.0 GPM of water, and detection of smaller flow rates was also possible. The sensor was actually measuring velocities between 10 to 250 cm/s. This research focused on the application in 1inch diameter pipes, but using other pipe diameters, the sensor can be used for a wide range of flow rates and various applications. The 71 µm by 80 µm size also makes it possible to be used in micro-channels.

3.3.3 Influence of the Input Power
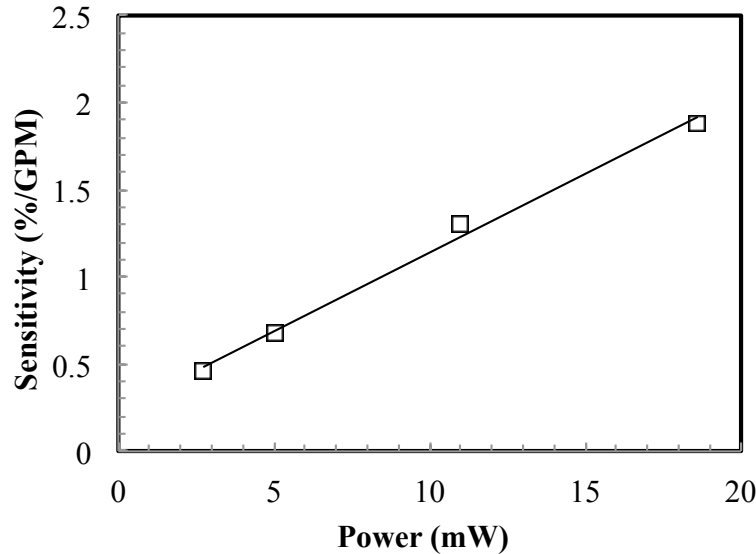
Figure 3.9 The input power and the experimental sensitivity of XS sensor

As the input power is decreased, the sensitivity of the device decreases. In Equation 3.3, ΔT is proportional to P, and increasing ΔT improves the sensitivity. In Figure 3.9, as research suggests [10], [14], [50], the sensitivity is proportional to the input power due to the higher temperature created at the sensor surface. Increasing the power too high, though, results in an inoperable sensor due to boiling. For the XS probe, increasing the input power over 20 mW caused the flow-rate sensors to become noisy and produce erratic results while the temperature sensors remained stable. The comparison of low and high input power signal was shown inFigure 3.10. Figure 3.10(a) was stable and supplied with 2.75 mW while Figure 3.10(b) became noisy with 35.64 mW input power. Figure 3.11 shows the calculated temperature on the flow-rate heater using Equation 3.13, in which I is the input current, V is the voltage measured on the heater, and R_0 is the calculated resistance at zero input power. αR_0 was measured by a

multimeter and was 0.275 for XS probes. The error bar was the temperature error calculated from input current and the standard deviation of the measured voltage. Sensor temperatures with more than 20 mW input power exceeded 100˚C, the boiling point of water under 1 atm.
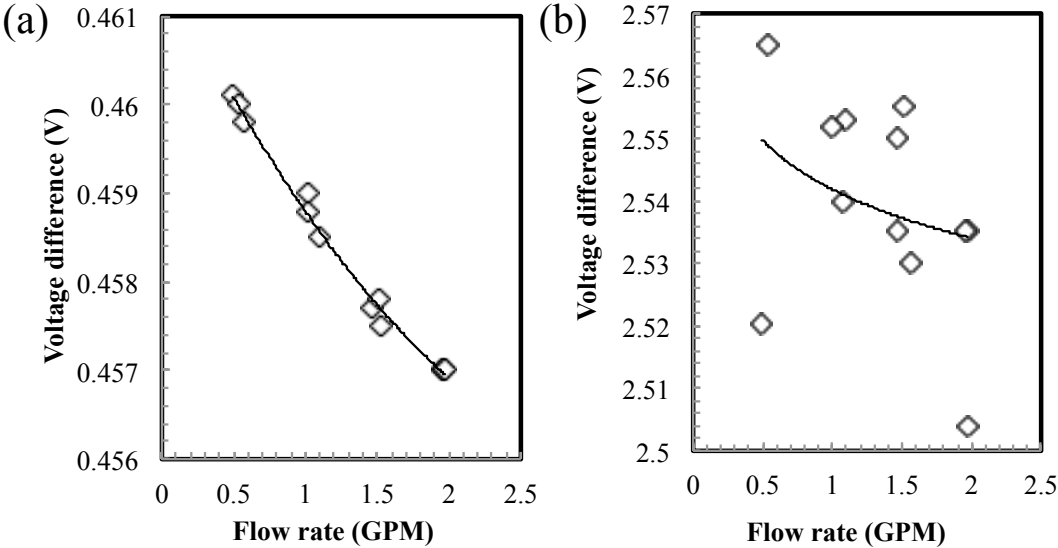
Figure 3.10 The raw data for the XS sensor supplied with (a) 2.75 and (b) 35.64 mW
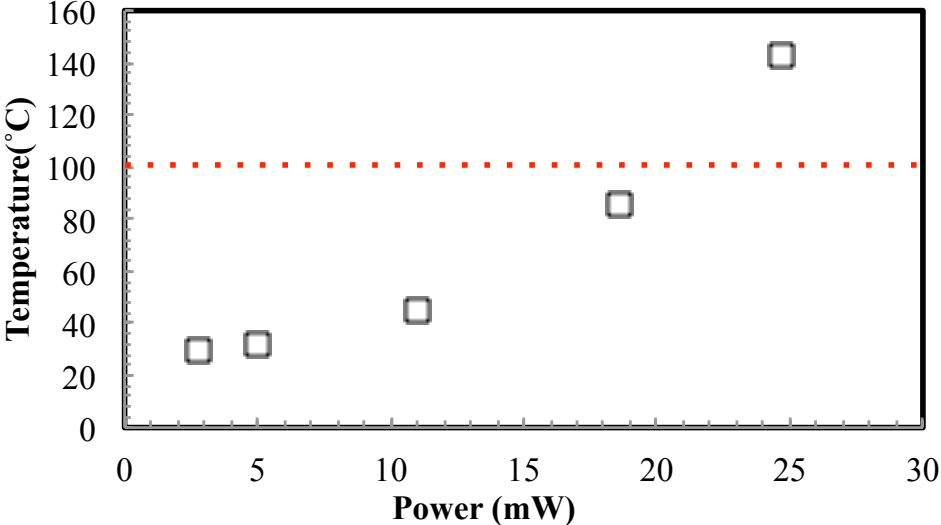
Figure 3.11 The calculated surface temperature of XS probes in experiment.

$$T = 30 + \frac{\frac{V}{I} - R_0}{\alpha R_0} \qquad\qquad \textbf{(3.13)}$$

3.4 Possibility of Pulsing Flow-rate Sensor

This dissertation presents energy and cost efficient flow-rate sensors in continuous mode, but a pulsed mode sensor may be more suitable to save energy. The requirement of a sensitive pulsed mode flow-rate sensor is very similar to what presented previously: a thermal insulating substrate, a sufficient input power, and a small sensing surface area. The difference between a pulsed and a continuous flow-rate sensor is that the pulsed mode sensor must need a heater and a separate RTD [51], [52], and the heat transport between the heater and the RTD should be considered. Thermal analysis of pulsed mode flow sensor is much more complicated than continuous mode. The heat transport analysis of a pulsed thermal flow sensor was presented by Okulan et al.[52]. However as Bruschi et al. indicated, most previous research focus on small flow rate in micro-channel [51]. Research and validation of pulsed mode thermal flow-rate sensor in residential range (i.e. 0.5-2.0 GPM or 114-454 L/h) is still needed.

3.5 Summary of the Flow Rate and Temperature Detection

This dissertation presents a thermal flow-rate sensor that is integrated with a temperature sensor and can measure large flow rates up to 2 GPM (~0.1 L/s) in 10 to 50 ˚C water. Responding to velocity between 10 to 250 cm/s, the sensor can also measure 0.2 to 7.8 mL/s water in 150 µm wide micro-channels or 2 to 78 L/s water in 6 inch diameter municipal pipes. Thus the sensor can span over 5 orders of magnitude in flow rates. And the sensors are fabricated with platinum, a metal that has not only the sufficient TCR for the flow-rate sensors to function but also the inert property to be used for other purposes such as water-sensing electrodes.

In terms of cost, the devices are 3 mm by 3 mm and can be fabricated with only one mask and a protection layer on the sensor surface. With this relatively simple fabrication, each device costs less than 30 cents, and more than 800 devices can be fabricated on a 4 in wafer. If fabricated on an industrial-sized 12 in wafer, around 7300 devices can be fabricated per wafer and the cost could be reduced even more. And note that adding electrochemical sensing using a platinum electrode on this device would not increase the cost since this metal is already present in the construction process — the construction of the extra sensors is essentially free.

CHAPTER 4

Ionic Conductivity Measurement for Residential Water

4.1 Sensor Fabrication and Experimental Methods

4.1.1 Sensor Fabrication and Experimental Methods for Sensor Optimization

(a)   (b)   (c)
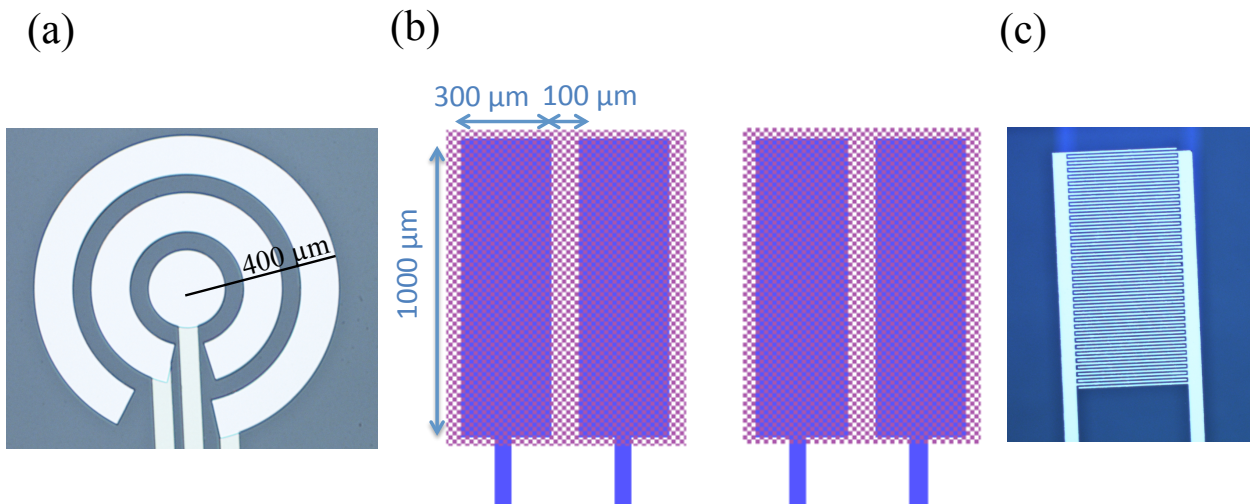
Figure 4.1 Sensor geometry of (a) target sensor, (b) four-electrodes parallel sensor, and (c) comb sensor

This dissertation presents preliminary research for various electrode conductivity sensors to design the optimized method for residential conductivity measurement. The optimized sensor of target shape in Figure 4.1(a), preliminary design of two and four-electrode parallel sensor in Figure 4.1(b), and the two-electrode comb sensor in Figure 4.1(c) are all tested. The electrodes

on the target sensor are 100 μm wide separated by 50 μm gap (the same geometry of the target sensor in Chapter 5). Each electrode on the four-electrode parallel sensor is 300 by 1000 μm separated by 100 and 300 μm gap. The two-electrode sensor is composed of the left two electrodes on the four-electrode sensor. The pink area is the area covered the dielectric materials. Each electrode on the comb sensor is has 35 fingers, and each finger is 10 by 650 μm separated by 10 μm gap.

All sensors (Figure 4.1(a-c)) were physical vapor deposited 300/1000 Å Ti /Pt on a glass wafer. The PVD pressure was controlled under $2x10^{-6}$ Torr with deposition rate of 15 and 5 Å/s. The dielectric layer in Figure 4.1(b) was PECVD silicone nitride. The sensors were integrated with PC board and inserted into a glass tube connected with a water pump (Figure 3.1(a-c)). Various voltage of pulsed and square wave was supplied to the sensor by an external power source, and all the signal was obtained with Labview.

4.1.2   Sensor Fabrication and Experimental Methods for Target Sensor

The sensor (Figure 4.1(a)) was physical vapor deposited 300/1000 Å Ti /Pt on a glass wafer. The sensor geometry is a three-electrode target design, which is used in both conductivity and pH/ORP sensors. The gap between the electrodes was 50 μm. The pressure was controlled under $2x10^{-6}$ Torr with deposition rate of 15 and 5 Å/s. The outside radius of electrodes were 400 μm, 250 μm, and 100 μm. The sensor was integrated with PC board and inserted into a glass tube connected with a water pump (Figure 3.1(a-c)), and the flow rate of the water was controlled at 2.0 Gallon per minute (GPM), the common flow rate in household faucets, for all conductivity tests.

During the conductivity tests, a voltage was pulsed from 0 to 0.5 V at 6200 Hz on the two larger electrodes on the sensor. The two outer electrodes were connected in series with an off-

chip resistance, R, and the root-mean-square current passed through the resistance, Irms, was measured as a conductivity indicator. DI water and NaCl were added into the water tank to change the conductivity in both increasing and decreasing directions. The fluid is in turbulent status ensuring well mixture. The reference conductivity was measured with an external conductivity meter.

4.2 Results and Discussion of the Ionic Conductivity Measurement

4.2.1 Ionic Conductivity Optimization
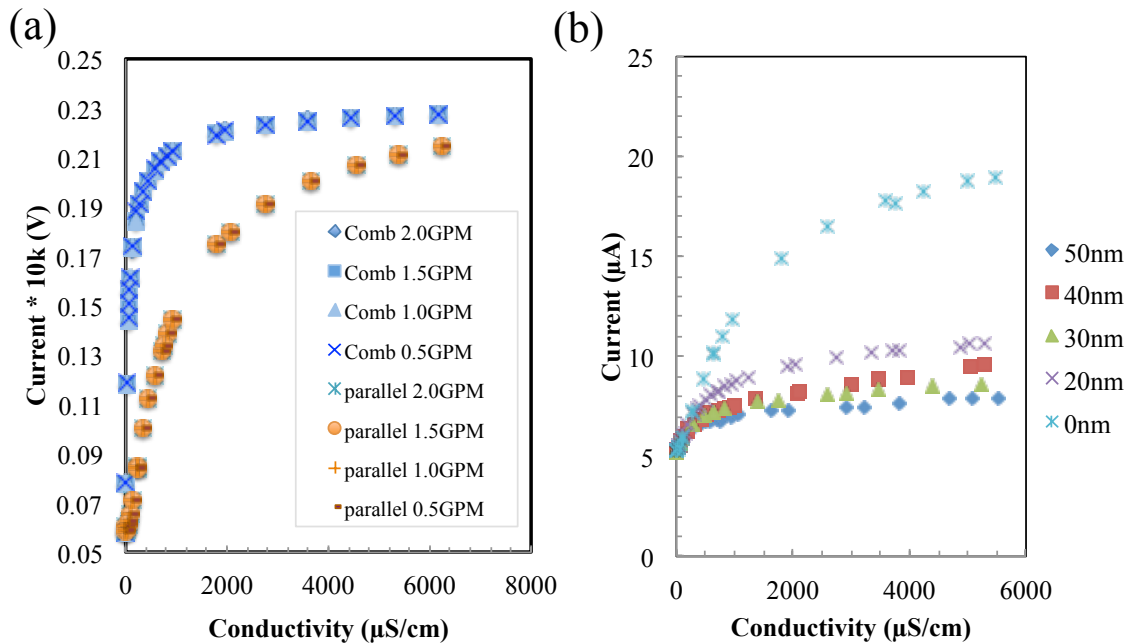
Figure 4.2 The conductivity measurement (a) in different flow rate and (b) with different dielectric thickness.

This dissertation presents preliminary research to design the optimized electrode conductivity sensors for residential water. The influences of flow rate and the thickness of the dielectric layer are presented in Figure 4.2. In Figure 4.2(a), two kinds of two-electrodes sensor, the comb (Figure 4.1(c)) and the parallel (left two electrodes in Figure 4.1(b)) sensors, were

supplied with 6200 Hz, -0.25 V to 0.25 V square wave voltage. The current passed through the two electrodes was measure by obtaining the voltage across the resistor, R (10 kΩ). Both sensors have no dielectric layer covered on the electrodes so the electrodes were bare platinum. The flowing water temperature was 30 ˚C and the conductivity was changed with NaCl. As shown in Figure 4.2(a), flow rate caused no shift in the conductivity measurement, but the sensitive region is a bit shifted due to the different sensor geometries. The geometry of the conductivity sensor determines the cell constant of the sensors (will be explained in Chapter 4.2.2). Both the two-electrode comb and parallel sensors are suitable for the conductivity in the interested region.

The necessity of the dielectric layer was tested in Figure 4.2(b) and the results showed the dielectric layer was not necessary. Conductivity sensors with dielectric films are common for applications with strong electric double layer (EDL). In some cases, especially micro-fluidic or medical applications, EDL has strong influence on obtaining the impedance value of the test solution [53]. To prevent the forming of EDL, an appropriate thickness of silicon nitride or other dielectric material should be applied on the electrodes. Two-electrode parallel sensor with five different thickness of silicone nitride was tested and shown in Figure 4.2(b). The thicker the dielectric layer was, the smaller the sensitivity was. The sensor with 0 nm nitride, which was bare platinum electrodes, had the strongest signal. Dielectric layer is not necessary in the interested region, and bare platinum electrodes are selected for the following experiments.

The conductivity sensor showed fast response in 100 milliseconds and the direction of the supplied voltage showed no significant influence. In Figure 4.3, the four-electrode parallel sensors were tested under various supplied voltage. The 6200 Hz, -0.25 V to 0.25 V square wave or 0 – 0.5 V pulsed wave voltage were applied on the two outer electrodes, and the current passed through the inner two electrodes was measured as the signal. Figure 4.3(a) showed the

direction of the supplied voltage (positive pulsed wave or positive-and-negative square wave) had no significant influence on the conductivity measurement. Figure 4.3(b) showed the sensors had fast response, the signals obtained at steady state showed no significance difference with the signals from 100 mS after the supplied voltage was turned on. Further, we observed no obvious reactions that interrupted conductivity measurement. Figure 4.3(b) showed the conductivity measurement was not interrupted up to 1.0 V pulsed wave. The larger the supplied voltage was, the stronger the signals were. We chose 0 – 0.5 pulsed wave as the supplied voltage for the following experiment because the circuits for the pulsed wave are cheaper than the circuits for the square wave.
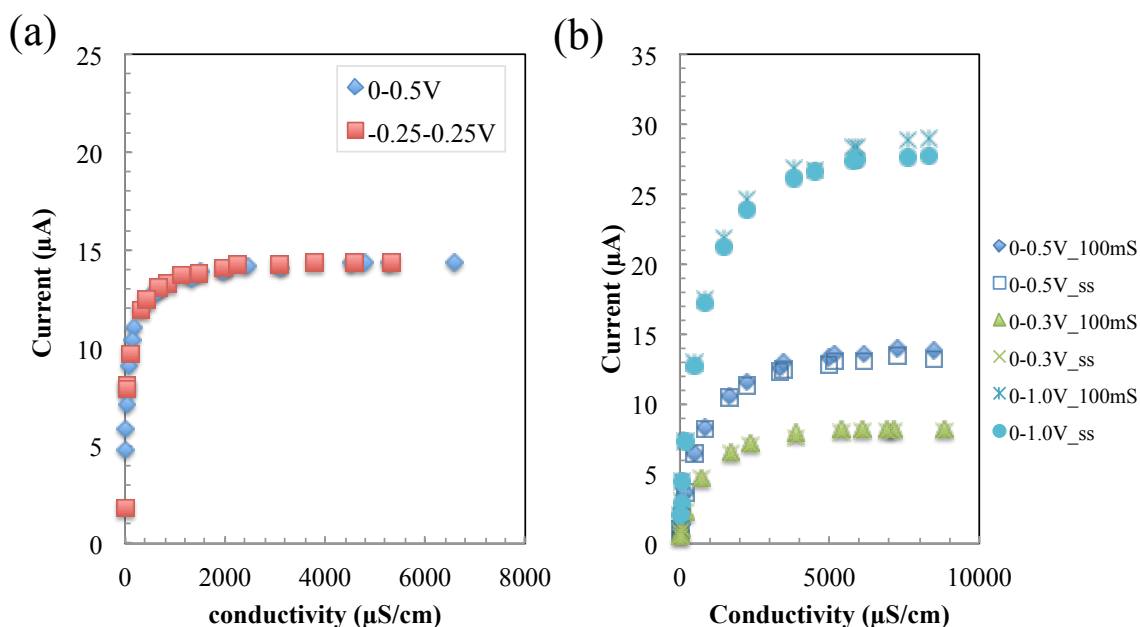
Figure 4.3 The conductivity measurement with two-electrode parallel sensor with (a) square and pulsed wave and (b) different supplied power.

Noted that the measurement with four-electrode parallel sensor in Figure 4.3 showed similar trend with Figure 4.2, the measurement with the two-electrode parallel sensor. Though

four-point impedance measurement is known to be more accurate than two-point method, we observed no significant difference between the two methods in the interested conductivity region. For residential water, small cost and sensor size are much more important than precise measurement. Therefore, we chose two-electrode sensor with bare platinum electrodes for the follow-up experiments. The further optimization is presented in section 4.2.2.

4.2.2　　　　Ionic Conductivity Measurement with Target Sensor
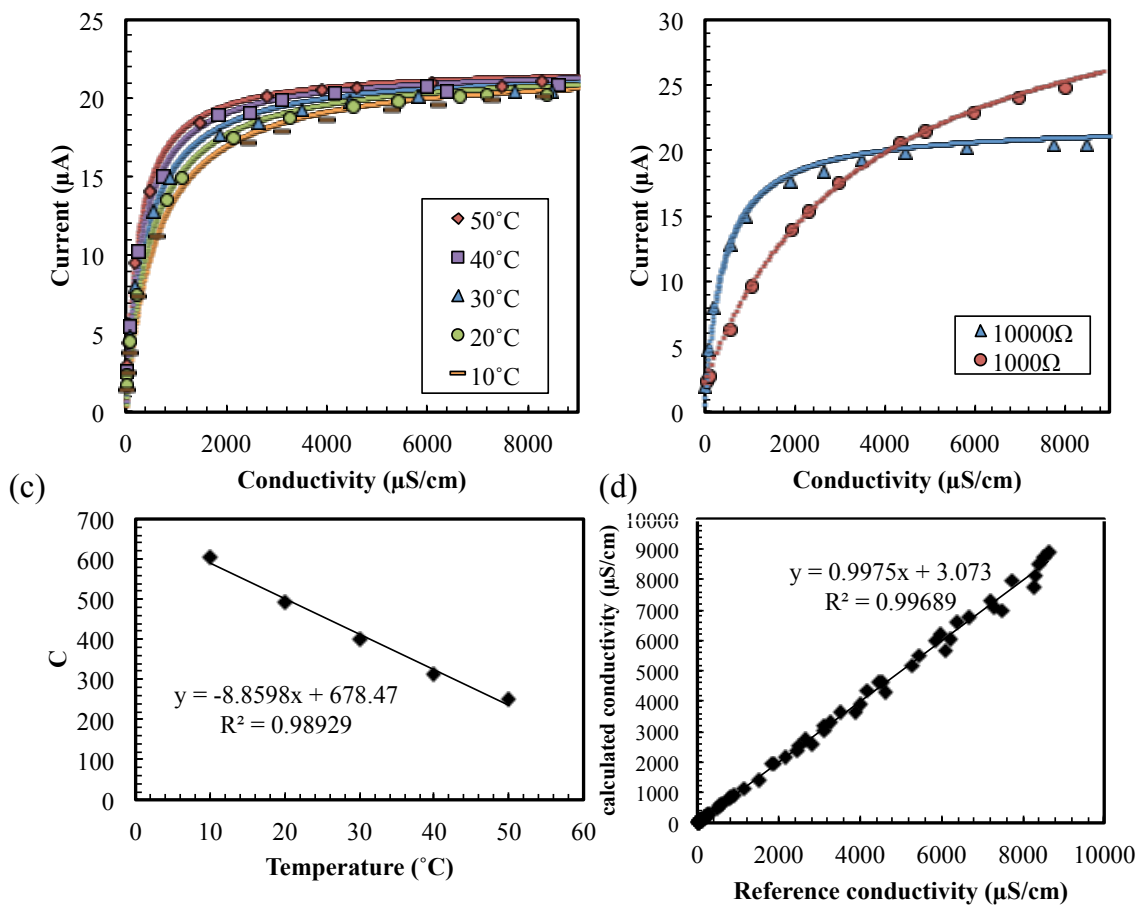
Figure 4.4 The rms current versus conductivity (a) in 10 – 50 ˚C water with 10 kΩ and (b) with 1 kΩ and 10 kΩ in 30˚C. (c) The constant C* versus temperature and (b) Measurement calculation with Equation 4.4.

To integrate the conductivity sensor with all the other water sensors, we design a new sensor geometry that is called the "target sensor". The sensor we have constructed (Figure 4.1(a)) can measure three crucial variables of water monitoring: conductivity, pH, and ORP. The performance of the ionic conductivity measurement is shown in Figure 4.4(a). To obtain the measurement, a 6200 Hz, 0.5 V pulsed wave V_{rms} was pulsed between the outer two electrodes and the root-mean-square current, I_{rms}, indicated the conductivity, σ. The sensitivity of the conductivity measurement can be easily adjusted by changing an off-chip resistance, R, connected in series with these electrodes. Figure 4.4(b) shows the results of such adjustments, with larger resistances leading to higher sensitivity at lower conductivities. For residential water monitoring, conductivity region between 1-1000 µS/cm is more important because it represents the quality of drinking water. The sensitivity of this region should be able to distinguish different water samples of 100 µS/cm difference. On the other hand, water of 1000-8000 µS/cm is usually the water in swimming pools, the sensitivity in this region should be able to tell the difference of 1000 µS/cm. Since the lower region is more important in this application, 10 kΩ resistance is chosen for the following experiments.

The conductivity data was fit well by the correlation:

$$I_{rms} = \frac{V_{rms}}{R + \frac{C_1}{\sigma}} = \frac{\sigma \frac{V_{rms}}{R}}{\sigma + \frac{C_1}{R}} = \frac{\sigma I_{max}}{\sigma + C} \tag{4.2}$$

This equation follows from Ohm's law, assuming a series resistance established by R and solution conductivity through a cell constant C_1 (unit of length per area, cm^{-1}). I_{max}, the saturated current, can be optimized for a specific range of conductivity by changing R in the circuit, as stated previously.

The conductivity of residential water and water in reservoirs is commonly 0 to 8000 µS/cm in a temperature range of 10 to 50 ˚C. As shown in Figure 4.4(f), the sensor can measure conductivity in this region using an R of 10 kΩ. The influence of water temperature in Figure 4.4(a) could be mitigated by using Equation 4.2, in which σ_0 is the calibrated conductivity at given temperature, T_0, and σ_t is the conductivity at temperature T [54]:

$$\sigma_0 = \frac{\sigma_t}{1 + A(T - T_0)} \tag{4.2}$$

Combination of Equations 4.1 and 4.2 yields

$$I_{rms} = \frac{\sigma_t I_{max}}{\sigma_t + C} = \frac{\sigma_0 I_{max}}{\sigma_0 + \dfrac{C}{1 + A(T - T_0)}} = \frac{\sigma_0 I_{max}}{\sigma_0 + C^*(T)} \tag{4.3}$$

The function C* in Figure 4.4(c) was derived from Figure 4.4(a) with A as 2%, matching the common temperature coefficient of water. Conductivity measurement in Figure 4.4(d) thus can be described with Equation 4.4.

$$\sigma_0 = \frac{I_{rms} C^*}{I_{max} - I_{rms}} \tag{4.4}$$

4.3 Summary of the Ionic Conductivity Measurement

In this section, the conductivity sensors are optimized for residential water measurement considering the sensor cost, the sensor size, and the integration with other sensors. The final design is a two-electrode conductivity sensor that has bare platinum electrodes and is supplied with 6200 Hz, 0 - 0.5 V pulsed square wave. The geometry of this sensor is a three-electrodes target sensor but only the outer two electrodes were used in the conductivity measurement. The experiments results suggests dielectric layers are not necessary for the interested region, so the

conductivity sensor has only bare platinum electrodes and can be easily integrated with other sensors presented in this dissertation.

The presented conductivity sensor is ideal for the integration with other water sensors. The conductivity sensor shares the same geometry with the pH/ORP sensor (in Chapter 5) so the same sensor can measure all of the three variables. This multifunctional design ensures the sensors to be small and cost-efficient, which are crucial for practical residential water monitoring. All sensors presented in this dissertation are fabricated on glass substrates, which offers decent thermal isolation. The heat generated on the flow sensor barely changed the temperature on the conductivity sensor so the conductivity reading is not influenced by the heat (Figure 3.3 in Chapter 3). Combined with the water temperature sensor presented in Chapter 3, the conductivity sensor presented in this chapter can be applied in residential water detection.

CHAPTER 5

pH and ORP Measurement with Bare Platinum Electrodes

5.1 Sensor Fabrication and Experimental Methods

The sensor shared the same geometry and fabrication methods with the conductivity sensor. The sensor (Figure 4.1(a)) was physical vapor deposited 300/1000 Å Ti /Pt on a glass wafer. The gap between the electrodes was 50 μm. The pressure was controlled under $2x10^{-6}$ Torr with deposition rate of 15 and 5 Å/s. The outside radius of electrodes were 400 μm, 250 μm, and 100 μm. The sensor was integrated with PC board and inserted into a glass tube connected with a water pump (Figure 3.1 in Chapter 3), and the flow rate of the water was controlled at 2.0 Gallon per minute (GPM), the common flow rate in household faucets, for all pH, and ORP tests. DI water and chemicals were added into the water to change the properties of the water in both increasing and decreasing directions several times for each experiment. The fluid is in turbulent status ensuring well mixture, and the pH and ORP are monitored real-time by using YSI meters to detect pH and ORP without buffer. The conductivity was changed with NaCl, the pH are changed with HCl and NaOH, and the ORP was changed with HClO.

In pH and ORP test, the largest electrode was the anode (+), the middle one was the cathode (-), and the smallest electrode was the ORP sensing electrode. The sensor was supplied 0.15 µA by Keithley 2401 sourcemeter, the current flew from the anode to the cathode in the solution, and the voltage differences were measured by Labview 2011. Labview measured the potential differences between the anode and the smallest electrode as ΔV_1 (>0) and between the cathode and the smallest electrode as ΔV_2 (<0) simultaneously. ΔV_2 indicated ORP while the difference ($\Delta V_1 - \Delta V_2$), which equaled the potential difference between the anode and the cathode, indicated pH. The flow rate of water was also controlled at 2.0 GPM.

The chloride-PVC membrane in section 5.2.3 was consist of 63 mg of PVC, 20 mg 1-dodecyl-3-methylimidaze, 144 µl bis-2-ethylhexyl, and 7.54 µl 1M silicone tetrachloride. All chemicals were dissolved in 2 ml tetrahydrofuran. A drop of 3-aminopropyltriethoxysilane was dried on the sensor to improve adhession, and another drop of PVC solution was dried on the sensor. The cathode on a coated sensor chip and the anode as well as the smallest electrode on another uncoated sensor chip were used for measurement in high hypochlorite solution measurement.

5.2 Results and Discussion of the pH and ORP measurement

5.2.1   pH and ORP Measurement with Bare Platinum Electrodes

The pH/ORP sensor shares the same geometry with the conductivity sensor but not the operation methods. During the pH/ORP measurement, the potential on the cathode changed smaller than the potential on the anode and the ORP of water, thus the sensor can measure pH and ORP. As shown in Figure 5.1(a), when a 0.15 µA DC current was passed from the largest electrode (anode) to the middle electrode (cathode), the potential difference between the cathode

and the smallest electrode, ΔV_2, indicated ORP in the ORP range of 150 to 800 mV. ORP is defined as the open circuit potential between a platinum electrode and a reference electrode offering a stable potential. The linear ORP measurement in Figure 5.1(a) suggested not only that the sensor could measure ORP but also that the cathodic potential remained relatively constant in various conditions. In Figure 5.1, the sensor was operated in a wide conductivity (200 to 8000 µS/cm) range, which equaled chloride concentrations of 60 to 2700 mg/L. The pH values were titrated from 4 to 10. These values were picked because they were in the common range for drinking water sources. The result suggested the potential on the cathode remained relatively constant in the wide-range conductivity, pH and ORP conditions. On the other hand, the potential difference between the anode and the cathode indicated pH. The data in Figure 5.1(b) was obtained with the sensor operating in the same condition range as Figure 5.1(a) and at the same time. Despite the ORP and the salt concentration varying, the sensor can detect pH changes from 4 to 10. This pH sensor is not extremely precise but it is sufficient to evaluate pH changes on the order of ½ to 1 units.
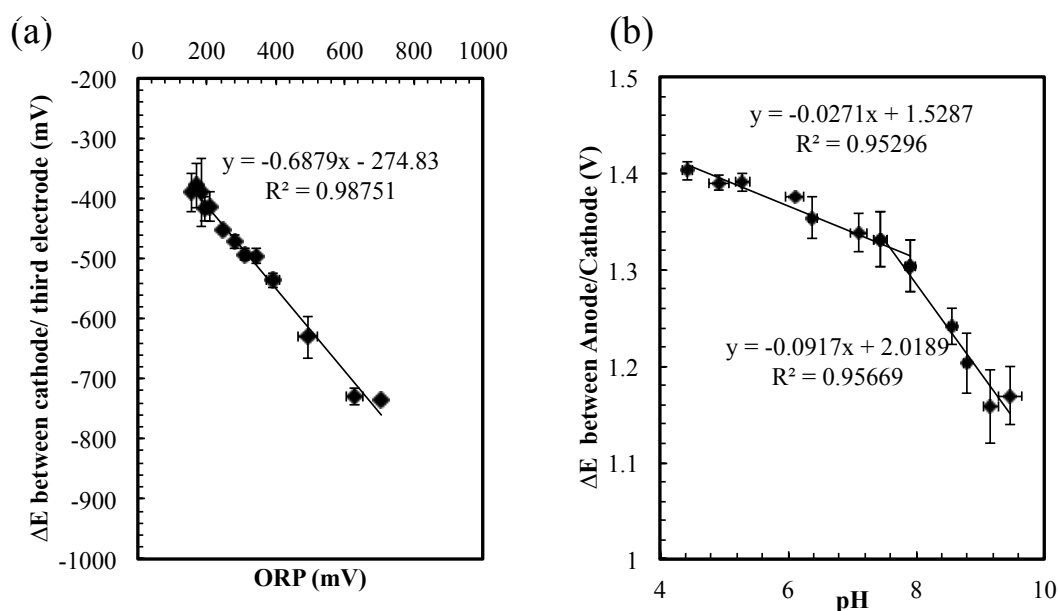
Figure 5.1 (a) The potential difference between the third electrode and the cathode

indicates ORP (b) The potential difference between cathode and anode was a pH indicator in various chloride concentrations.
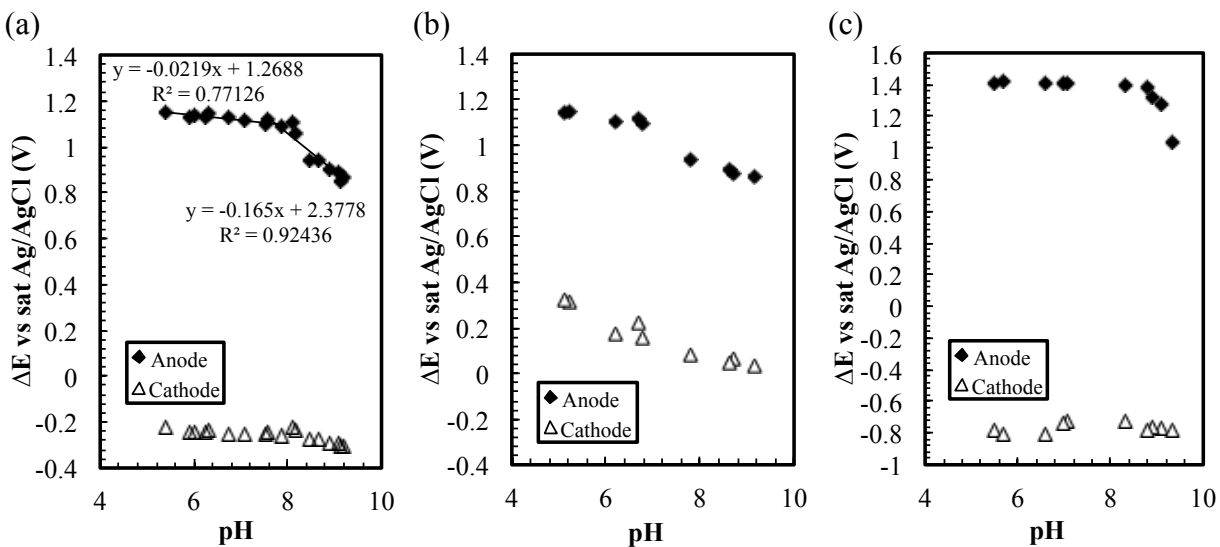
Figure 5.2 (a) The potential on the cathode and the anode versus saturated Ag/AgCl reference electrode at 0.15 μA, (b) 0.05 μA, and (c) 1.0 μA.

The electrochemical reactions that produced the stable cathodic voltage presumably started with active sites on the platinum cathode's surface being occupied by chloride through the adsorption reaction [55]. The reactions are not completely known but to understand the reaction on the electrodes, the potential change on the cathode and anode was examined with an additional Ag/AgCl reference electrode. As shown in Figure 5.2(a), the potential on the anode changed with pH while the potential on the cathode remained relatively stable. The reaction on the cathode presumably was chloride adsorption on platinum surface as listed in Equation 5.1 [55]:

$$Pt^* - Cl + e^- \leftrightarrow Pt^* + Cl^- \tag{5.1}$$

If electrolysis of water occurred, hydrogen generation would appear through the cathodic reactions as Equation 5.2 and 5.3 [56]:

$$H^+ + Pt^* + e^- \leftrightarrow Pt^* - H \qquad\qquad (5.2)$$

$$Pt^* - H + H^+ + e^- \leftrightarrow H_2 + Pt^* \qquad\qquad (5.3)$$
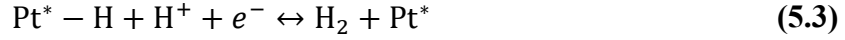
However, according to the Nernst equation, the potential on the cathode should vary with pH if a half-reaction involves H^+, or with the log of the concentration if it involves other dissolved ions. Thus, the relative independence of the cathode potential from pH suggests that H^+ is not involved in the cathodic half-reaction. Further, the supplied current density was ~90 µA/cm^2 and at least 200 mA/cm^2 is typically required to drive water electrolysis [57].

Chloride adsorption on platinum has been studied previously but the value of the half-reaction has been underestimated because it is usually considered a catalyst 'poison' in electrochemical reactors such as hydrogen fuel cells. Chloride strongly chemisorbs, forming small polarity bonds on platinum (111) facets [58]; the strength of this bond is essential for Pt/PtCl providing a relative stable potential. The half-reaction in Equation 5.3 was studied in detail by Stern [55], who found that it corresponded to a pH-independent peak in cyclic voltammetry. Chloride adsorption can passivate platinum to both hydrogen and hydroxide ions between 0.3 and 0.7V (SHE) [59]. The potential required to drive complete chloride desorption was found to be pH and chloride-concentration independent at sufficiently negative potentials (< −320 mV vs. SCE) [58]. In addition to a covalent metal/ion interaction, Rose and Benjamin suggested that an adsorbed water layer may solvate the chloride as well [60]. The adsorption of other halide anions on platinum (111) and gold (111) has also been studied *in situ* by x-ray scattering [61].

On the other hand, the anode potential varied with pH when chloride was present, but remained relatively constant with respect to pH in chloride-free test solutions. Thus the reaction

was suspected to be hypochlorite generation. Hypochlorite dissociates with a pKa of 7.5 [62], which may cause the slope change in pH measurement; the observed cell potentials are consistent with the half-reactions

$$HClO + H^+ + 2e^- \leftrightarrow Cl^- + H_2O \qquad \textbf{(5.4)}$$

$$ClO^- + 2H^+ + 2e^- \leftrightarrow Cl^- + H_2O \qquad \textbf{(5.5)}$$
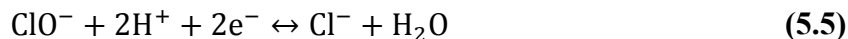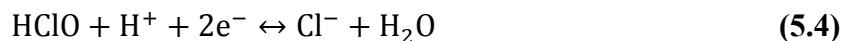
The pH-sensing electrode appears to generate hypochlorite from chloride, which is the most common ion in water reservoirs. It is thermodynamically favorable for oxygen generation to occur through

$$O_2 + 4H^+ + 4e^- \leftrightarrow 2H_2O \qquad \textbf{(5.6)}$$

Although the standard potential of the half-reaction in Equation 5.4 is 1.49 V [63] and that in Equation 5.6 is 1.229V vs SHE [64], there is a considerable overpotential for oxygen generation on metallic Pt [57], [65], [66], so hypochlorite generation may be favored kinetically.

The sensor can measure pH and ORP simultaneously with only simple platinum electrodes but the phenomenon allowing pH and ORP measurement only occurred in a small current range. As shown in Figure 5.2(a), when 0.15 μA (~90 μA/cm^2) was used as the driving current, the change in potential on the cathode with respect to pH was smaller than the change on the anode. If the current was decreased to 0.05 μA (~30 μA/cm^2), potentials on both electrodes changed with pH (Figure 5.2(b)) and the potential difference can no longer be used to indicate pH. In Figure 5.2(c), when 1.0 μA (~580 μA/cm^2) was used, the potential on the anode was not sensitive to pH in lower pH region. This result suggests that evolution of chlorine or oxygen gas could replace chlorite generation at this current density.

The presented pH and ORP sensors are not very precise but have great potential for water monitoring. Contamination, such as toxic algae or heavy metal leakage, often accompanies with a significant decrement of pH value. The decrement of pH is a slow process that usually takes weeks and often occurs unexpectedly in the service lines downstream the treatment plants. Thus end-points pH monitoring at home that doesn't require frequent attention from the users is necessary and much more important than precise accuracy and fast response time. Luckily the pH and major ion concentrations of tap water are in general consistent for years at the same local area. Given Ann Arbor tap water as an example in Table 5.1, the concentration (C) of major ions changed less than 15 ppm over more than 10 years. The pH of Ann Arbor tap water has remained 9.3 from 2003 to 2015. Instead of precise reading, the practical pH sensors for water safety only need to sense the unusual pH decrement and inform the users automatically.

Table 5.1 Major ion concentration of Ann Arbor tap water 2003-2015

Ion	Max C (mg/L)	Min C (mg/L)	ΔC (mg/L)	Year
Ca^{2+}	32	30	2	2014-2015
Mg^{2+}	24	21	3	2014-2015
Na^+	61.5	52	9.5	2003-2015
K^+	3.4	3	0.4	2014-2015
Cl^-	115	112	3	2014-2015
CO_3^{2-}	92.4	77.4	15	2003-2015
SO_4^{2-}	58	56	2	2014-2015
NO_3^-	1	0.47	0.53	2003-2015
NH_4^+	0.16	0.11	0.05	2003-2015
PO_4^{3-}	0.26	0.24	0.02	2014-2015
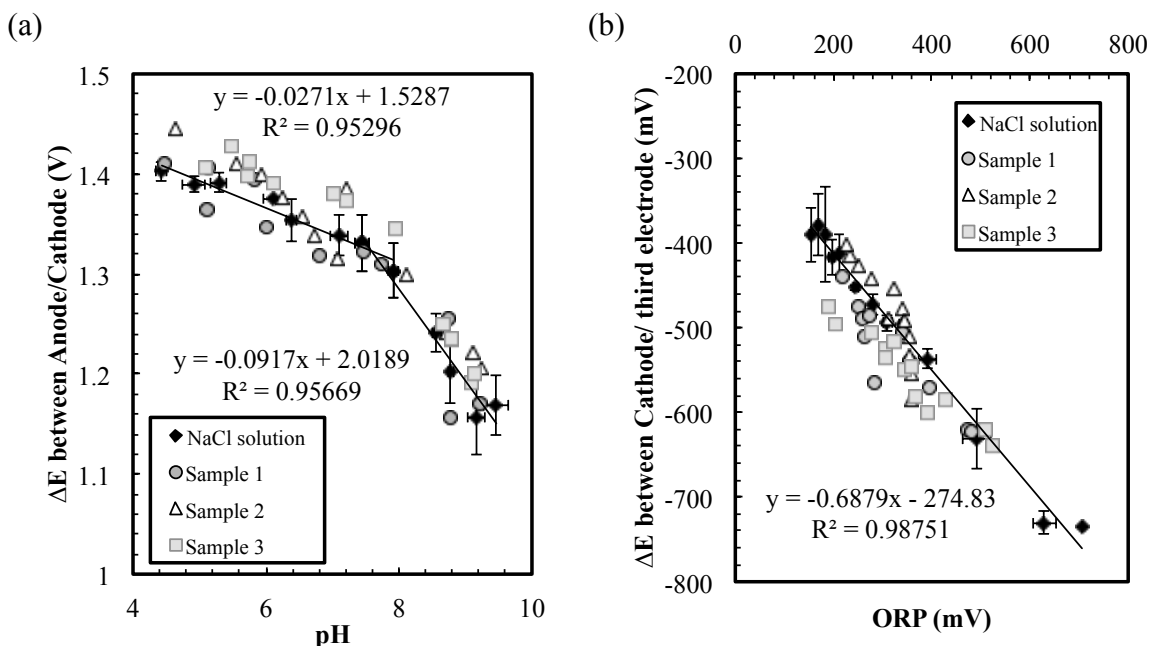
Figure 5.3 (a) The pH measurement and (b) the ORP measurement in the water samples

The sensor presented also showed sufficient tolerance to the interference of other common ions in tap water thus the sensor can be a practical method for water monitoring. Ideal monitoring methods for water safety should be affordable end-point measurement that can detect pH decrement without regular maintenance. The convenience of the sensors are much more important than precise accuracy and fast response time. To test if the sensor presented can be applied in practical use, three samples containing common ions in different concentrations were prepared for the experiment (Table 5.2). HClO was titrated into sample 1 and 3 to change the ORP of water so the concentration of HClO was not a fixed value. Noted the concentration variations between samples (up to 200 mg/L) were 10 times larger than regular situation listed in Table 5.1 (< 15 mg/L). As shown in Figure 5.3, the sensor can measure pH and ORP simultaneously in these different water samples despite some minor drift. The NaCl solution was the same data set from Figure 5.1 that included the common residential water range (sodium and chloride concentrations of 60 to 2700 mg/L), and the sensor showed small drift in the wide

concentration range. Since the major ion concentration at same local area mostly remained unchanged and the sensor requires almost no maintenance, Figure 5.3 suggests the sensor can be an ideal sensor to be embedded in the drinking water service lines to detect pH decrement accompanied with contaminations. However, more experiment should be done with actual water sample from various conditions to validate the sensor performance.

Table 5.2 Ion concentrations in the test simulated samples (mg/L)

Ion	Sample 1 (580 μS/cm)	Sample 2 (870 μS/cm)	Sample 3 (1070 μS/cm)
Ca^{2+}	30	0.45	15
Mg^{2+}	0	20	10
Na^+	30.6	113	143
K^+	4	10	0
Cl^-	112	80	120
CO_3^{2-}	10	0	0
HCO_3^-	61	300	300
SO_4^{2-}	72	80	77
NO_3^-	12.7	0	0
NH_4^+	0	0	1
PO_4^{3-}	0	1	0
HClO	0 – 0.5	0	0-0.5

5.2.2   Sensor Validation and the Response Time

The sensor can only operate with chloride ion, which is the most common ion in both drinking water and water reservoirs. The relative stable potential on the cathode is the crucial reference of the pH/ORP sensor. As described in Equation 5.1, the potential was presumably

from the chloride adsorption on platinum electrode, and the sensor should lose function without chloride ions. Ideally, when there is no chloride ion in the test solution, water electrolysis is the main reaction. The ΔE between the cathode and the anode thus should be a straight flat line (i.e. the ΔE is not correlative to pH) without chloride ions...

Hi '706. illustrates the pH measurement only functions with chloride ions. In the chloride-free test solution, trifluoromethanesulfonic acid or sulfuric acid were added into DI water to maintain similar ionic conductivity as the sodium chloride solution in the previous experiments. As shown in Fig 5.4(a), Δ E changed less in both chloride-free solutions than in chloride solution. This phenomenon implied the relative stable potential on cathode is disappearing. After added in sodium chloride, the potential difference between the anode and the cathode turned back to the black curve with chloride. Figure 5.4(b) showed the potential on the cathode is only stable on the cathode.

(a)   (b)
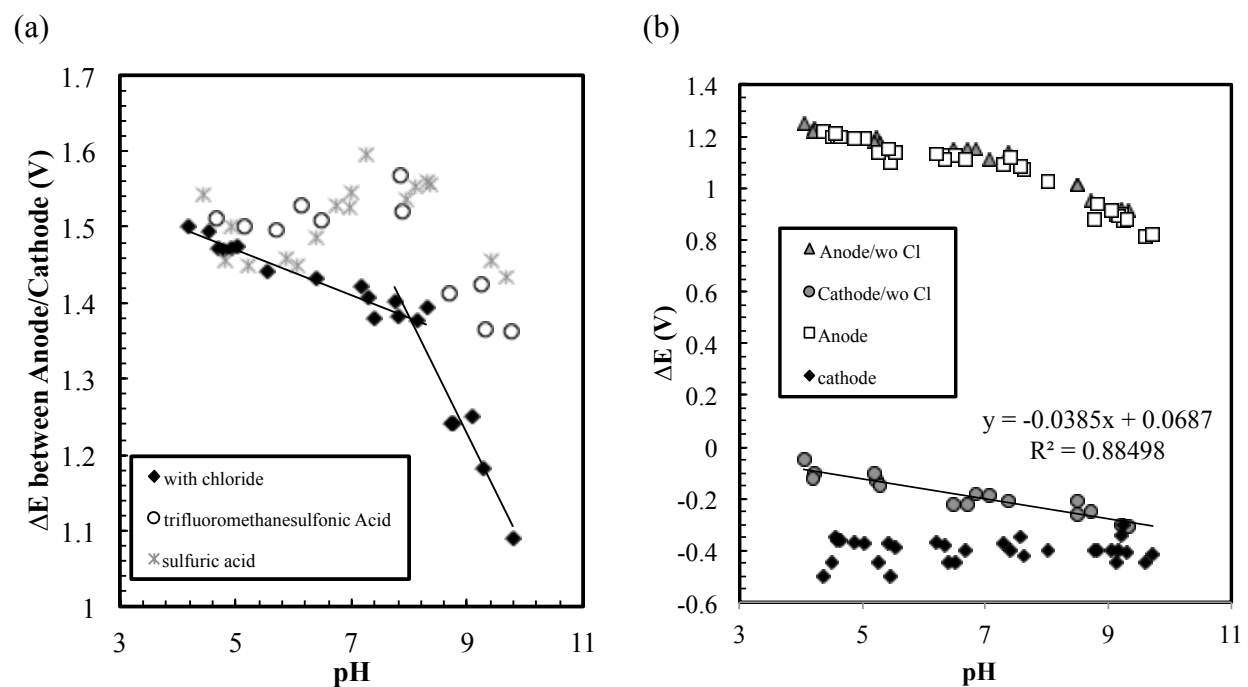
Figure 5.4 (a) The potential between the anode and the cathode and the (b) potentials versus Ag/AgCl reference electrode in solution with chloride and without chloride (trifluoromethanesulfonic acid and sulfuric acid)

Further validation is still necessary though Figure 5.4 suggests that chloride plays an important role in this sensor. In Figure 5.4, ΔE between the cathode and the anode was not a completely straight flat line as predicted. Auger can be one possible approach to validate that chloride adsorption was the key reaction on the cathode. If the auger element mapping shows that the chloride aggregates on the cathode more than the other two electrodes, we can confirm the existence of chloride adsorption.

The response time of the pH/ORP sensor was tested and the sensor responded faster than needed. The pH decrement in drinking water usually occurs slowly, and one unit change in pH may take days. The response time of the pH/ORP sensor presented in this dissertation is shown in Figure 5.5. The real time response of the pH and ORP sensor was recorded. HCl or NaOH was titrated into the test solution every 5 min to change the pH of the water (and unavoidably the ORP changed slightly). As shown in Figure 5.5, the sensor responded immediately (the recorded time includes the time of mixing the solution) in most situations. However the sensor seemed to need more response time around pH 7 ($1.35 < \Delta E < 1.45$ in Figure 5.5, noted that this plot was operated with 0.18 μA instead of 0.15 μA so the ΔE was higher than all the other Figures). The possible reason is because around pH 7, the concentration of H^+ and OH^- are both very low. Since water electrolysis is possible on the sensors, the reactions on the electrodes generated H^+ or OH^- and altered the local pH around the sensor. The local pH around the sensor was continuously changing, thus the response of the sensor drifted with time. This also gave a reasonable explanation to Figure 5.1 that the sensor fluctuated more around pH 7, which is the

pH value of pure water. The results suggested the sensor may not be able to measure exact pH but is definitely sufficient to alert the users when the pH is out of the normal range.
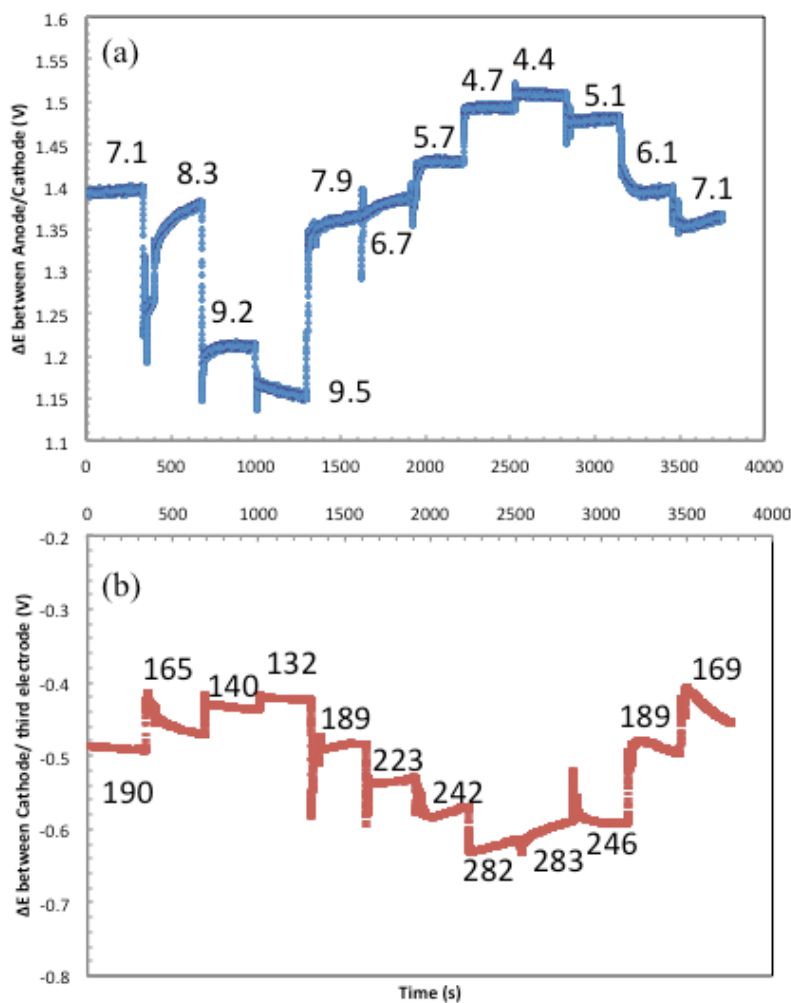
Figure 5.5 (a) The pH and (b) the ORP reading when the chemicals were titrated every 5 min to change the pH and ORP.

5.2.3   pH/ORP Measurement with Chloride Membrane in Extreme Condition

When the concentration of strong oxidants — of which hypochlorite is an example — is above 1 ppm, the potential on the cathode may change significantly and the pH/ORP sensor lose

its sensitivity. Application of a coating to the electrode surface could mitigate the limited sensitivity of the Pt/PtCl cathode in solutions of strong oxidants. Such oxidants, mostly hypochlorite salts, are commonly used in pools at around 7 ppm to increase ORP for sterilization. In section 5.2.1, this thesis introduces the pH/ORP measurement with bare platinum electrodes when HClO was below 1 ppm. As shown in Fig. 5.6., when the concentration of hypochlorite is above 1 ppm, the sensor loses its function for both pH (Fig 5.6. (a)) and ORP (Fig 5.6 (b)) measurement. Figure 5.7 shows that if the surface is coated with a PVC membrane containing an ionic liquid [23], the sensor can function in solutions with hypochlorite from 0 to 12 ppm. Noted that this coated sensor was operated with 0.20 µA instead of 0.15 µA.
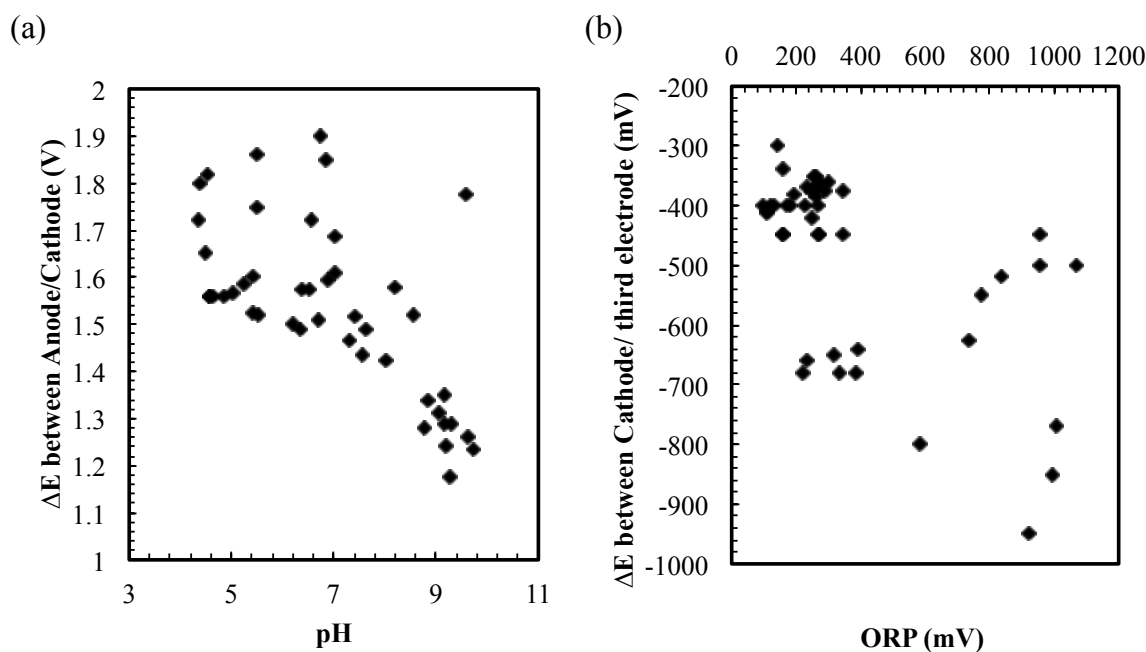
Figure 5.6 (a) The pH and (b) ORP reading when HClO concentration was above 1 ppm.
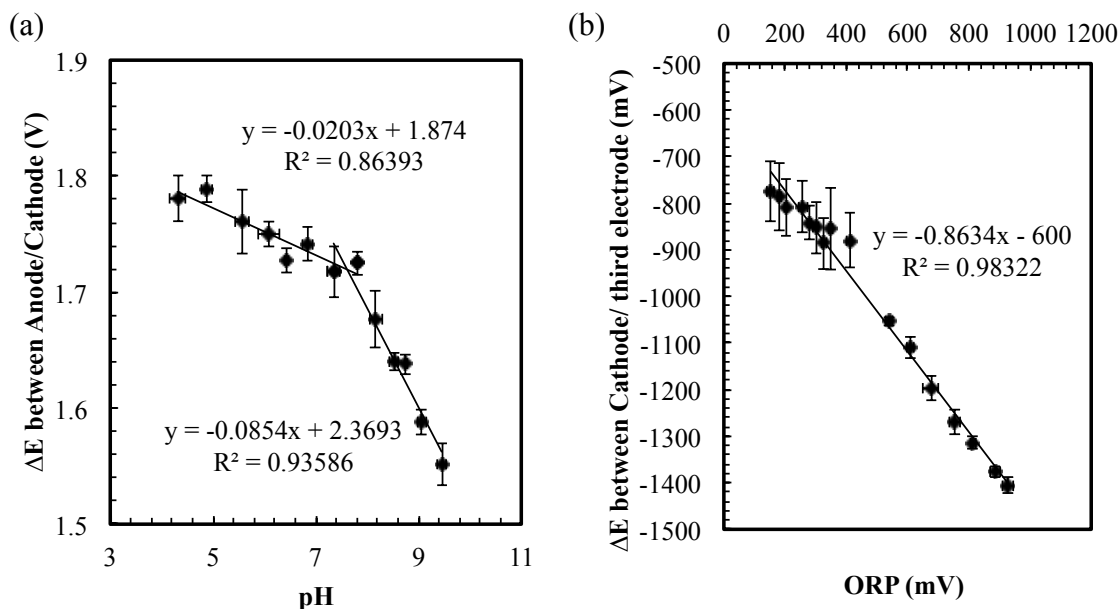
Figure 5.7 (a) The pH and (b) the ORP reading with chloride membrane with HClO concentration up to 12 ppm.

The chloride PVC membrane is impermeable to hypochlorite and keeps the potential on the cathode stable. As shown in Figure 5.8(a), when the sensor with bare electrodes was operated in test solution that HClO > 1 ppm, the potential on the cathode changed significantly. The potential of the cathode thus no longer served as a reference and the sensor lost its function. As shown in Figure 5.8(b), the PVC membrane blocked the influence of ClO⁻, and the sensor functioned normally. This enables applications of the pH/ORP sensor to residential water, public pools, and other fluids containing stronger oxidants around the 10 ppm level.
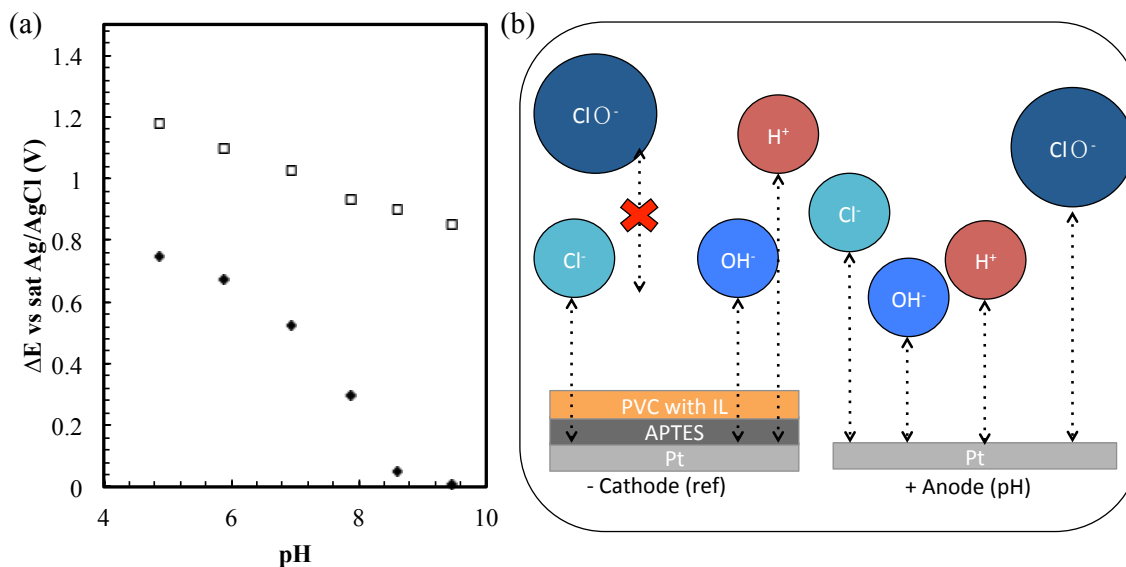
Figure 5.8 (a) The potential on the bare platinum electrodes when HClO > 1ppm and (b) the illustration of the membrane protection.

5.3 Summary of pH and ORP Measurement with Bare Electrodes

Simple bare platinum target sensor presented in this dissertation can be used to sense conductivity, ORP, and pH in aqueous solutions when provided the appropriate current. In this section, the pH/ORP sensor was tested in various conductivity, chloride concentration, pH, and ORP range. The sensor was also tested with the existence of common ions in residential water. The sensor is not extremely precise but it is capable of detecting if water is in the regulated range. The key element of this reference-electrode-free pH/ORP sensor is the relative stable potential on the cathode. The dominant reaction on the cathode is presumably the adsorption of chloride, which is partially validated in section 5.2.2, but further validation is still necessary.

Due to its simple fabrication with a single metal deposition, the device only costs about 10 cents, and flow sensors, temperature sensors, and heaters (for thermal cleaning) can be added onto the chip with little extra cost (Chapter 3). Having small electrode area ($ < 1$ mm^2) and inert

platinum electrode surfaces allows the sensor to be easily installed with little maintenance. Since pH and ORP change slowly in natural environment, the response time of this pH/ORP sensor is also proved to be shorter than needed.

If needed, PVC membrane can be coated on the sensor to compensate the influence of other ions for application in extreme condition, such as sanitizing solutions with high concentration of chlorine (the coated sensor can detect water with HClO up to 12 ppm). The sensor can also be used in microfluidic applications where a small electrode surface is required.

CHAPTER 6

Heavy Metal Sensors Focus On Lead Detection with only Bare Platinum Electrodes

6.1 Sensor Fabrication and Experimental Methods

6.1.1 Fabrication of the Electrodes

(a)   (b)   (c)
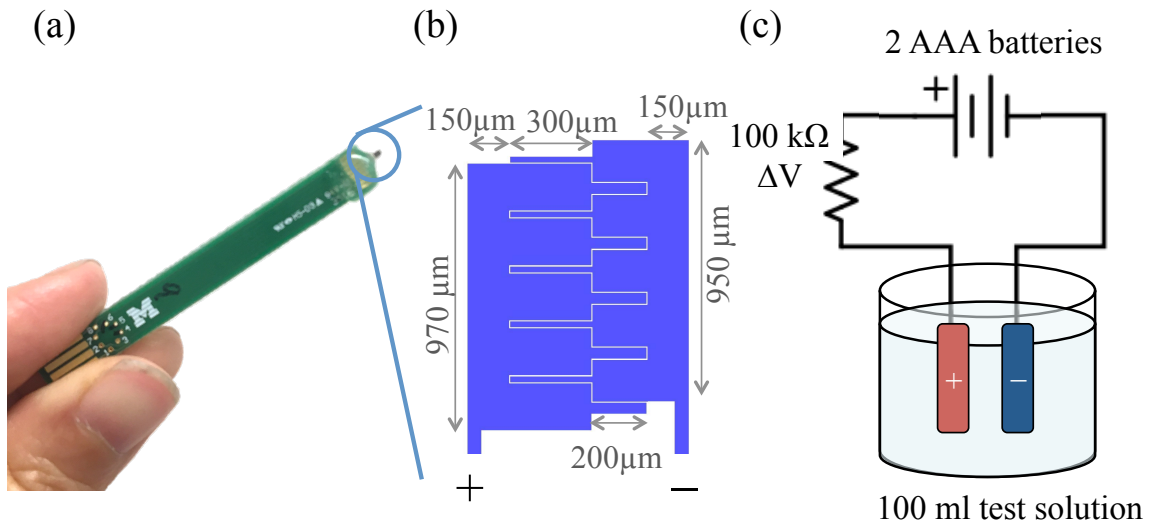
Figure 6.1 (a) The integrated sensor (b) two-electrodes sensor geometry and (c) the system schematic. The sensor was immersed in 100 ml test solution and connected with two AAA batteries and a 100 kΩ resistance. Voltage across the resistance was measured as the sensor output.

The sensor (Figure 6.1(a)-(b)) was constructed using physical vapor deposition of 300/1000 Å Ti /Pt on a 500 µm thick, 4 in diameter glass wafer. The pressure was controlled under 2×10^{-6} Torr with a deposition rate of 15 and 5 Å/s, respectively. The sensors were integrated with a PC board as shown in Figure 6.1(a). The two-electrode system is shown in Figure 6.1(b), and the electrodes were separated with a 5 or 10 µm gap. The four-electrode sensor was fabricated with the same method but in a different geometry as shown in Figure 6.2(a). The small gaps between the left two electrodes and the right two electrodes were 5 µm, and the large gap between the middle two electrodes was 50 µm.
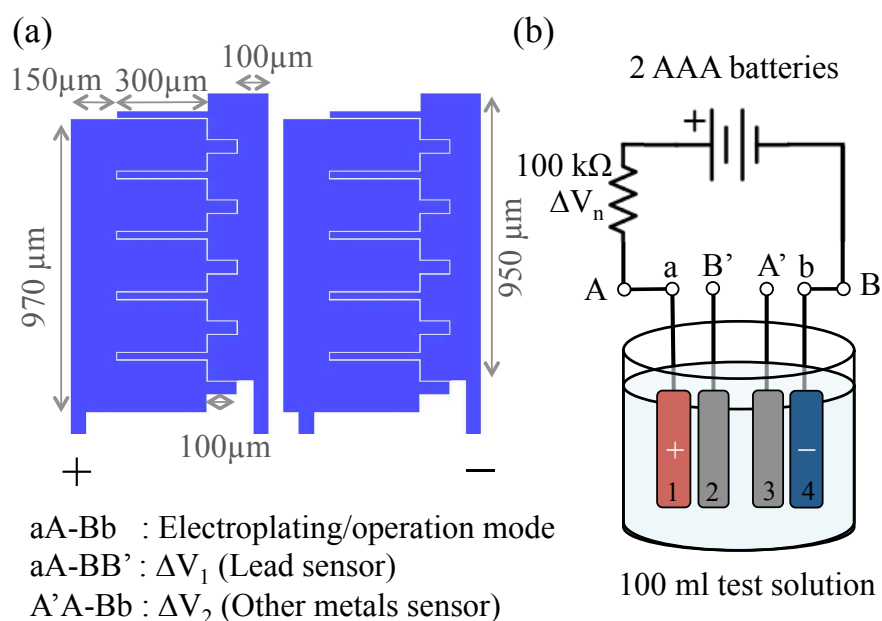
Figure 6.2 (a) Four-electrodes sensor geometry and (b) the system schematic. The sensor was immersed in 100 ml test solution as connected aA-Bb when it was operated. Voltage across the resistance was measured as ΔV_1 when connected as aA-BB' and as ΔV_2 when connected as A'A-Bb.

6.1.2   Experiment Setup and the Measurement of the Impedances

In Figure 6.1(c), the integrated two-electrode sensor was connected with two AAA batteries and a 100 kΩ resistor. The sensor was dipped in 100 ml test solution in a beaker. The

voltage difference across the resistor, ΔV, was measured by Labview as the signal. ΔV reflected the overall impedance across the electrodes: ΔV increased when the impedance across the two electrodes decreased. All solutions were changed every week during the experiments. The schematic diagram of the four-electrode system is shown in Figure 6.2(b). The sensor was connected with two AAA batteries and a 100 kΩ resistance. When the sensor was operated and electroplating metals, the sensor was connected as aA-Bb. The voltage difference across the resistor was measured as ΔV_1 when the sensor was reconnected as aA-BB' to measure the impedance between the anode and the second electrode. When the sensor was reconnected as A'A-Bb, the voltage difference across the resistor was measured as ΔV_2 to detect the impedance between the cathode and the third electrode.

6.1.3   Preparation of the Test Solution

Table 6.1 Ion concentrations in simulated tap water (Simultap) and real Ann Arbor tap water

Ion	Simultap (mg/L)	Ann Arbor (mg/L)
Na^+	270	48-67
K^+	11	--
Mg^{2+}	71	10-33
Ca^{2+}	46	23-66
HCO_3^-	61	--
CO_3^{2-}	14	100-176
NO_3^-	18	0-0.06
SO_4^{2-}	390	41-82
Cl^-	364	98-147

The simulated test solutions were made with $PbCl_2$, $CuCl_2$, $ZnCl_2$, and $FeCl_2$ in 10^{-2} M

NaCl made with DI water. The NaCl was added to increase the conductivity of the solution to

about 1000 µS/cm, the upper limit of drinking water set by EPA. The composition of the

simulated tap water (Simultap) and Ann Arbor tap water (information gathered from annual Ann

Arbor water quality reports 2003-2015) is listed in Table 6.2. Simultap contained relatively

higher concentrations of common ions than real tap water. The real sample Tap 1 and Tap 2 were

collected in Ann Arbor, Michigan, USA. The heavy metals in the real tap water samples were

examined with ICPMS and listed in Table 6.2:

Table 6.2 Concentration of heavy metals ions in tap water sample and EPA regulation

Metal	Unit	Tap 1	Tap 2	EPA regulations
Pb (NL)	ppb	ND	3.0	0 (MCL); 15 (AL)
Pb	ppb	ND	5.0	0 (MCL); 15 (AL)
Cu	mg/L	0.004	0.70	1.3(MCL); 1.0 (SMCL)
Zn	mg/L	0.004	0.59	5.0 (SMCL)
Fe	mg/L	0.003	0.033	0.3 (SMCL)
Al	mg/L	0.024	0.012	0.050 – 0.2 (SMCL)
Cr	mg/L	0.0002	0.0004	0.1 (SMCL)
Mn	mg/L	0.0001	0.005	0.05 (SMCL)
NL: National Testing laboratory ND: Not detectable (< 1ppb) MCL: Maximum contaminant level SMCL: Secondary maximum contaminant level AL: Action Level				

The lead concentration was tested both by ICPMS in University of Michigan and National

testing laboratory approved by EPA. Tap 1 contained no lead and relatively low concentration of

all heavy metals. Tap 2 contained about 5 ppb of lead, which is smaller than action level (15 ppb), and 0.7 mg/L of copper, which is relatively high but smaller than SMCL. $PbCl_2$ was added in Tap 1 to make the "Tap 1+ Pb150 ppb" sample but no extra NaCl was added.

6.1.4   The Operation of Auger Spectroscopy

The Auger spectroscopy data were collected for the specimens on a PHI 680 Auger nanoprobe that is equipped with a field emission electron gun and a cylindrical mirror energy analyzer (energy resolution $\Delta E/E \approx 0.25$ %).   The base pressure of the test chamber is around 1.2×10^{-9} torr. The native oxidized layer of the chromium pellet was removed by Ar ion sputtering. To avoid the charging effect of insulating samples under electron beam irradiation, Pb oxides powder with size less than 3 μm was pressed into a tin foil or a carbon type so that high energy electron beam can penetrate these lead oxide particles, while "devices" were placed on the tilt stage in order to reduce the embedded charging effect caused by the deep penetration of incident electron beam.   A small electron beam current of 1 nA was used to irradiate the specimens.

6.2 Results and Discussion of Bare-Electrode Heavy Metal Sensing

Simple sensors to detect heavy metal in drinking water can be achieved with simple platinum electrodes. When the electrodes are connected with 2 AAA batteries (~3.2V), heavy metal ions are reduced to conductive metals on the cathode. As shown in the list in Table 6 [67], the electric resistances of reduced metals are 9 to 10 orders of magnitude smaller than drinking water. Thus if the reduced metals connect the gap between the electrodes, the impedance across the electrodes drops significantly. The impedance change is an indicator of the existence of heavy metals in the solution.

Table 6.3 Resistivity of reduced and oxidized metal forms

Oxidized metal	Resistivity (Ω.m)	Reduced metal	Resistivity (Ω.m)
PbO_2	$2\text{-}74 \times 10^{-6}$	Pb	2.20×10^{-7}
ZnO	>2.2	Zn	5.90×10^{-8}
CuO	$25 - 100$	Cu	1.68×10^{-8}
Cu_2O	$10^2 - 10^4$		
$Fe(OH)_3/FeO(OH)/Fe(OH)_2/Fe_2O_3$	$10^3 - 10^6$	Fe	1.00×10^{-7}
Drinking water	$10\text{-}2000$	-----	

6.2.1 Two-Electrode Heavy Metal Sensing

A two-electrode sensor with 5 μm gaps can detect lead ions at a level of 15 ppb with no false responses. The performance of the 5 μm gap, two-electrodes system is shown in Figure 6.3(a) and a 10 μm gap sensor in Figure 6.3(b). For both sensors, ΔV increased significantly and became $> 1V$ within two days in 150 ppb Pb^{2+} solution. The growth of ΔV represented conductive layers formed between the two electrodes thus reducing the impedance. The sensor with a 5 μm gap showed response ($\Delta V > 1V$) in 15 ppb Pb^{2+} (action level) solution in three days, but the sensor with 10 μm gap showed no response throughout the two weeks experiment. This suggests a 5 μm gap between the electrodes is more sensitive than the larger gap. Both sensors had no false positive response from Simultap, showing common ions in water did not generate conductive species.
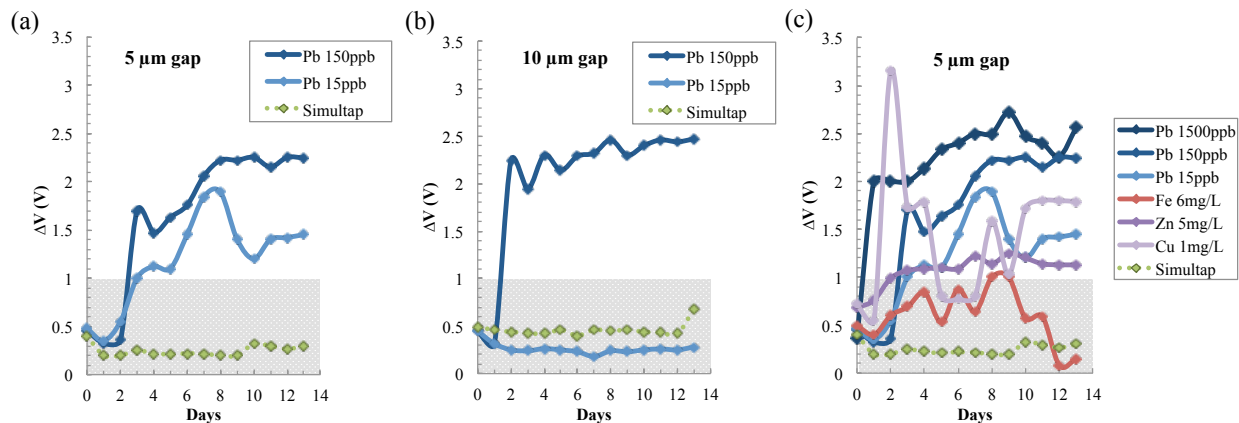
Figure 6.3 (a) Original reading of ΔV of the sensors with 5 μm gap and (b) 10 μm gap, and (c) ΔV of the sensor with 5 μm gap in various simulated solution

The two-electrodes sensor with 5 μm gap showed response to almost all solutions with heavy metals and showed no false positive responses. The sensor was tested in various simulated solutions designed to mimic the EPA heavy metal regulations listed in Table 6.2 [38], [39], and the performance is plotted in Figure 6.3(c). ΔV increased in all heavy metal solutions but remained the same in Simultap, which contained no heavy metal ions. The variation of ΔV was because some conductive deposition may fall off during the two weeks experiment, and the time ΔV remained >1V is not crucial. The sensor was also tested in two real tap water samples and a mixture of real tap water and lead. The performance in both the simulated and real samples is shown in Table 6.4. The solutions with lead higher than the action level are highlighted as blue and solutions with no heavy metal ions are shaded. The sensor showed fast response (<3 days) to lead, zinc, and copper solutions. No false positive response was generated in either Simultap or Tap 1.

Table 6.4 Two-electrode sensor performance in different solutions

	Solution	Response day (days)	Max ΔV (V)
Simulated sample	Pb 150 ppb	3	2.25
	Pb 15 ppb	3	1.89
	Fe 6.0 mg/L	9	1.00
	Fe 0.3 mg/L	13	1.01
	Zn 5.0 mg/L	2	1.25
	Zn 0.5 mg/L	3	1.27
	Cu 1.0 mg/L	2	3.15
	Cu 0.1 mg/L	1	3.20
	Simultap	--	0.4
Real sample	Tap 1	--	0.80
	Tap 1 + Pb 150 ppb	1	1.65
	Tap 1 + Pb 15ppb	--	0.60
	Tap 2	8	1.60

However, the responses in simulated ferrous solution and the mixture of real tap water and lead ions were slower than expected. The sensor generated slow and weak response (max ΔV = 1V at 9th day) in simulated ferrous solutions even at very high concentrations (20 times larger than SMCL). For the same 15 ppb Pb concentration, the sensor responded in 3 days in 15 ppb Pb solution but did not respond to the mixture of "Tap 1 + 15 ppb Pb". The sensor also responded more slowly to Tap 2 (0.7 mg/L Cu) than 0.1 mg/L Cu solution.

6.2.2   Operation of the Bare-Electrode Heavy Metal Sensor
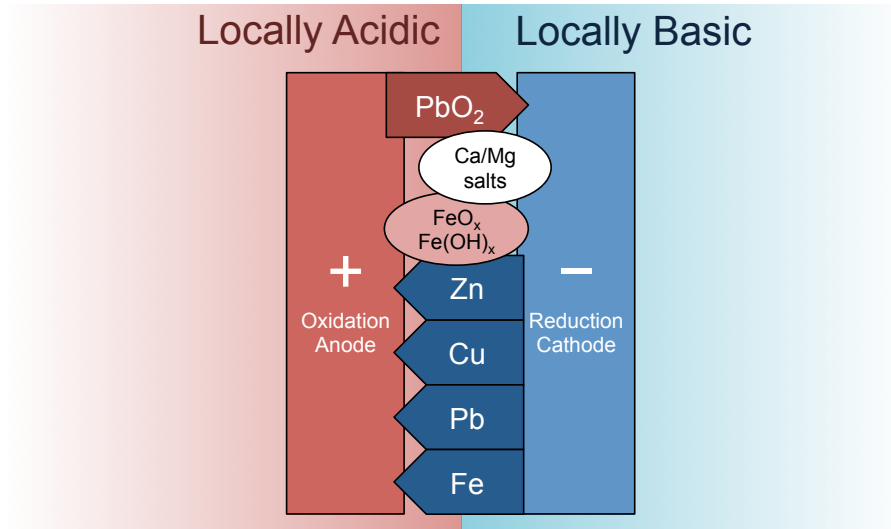
Figure 6.4 In two-electrodes system, metals reduce or oxidize into conductive species (draw as arrows). Some nonconductive salts and rust (draw as circles) also precipitates on the sensor.

The performance of the sensor can be explained with the help of Figure 6.4. The sensor shows response only if conductive deposition connects the gap and thus decreases the impedance between electrodes. The tendency of metal ions reducing to conductive metal can be represented by the standard reduction potentials, E^0. The higher the E^0, the easier the ions can be reduced. E^0 value of common metal ions in contaminated drinking water are listed in Table 6.5 [68]. E^0_{acid} is the E^0 in acid (pH=0) and E^0_{basic} is the value in basic (pH=14) conditions. Pb^{2+}, Zn^{2+}, Fe^{2+}, and Cu^{2+} can be reduced to conductive metals when the potential on the cathode is smaller than -0.76V [68]. With 2 AAA batteries, the potential on the cathode is sufficient to reduce the heavy metal ions.

Table 6.5 Standard potential E^0 of common metal ions and major ions in drinking water

Metal ions rxn	E^0_{acid}(V)	E^0_{basic}(V)	Major ions rxn	E^0_{acid}(V)	E^0_{basic}(V)
PbO_2/Pb^{2+}	1.46	--	Cl_2/Cl^-	1.40	1.36
O_2/H_2O	1.23	--	O_2/H_2O	1.23	--
Pt^{2+}/Pt	1.18	--	NO_3^-/NO_2	0.94	--
Fe^{3+}/Fe^{2+}	0.77	--	SO_4^{2-}/S	0.35	--
Cu^+/Cu	0.52	--	H^+/H_2	0.00	-0.83
Cu^{2+}/Cu	0.34	--	NO_3^-/NH_3	--	-0.12
$PbO_2/Pb(OH)_2$	--	0.25	CO_3^{2-}/CH_4	--	-0.73
H^+/H_2	0.00	-0.83	SO_4^{2-}/SO_3^{2-}	--	-0.94
Pb^{2+}/Pb	-0.13	--	Mg^{2+}/Mg	-2.36	--
Fe^{2+}/Fe	-0.44	--	Na^+/Na	-2.72	-2.72
Zn^{2+}/Zn	-0.76	--	K^+/K	-2.94	-2.94
			Ca^{2+}/Ca	-2.87	--

Lead ions are the only ions that can deposit a conductive species around the anode. The dominant reaction around the anode is oxidation, and lead is the only element that can be oxidized into conductive species — lead dioxide. Generation of lead dioxide is considered possible because the E^0 of PbO_2/Pb^{2+} is 1.46V (Table 6.5) [68][69]. Lead dioxide is considered conductive because its resistivity is about six to eight orders of magnitude smaller than drinking water and the other oxidized metals (Table 6.3) [67][70].

No false positive response is possible from typical ions in tap water. Concentrations of major ions in Ann Arbor, Michigan, tap water are listed in Table 6.1 as an example. Though the concentrations of ions vary from location to location, the species are mostly the same [71]. The

standard reduction potentials of these ions are listed in Table 6.5. Unless the cathode potential is smaller than -2.3V [68] (which is 1.4V smaller than the potential required to reduce the heavy metals), no conductive species are likely to deposit on the sensor surface and drop the impedance. With 2 AAA batteries, false positive responses are not likely.

Though false positive responses are unlikely, the performance of the two-electrode sensor may be delayed by precipitated hardness and rust. The solubility of water hardness, which is white with the major component being calcium carbonate, decreases with increasing pH [72]–[74]. With 2 AAA batteries (~3.2V), the sensor electrolyzes water during operation. Thus the local pH around the anode is acidic and basic around the cathode. Hardness precipitates on the cathode, blocking the gap between the electrodes, and delaying the sensor response. Rust, which is mostly ferric and ferrous oxide, is another precipitation that is possible due to altered pH [75][76]. Though E^0 suggests ferric and ferrous ions are possible to be reduced into iron, previous research shows the ions may instead precipitate as rust [75]–[77]. The ability of the sensor to detect iron is thus lower than the ability to detect other metals, so the sensor showed weaker and slower response in ferrous solution than in other heavy metal solutions.

Figure 6.5 showed the pictures of the sensors operated in different test solutions and corroborates the hypothesis described above. Lead was the only element deposited on the anode (+) while zinc and copper were reduced on the cathode (-). Simultap precipitated white hardness, and iron solutions precipitated red rust. Thus, the two-electrode sensor is ideal for heavy metal detection but can't distinguish lead from other heavy metals. Lead is the most toxic metal in drinking water and should be identified for the safety of the users.
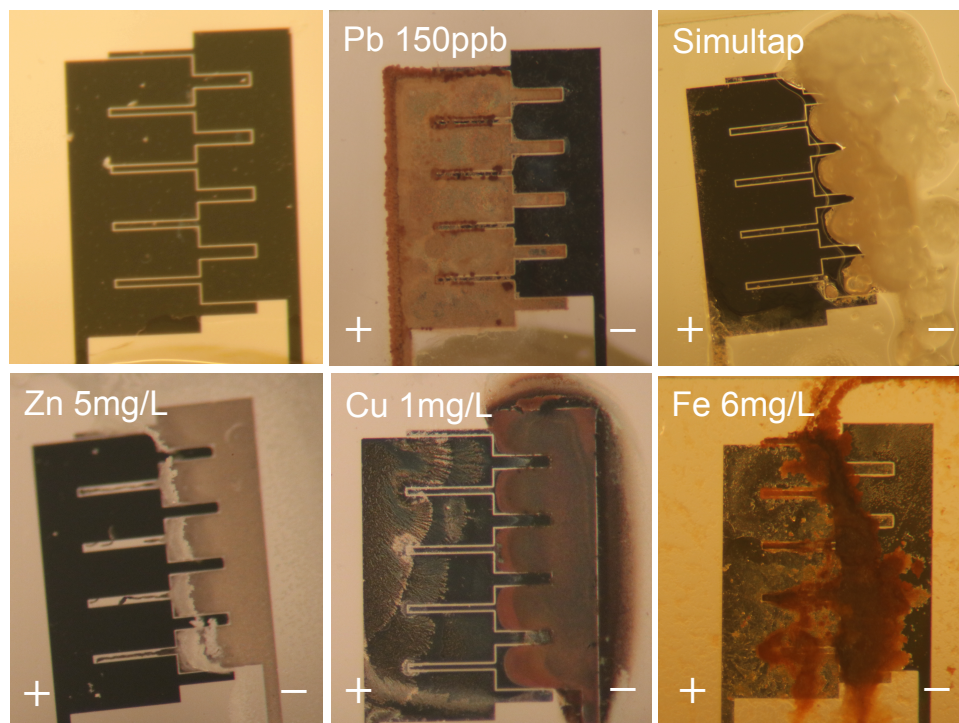
Figure 6.5 The original two-electrodes sensor (top left) and after it was operated in various solution. Lead deposited on the anode while all the other solution deposited or precipitate on the cathode.

6.2.3   Four-Electrode Bare-Electrode Heavy Metal Sensing

To distinguish the most toxic element, lead, from other heavy metals, a four-electrode sensor was designed and tested. Two extra electrodes are placed between the cathode and the anode as shown in Figure 6.2(a). The small gap between the left two electrodes and the right two electrodes was 5 μm. The large gap between the middle two electrodes was 50 μm. As explained previously, lead ions are the only ions that will deposit a conductive species around the anode while other heavy metals can still deposit on the cathode. The four-electrode sensor thus contains both a lead detector and a heavy metal sensor.

The expected reactions in the four-electrode system are illustrated in Figure 6.6. Lead ions oxidize to lead dioxide around the anode and connect the gap between the anode and the

second electrode. At the cathode, other metals are reduced, and hardness and rust precipitate due to pH change. Since lead is the only ion that can be oxidized to a conductive species in the system, lead is the only element that deposits a conductive compound around the anode. The two electrodes on the left are thus lead detectors and the two electrodes on the right are other heavy metal sensors.
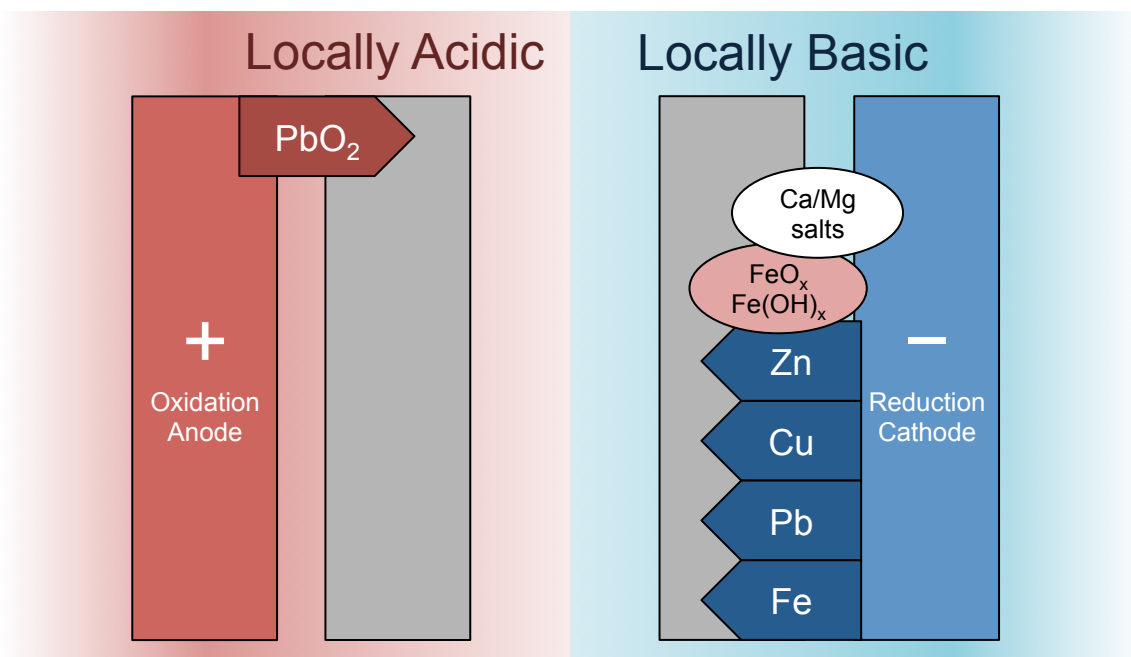
Figure 6.6 In four-electrodes system, lead oxidizes into conductive lead dioxide on the anode, and metals reduce into conductive species (draw as arrows) on the cathode. Nonconductive salts and rust (draw as circles) also precipitates on the cathode.

The concept was confirmed with experiment results and had no false positive response on both sides in simulated and real tap water. The original reading of the four-electrode system is shown in Figure 6.7. Both ΔV_1 and ΔV_2 maintained < 1V in Simultap and Tap 1. ΔV_1 increased significantly in both Pb^{2+} solutions, and showed no false positive response to high concentrations of zinc and iron. ΔV_2 detected the existence of all other heavy metals and increased significantly in Zn^{2+}, Cu^{2+}, and Fe^{2+} solutions. ΔV_2 did not respond in 15 ppb Pb^{2+} because the low ion concentration and most of Pb^{2+} was oxidized on the anode.
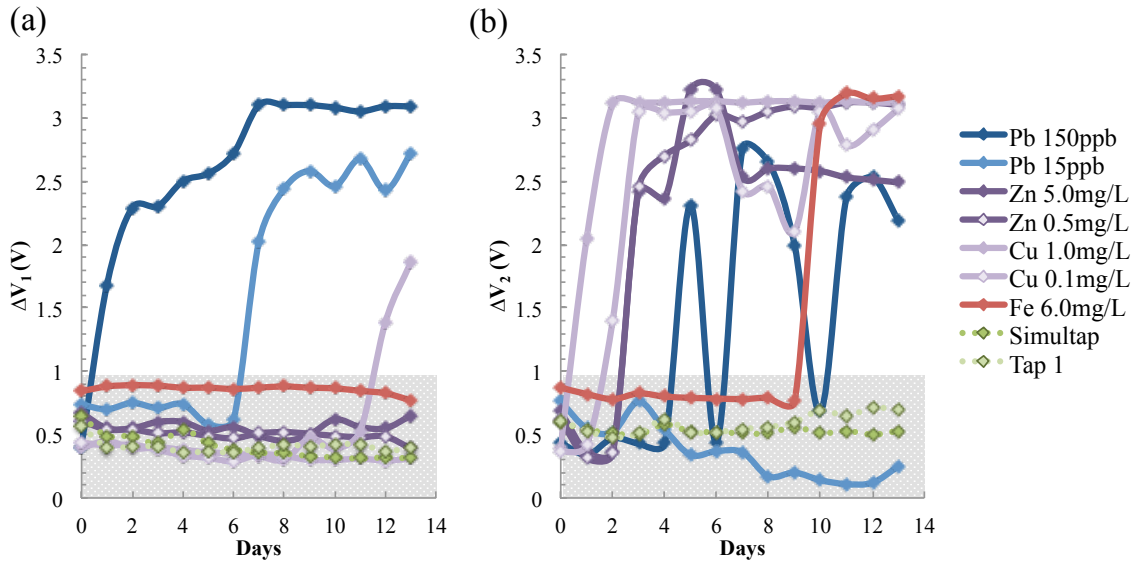
Figure 6.7 (a) The original ΔV_1 reading at anode side and (b) ΔV_2 reading at cathode side in different solutions for two weeks.

One downside is that copper, which is also a toxic metal regulated by EPA MCLs, can generate a false response on the lead detector. A late response (12th day) on ΔV_1 appeared in the 1 mg/L copper solution. This response occurred because copper is the easiest ion to be reduced among the four metal ions (Cu^{2+}/Cu is 0.34 V as listed in Table 6.5 [68]). On the anode, oxidations were the major reactions and few reductions happened due to the forced electrical current. However, both oxidation and reduction were possible on the middle two floating electrodes, which meant that copper could be reduced on these two electrodes as well. When copper was reduced on the second electrode, the anode and the electrode may be connected. The impedance between these two electrodes dropped significantly, ΔV_1 increased, and a false positive was generated.

The lead detection using the four-electrode sensor can occur without being influenced by the main ions in the tap water. Table 6.6 listed the performance of the four-electrode sensor in various solutions. The solutions with lead higher than the action level were highlighted as blue and solutions with no heavy metal ions were shaded. The lead sensor detected all solution with

lead above the action level though the low concentration (5 ppb) of lead in Tap 2 was not detected. The ability for lead detection was not influenced by the major ions in the solution. Since the hardness was precipitated around the cathode due to pH change and it was not blocking the lead detector, the response days for the action level sample "15 ppb Pb" is the same with the real tap water sample "Tap 1 + Pb 15ppb". On the other hand, the heavy metal sensor was delayed by the harness precipitated around the cathode. For the same concentration of lead, copper, and zinc, the sensor detected much faster (1 days) in a simulated solution than in the mixture of heavy metals and real tap water. The heavy metal detector also showed no response to Tap 2, which contained a relatively high concentration of copper (0.7 mg/L).

Table 6.6 Four-electrodes sensor performance in different solutions

	Solution	ΔV_1 Anode		ΔV_2 Cathode	
		Response day	Max ΔV (V)	Response day	Max ΔV (V)
Simulated Sample	Pb 150 ppb	1	3.10	5	2.76
	Pb 15 ppb	7	2.72	--	0.76
	Fe 6.0 mg/L	--	0.89	10	3.19
	Zn 5.0 mg/L	--	0.67	3	3.22
	Zn 0.5 mg/L	--	0.61	3	3.12
	Cu 1.0 mg/L	12	1.86	1	3.13
	Cu 0.1 mg/L	--	0.44	2	3.07
	Pb 15ppb + Cu 1mg/L + Zn 5mg/L	2	2.99	1	3.21
	Simultap	--	0.31	--	0.59
Real Sample	Tap 1	--	0.57	--	0.71
	Tap 2	--	0.69	--	0.70
	Tap 1 + Pb 150 ppb	2	3.05	--	0.56
	Tap 1 + Pb 15ppb	7	2.14	12	2.4
	Tap 1+ Pb 15ppb + Cu 1mg/L+ Zn 5mg/L	9	1.36	5	3.02

6.2.4 Validation with Auger Spectroscopy

The compositions of the metal depositions on the anode and cathode are confirmed by using Auger electron spectroscopy (AES). AES is a surface-sensitive characterization technique based on the analysis of energetic electrons emitted from an excited atom after a series of internal relaxation events [78]. The energy position and shape of an Auger peak contains a significant amount of information about the chemical environment of the source ion. This chemical information results from the dependence of the atomic energy levels, the loss structure, and the valence band structure on the local bonding. Compared to the high and slowly changing backscattered electron background, the Auger peaks usually look small. Commonly the first order derivatives of the spectra are employed to highlight chemical changes.
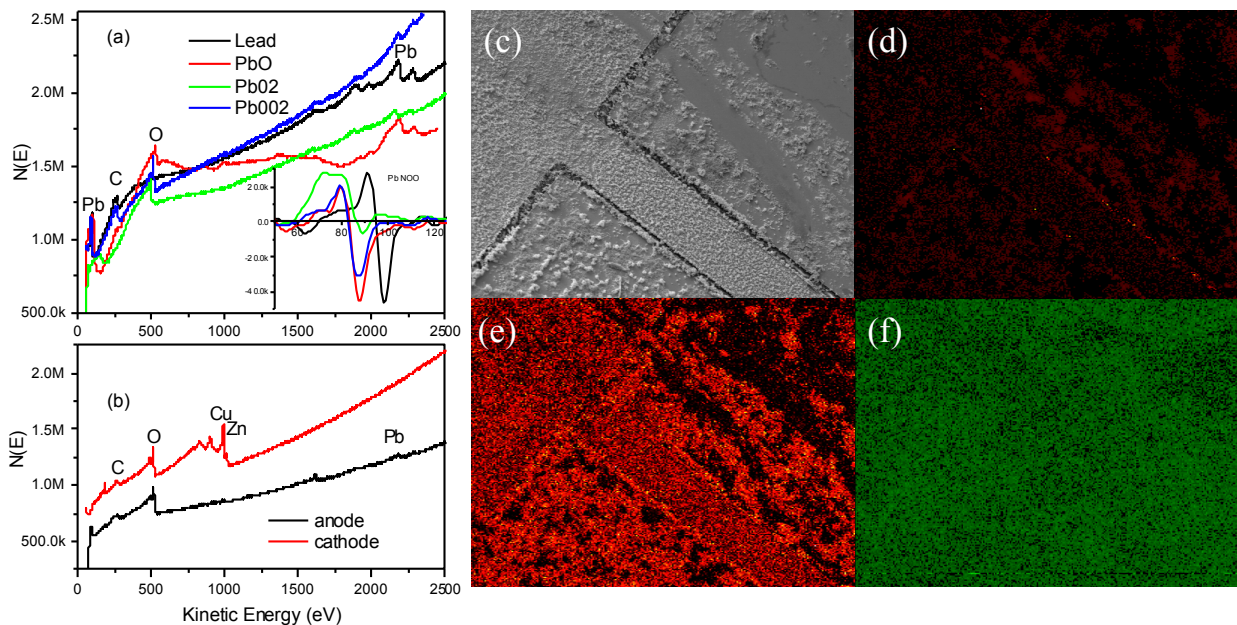
Figure 6.8 Auger electron spectra of (a) standard metal lead, standard lead (II) oxide, sample Pb02 and Pb002. The inset expands the Pb *NOO* Auger transitions in the first order derivative. (b) The AES profiles of anode (black curve) and cathode (red curve) of the sample Mix 5. The (c) SEM image and Auger electron mapping at Pb, (d) NOO, (e) MNV transition peaks from the sample Pb02 and (f) mapping at O element NOO peak under the electron impact of 10kV and 10nA.

The chemical states of the lead deposition on the anode can be validated by comparing the kinetic energy of the valence band Auger electrons. In the experiment, 99.99% Pb and 99.999% PbO were purchased from Sigma Aldrich and used as validation standards. Pb02 was the sensor anode operated in 150 ppb Pb solution for two weeks and Pb002 was in 15 ppb. As seen from Figure 6.8(a) (inset), electron beam excited Pb ONN Auger transitions show high sensitivity to the chemical states. The metallic Pb ONN Auger electrons (98.0 eV) have higher kinetic energies than those of PbO (87.6 eV) and the specimen (86.5 eV). Similar observations also occur at Pb MNV transitions (1800~2300 eV) in the raw data (Figure 6.8(a)). The kinetic energy of the Auger electron depends only on the energy levels involved, however, not on the energy of the primary excitation. These energy levels relate to the type of atom and the chemical environment in which the atom was located. The energy levels are element specific, so that the Auger electrons emitted by the sample carry information about their chemical composition. The resulting spectra can be used to determine the identity of the emitting atoms and some information about their environment. Basically the inner shell energy levels are much less affected by the chemical states, so the kinetic energy of the valence band Auger electrons can directly reflect the chemical states of the source ions.

The other approach to validate the chemical status is the Auger peak intensities, and with the NOO positions we can conclude that the deposition on the anode had PbO_2. The Auger peak intensities are determined by the ionization cross section, Auger yield possibility, the mean escape depth and the backscattering factor [79]. It is quite difficult to individually quantify these factors. Usually the intensity (peak-to-valley height) of AES peaks can be simplified to the product of a sensitivity factor and the concentration of the element. Based on the sensitivity factors for O and Pb elements derived from the standard PbO, the atomic concentration ratio of

the specimens can be calculated from their peak-to-valley heights (see Table 6.7). Combining the

peak Pb NOO position [80], [81], it can be concluded that the deposition in 15 ppb Pb solution is

mainly PbO_2 while a mixture of PbO_2, PbO, and Pb in 150 ppb solution.

Table 6.7 The averaged atomic ratio obtained from AES data of selected spots. The errors for all elements are estimated to be 5%.

Specimen	C	O	Pb	Zn	Cu	Na	Cl	O/Pb
Pb	-	-	100	-	-			
PbO	31.3	34.4	34.3	-	-			1.0
Pb02 (150ppb)	15.4	37.9	22.8	-	-	11.9	11.8	1.7
Pb002 (15ppb)	55.2	17.2	8.4	-	-	10.2	10.1	2.1
Mix (anode +)	30.5	45.4	29.1	-	-	-	-	1.6
Mix (cathode -)	15.5	34.4	-	40.9	6.8	-	-	

As seen from Figure 6.8(b), when the sensor operated in the mixed solution "Pb 15ppb +

Cu 1mg/L + Zn 5mg/L", most Pb deposited on the anode while Cu and Zn deposited on the

cathode. No Pb (or trace amount of Pb) deposited on cathode confirming that our sensor has high

elemental selectivity. The atomic ratios were listed in Table 6.7, which are the average of 5

different spots in order to provide the reproducibility. The errors for all elements are estimated to

be 5 %.

In-gap deposition of Pb species was confirmed with Auger element mapping. The

electron-excited Auger electron spectroscopy provides very high spatial resolution (~10 nm),

which enables it especially suitable for the small feature analysis and elemental mapping. Sample

Pb02 (the sensor in 150 ppb for two weeks) was mapped using Pb NOO and MNV Auger

transition peaks. The SEM image in Figure 6.8(c) and Pb NOO peak in Figure 6.8(d) illustrated

high concentration of lead is deposited in the gap. The left-up side in the image was the anode while the right-down side was the second electrode. Figure 6.8(d) showed Pb signal is stronger in the gap. Pb MNV peaks in Figure 6.6(e) showed Pb distributed all over the electrodes except the scratch on the right-up side, and the distribution matched the SEM image in Figure 6.8(c). The mapping of O element in Figure 6.8(f) showed O was all over the electrodes.

6.2.5 Long-Term Monitoring of the Four-electrode Sensor
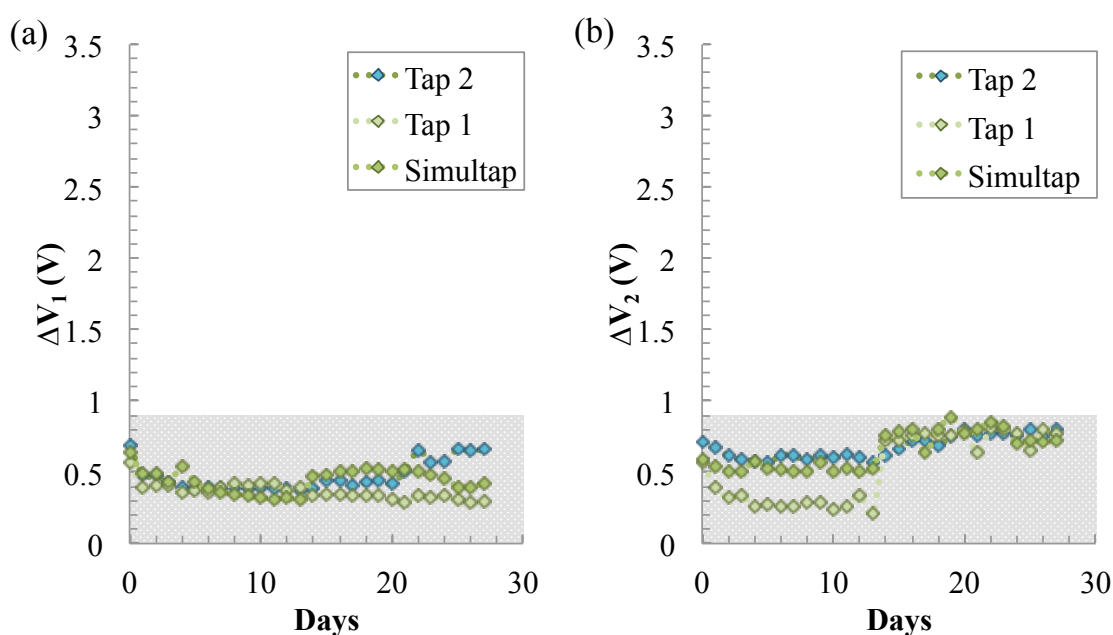
Figure 6.9 (a) The original ΔV_1 reading at anode side and (b) ΔV_2 reading at cathode side in contaminated tap, tap, and simulated tap water for four weeks.

Heavy metals can leak into water without of the awareness of users and thus on of the most important features of heavy metal sensors is continuous long-term monitoring. To achieve this goal, the sensor needs to be stored or operated in solution for long periods of time and still function normally. The sensors discussed here are ideal such operation because the inert electrodes suggest no lifetime limitation. As shown in Figure 6.9, both sides of the sensor

performed well in Simultap, Tap 1, and Tap 2 after the sensor was operated continuously for four weeks. The sensor also functioned normally after storage in solution for two weeks, as shown in Figure 6.10(a) and (b). In Tap 1, 15 ppb Pb, and 150 ppb Pb solution, the impedances of the sensor on both side remained relatively constant during storage (immersed in the solution without any supplied voltage) and the sensor functioned normally after activation. $\Delta V1$ on the lead detection side increased significantly (>1V) in both 15 ppb and 150 ppb lead solution but both $\Delta V1$ and $\Delta V2$ remained < 1V in tap water. In Figure 6.10(c), the sensor was operated (on) in Tap 1 for two weeks and then stored (off) in Tap 1 for another two weeks. Hardness precipitated on the cathode during operation mostly dissolved after the storage, thus both the lead detector and the other heavy metal sensors remain unblocked and the sensor can be used again.
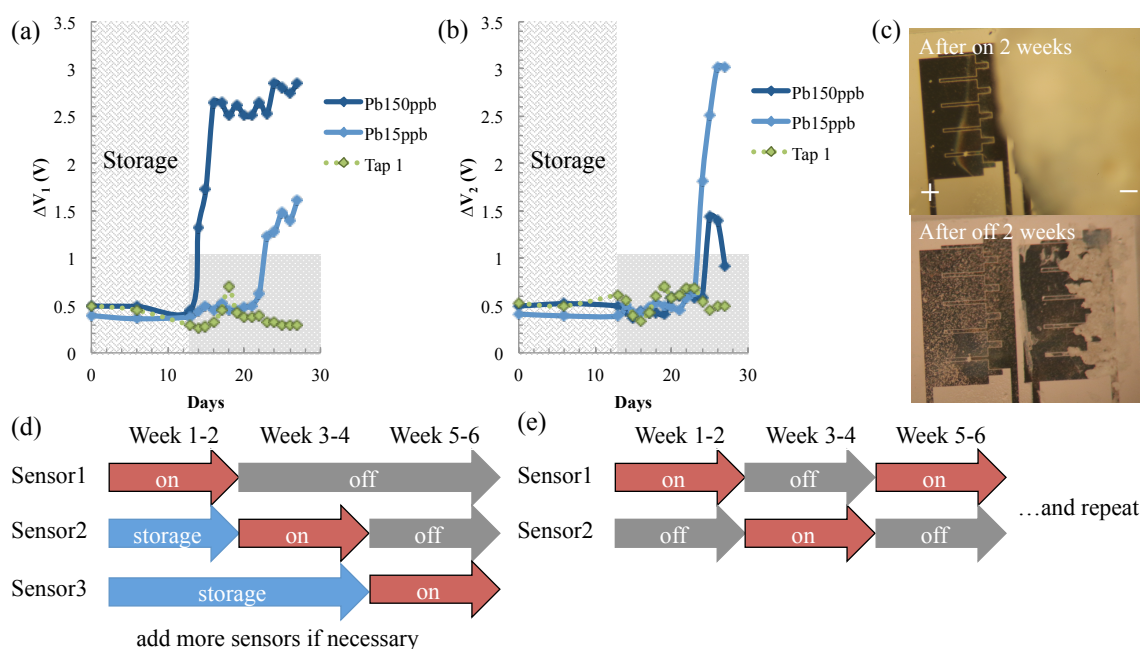
Figure 6.10 The sensor was stored in tap water, 15 ppb, and 150 ppb Pb solution for two weeks and still function normally on both (a) anode side and (b) cathode side. (c) Hardness precipitated on the cathode side after the sensor was on for 2 weeks but mostly dissolved again after the sensor was off for 2 weeks. The sensor can be used for long-term monitoring through two approaches: (d) multiple sensors in the pipelines or (e) two sensors operating alternatively.

90

These experiments suggest that long-term monitoring is possible using two methods. The first approach, as shown in Figure 6.10(d), is to put multiple electrode combinations on a single sensor. The surface area of the sensor is less than 1 mm^2 but duplicate sensors can easily be constructed on this or slightly larger formats. If necessary, wax or other materials can be applied to the sensors during storage to protect the sensor's surface. The materials can be easily removed just before operation with embedded Ti/Pt heaters to melt and remove the material. The other approach, as shown in Figure 6.10(e), is to alternate two sensors. One sensor operates for two weeks while the other is immersed in the same solution with no applied power. The alternation of the sensors can be programmed and operated automatically, and the sensors without applied power will regenerate through dissolution of precipitated ions.

More sensors were tested to validate the long-term monitoring possibility of the sensors. The sensors functioned normally after six week of storage and operation. In Figure 6.11, total six sensors were tested for two-month monitoring experiment. For the first four weeks, "Tap 1A-B" were stored and operated in Tap 1, "Pb 15 ppb A-C" in 15 ppb Pb test solution, and "Pb 150 ppb" in 150 ppb Pb test solution. No false response was generated during sensor storage. After the sensors were turned on, all the sensors in lead solution showed response, and no false response was generated on Tap 1A-B. The 5th and 6th week, Tap 1A-B were stored in Tap 1 solution again. After 6 weeks, the sensors were turned on when Tap 1A was in 5 mg/L Zn and Tap 1B in 15 ppb solution. The other heavy metal sensors (the cathode side) on Tap 1A showed response the next day, and the lead sensor (the anode side) on Tap 1B showed response at the 8th day. The experimental result showed the sensors functioned perfectly after 6-week operation and storage. On the 45th day Tap 1A was moved to 15 ppb Pb solution to test if the sensor can still detect Pb. However the sensor burned out before lead response. The primary packaging of these

sensors was epoxy covering the bonded wires. The epoxy is not ideal to prevent water leakage or the heat dissipation of the wirebond thus causes sensors failure. The water insulation and heat dissipation should be improved in the future packaging of these sensors.
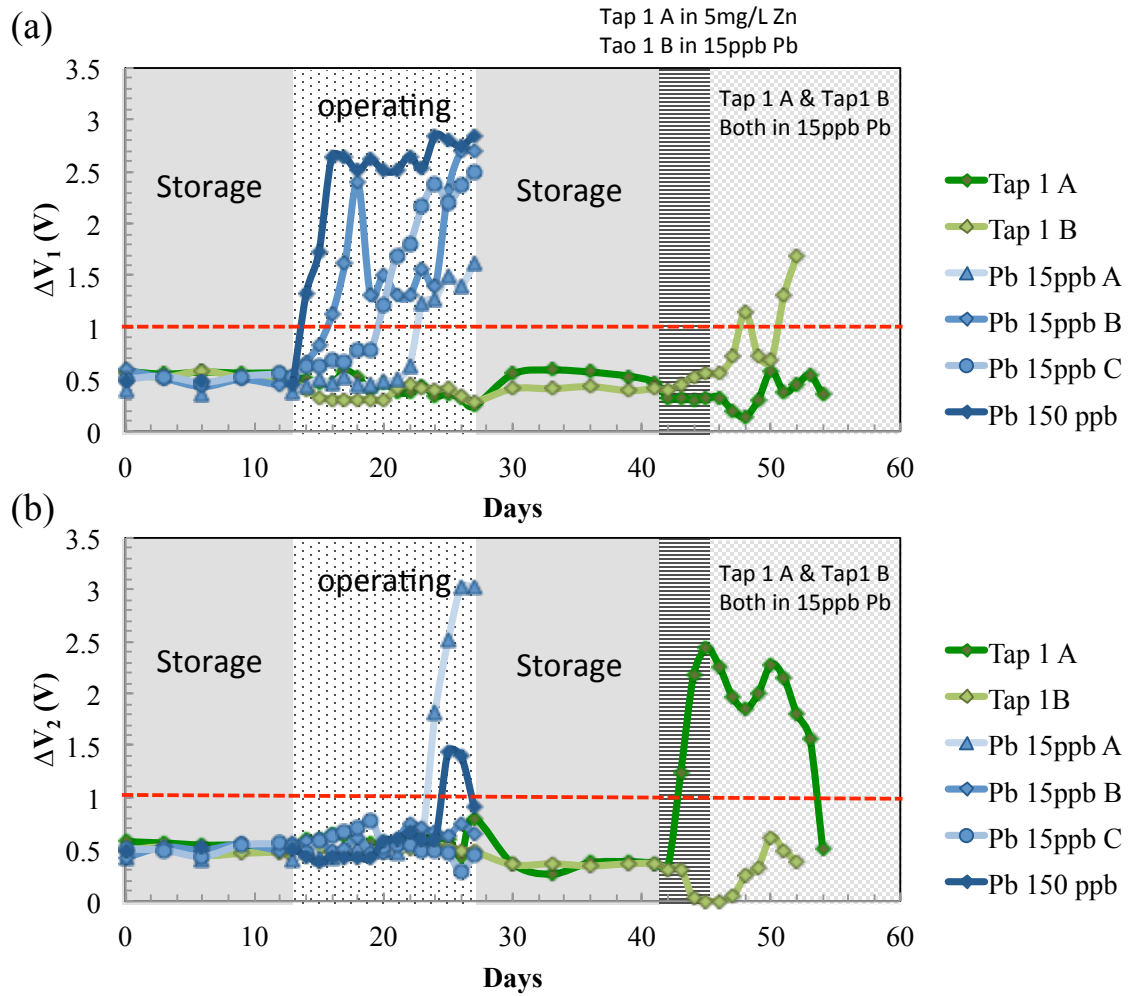
Figure 6.11 Two-month operation of 6 sensors until they responded or burned out for (a) lead and (b) other heavy metal sensing.

It is important to note that the sensors presented here are ideal for qualification of lead but not necessarily for quantification. Although somewhat quantitative, the response day of the sensor does not necessarily represent the concentration of lead or other heavy metals. For example, the response day for 15 ppb Pb solution in Figure 6.7 is 7 days but 9 days after turned

on in Figure 6.10. In Figure 6.11, three sensors in 15 ppb Pb showed response at 2nd, 6th, and 9th day, of which the average was 5.7 day and the standard deviation was 3.5 days. However, for water safety monitoring, real-time detection of the action level of lead or other dangerous heavy medals is extremely important, and quantification of that level can occur off-line.

6.3 Summary of the Bare-Electrode Heavy Metal Sensing

The sensor presented in this paper can help detect contamination of lead or other heavy metals in a variety of applications. The four-electrode sensors detect lead on the left two electrodes and detect other heavy metals on the right two electrodes. The inert platinum electrode and the experiment results suggest the sensor has a potential long lifetime, and the sensor can be easily inserted in pipes for continuous monitoring and detection. Instead of quantification, the sensor performs excellent qualification which is important in the monitoring of lead contamination. Toxic lead exposure causing permanent injuries through contaminated tap water has been a concern in the US, and the sensor proposed in this paper can be a possible solution to detect such lead outbreaks. However, the label-free bare-electrode sensors still need further research for optimization and broad applications.

For example, it is possible to shorten the response time of this sensor by changing the sensor geometry. The crucial sensing method of this sensor is to grow reduced metal or lead dioxide bridges in the gap between the electrodes to change the impedance. To raise the bridge-formation possibility and shorten the response time, we can increase the length-to-surface-area ratio or decrease the gap distance between the electrodes. The current electrode design causes lots of heavy metal ions deposit on the electrode surfaces instead of in the gap. Thus by increasing the length-to-surface-area ratio, we can increase the possibility of conductive bridge formation.

Sensors with smaller gap not only have shorter response time but also are possible to detect Pb^{2+} at lower concentration (< 15 ppb action level). These sensors may be suitable for trace lead detection in human urine, but they can generate noisy response in residential water far lower than MCLs and SMCLs. Further, the smaller the gap, the more difficult it is to fabricate the sensor.

Due to the simple sensor geometry and the high possibility for long-term monitoring, we believe this paper can trigger lots of follow-up research in other common heavy metal detection such as Ni^{2+}, Co^{2+}, Cr^{3+}, Hg^+, and Cd^{2+}. Some research has been done to predict the sensor performance of detecting these metals. According to the E^o and resistivity of these heavy metals in Table 6.8 and Table 6.9 [68], [82]–[86], Hg, Co, Cr, Cd, Ni are possible to be detected on the cathode side, while Cr is possible to be detected on the anode side (lead sensor). Since E^o of CrO_2/Cr^{3+} is a 200 mV larger than PbO_2/Pb, the oxidation of lead is more favorable, and the anode side should be more sensitive to Pb^{2+}. Pb and Cr may be distinguished by strict potential control on the anode, but more follow-up research should be investigated in the future.

Table 6.8 E^o of the other heavy metals

Metal Ion Reaction	$E^0_{acid}(V)$	$E^0_{basic}(V)$
CrO_2/Cr^{3+}	1.70	0.20
Hg^{2+}/Hg	0.65	--
Hg_2^{2+}/Hg	0.39	--
Ni^{2+}/Ni	-0.24	-0.70
Co^{2+}/Co	-0.28	-0.75
Cd^{2+}/Cd	-0.40	-0.83
Cr^{3+}/Cr	-0.74	-1.36

Table 6.9 Resistivity of the other heavy metals and metal oxides

Oxidized metal	Resistivity (Ω.m)	Reduced metal	Resistivity (Ω.m)
CrO_2	~3 x 10^{-6}	Cr	1.3 x 10^{-7}
HgO	---	Hg	9.6 x 10^{-7}
NiO	~10^{-3}-0.65	Ni	7.0 x 10^{-8}
Co_3O_4	10^2 - 10^4	Co	5.8 x 10^{-8}
CdO	0.42	Cd	7.3 x 10^{-8}

CHAPTER 7

Conclusions and Future Work

7.1 Summary of the Developed Sensors

This dissertation developed sensors for seven key variables of drinking water safety: flow-rate, temperature, ionic conductivity, pH, ORP, lead ions, and other heavy metal ions. Instead of focusing on precise and fast-responding sensor, this dissertation focuses on sensors that are suitable for long term monitoring. There are often tradeoffs between sensor accuracy and lifetime, as well as between sensor sensitivity and fabrication cost. This dissertation developed sensors that are cost efficient, theoretically long-lasting, and suitable for residential water monitoring.

In chapter 3, the dissertation presents a thermal flow-rate sensor that is integrated with a temperature sensor and can measure large flow-rates up to 2 GPM (~0.1 L/s) in 10 to 50 ˚C water. The sensitivity of this sensor is improved by lowering the sensing surface area A_c and by reducing conductive heat transport in the substrate from material selection. Responding to velocity between 10 to 250 cm/s, the sensor can also measure 0.2 to 7.8 mL/s water in 150 μm wide micro-channels or 2 to 78 L/s water in 6 inch diameter municipal pipes. Thus the sensor can span over 5 orders of magnitude in flow rates. And the sensors are fabricated with platinum, a metal that has not only the sufficient TCR for the flow-rate sensors to function but also the

inert property to be used for other purposes such as water-sensing electrodes. The simple structure and material of the flow-rate sensor make it easy for integration and cost-efficient in fabrication.

In chapter 4, the conductivity sensors are optimized for residential water measurement considering the sensor cost, the sensor size, and the integration with other sensors. The final design is a two-electrode conductivity sensor that has only bare platinum electrodes. The geometry of this sensor is a three-electrodes target sensor but only the outer two electrodes were used in the conductivity measurement. The conductivity sensor shares the same geometry with the pH/ORP sensor (in Chapter 5) so the same sensor can measure all of the three variables. The experiments results suggests dielectric layers are not necessary for the interested region, so the conductivity sensor has only bare platinum electrodes and can be easily integrated with other sensors presented in this dissertation. Various supplied voltage are also studied but no obvious difference is observed. The optimized target conductivity sensor is supplied with 6200 Hz, 0 - 0.5 V pulsed square wave on the outer two electrodes.

In chapter 5, the simple bare platinum target sensor can measure pH and ORP simultaneously in various conductivity and chloride concentration. This section uses the same target sensor in chapter 4 to sense pH and ORP in aqueous solutions. The sensor is provided DC current in suitable range instead of pulsed voltage. The sensor is also tested in different compositions of common residential ions with and without strong oxidants. The sensor is not extremely precise but it is capable of detecting if the water is in the regulated pH and ORP range. The key element of this reference-electrode-free pH/ORP sensor is the relative stable potential on the cathode. The dominant reaction on the cathode is presumably the adsorption of chloride, which is partially validated in section 5.2.2, but further validation is still necessary. If needed,

PVC membrane can be coated on the sensor to compensate the interference of other ions for applications in extreme conditions, such as sanitizing solutions with high concentration of chlorine. The coated sensor can detect water with HClO up to 12 ppm while uncoated sensor can only be operated with HClO smaller than 1 ppm. Since pH and ORP change slowly in natural environment, the response time of this pH/ORP sensor is also proved to be shorter than needed.

In chapter 6, the sensor presented in this section detects lead and other heavy metals in residential water by reducing or oxidizing the metal ions into conductive bridges between the electrodes. The two-electrode heavy metal sensor can detect heavy metals but the sensor is interfered by other major ions in the water. On the other hand, the four-electrode heavy metal sensor can distinguish lead from other heavy metals and the lead detection is not interfered by major ions. The inert platinum electrodes and the experimental results suggest the sensor has a potentially long lifetime, and the sensor can be easily inserted in pipes for continuous monitoring and detection. Instead of quantification, the sensor performs excellent qualification, which is important in the detection of lead leakage and contamination. Toxic lead exposure causing permanent injuries through contaminated tap water has been a concern in the US, and the sensor proposed in this section can be a possible solution to detect such lead outbreaks.

With the simple structures, all sensors presented in this dissertation can be easily and cost-efficiently integrated. All sensors are fabricated on glass substrates, with only a single layer PVD Ti/Pt. The glass substrate offers decent thermal isolation, thus the heat generated on the flow sensor barely changed the temperature on the conductivity and the other sensors. (Figure 3.3 in Chapter 3). The small sensing area (total < 3 mm^2) and inert platinum electrode surfaces allow the sensor to be easily installed with little maintenance. Extra heaters or electrodes (for thermal and electric-field cleaning) can be added onto the chip with little extra cost. Due to its

small feature and simple structure, an integrated device quipped with all presented sensors should cost only about 10 cents.

7.2 Possibility of Long-Term Monitoring with the Microorganism in Water

MEMS sensors are very popular in many fields but lots of them encounter obstacles from microorganism interference in real applications. Due to chemical treatments, drinking water distribution system (DWDS) usually contains fewer microorganisms than water reservoirs, such as rivers and lakes. However, the bio-activities in DWDS are not negligible. The microorganisms in DWDS are generally four categories: bacteria, archaea, eukaryotes, and virus. Bacteria is the most common among the four, thus bacterial biofilm arouses lots of interests and following research. In this section, this dissertation discusses how can the presented multifunctional water sensor avoid the interference from bacteria.

The DWDS bacteria composition in different locations is not consistent, thus it is almost impossibly to generally describe the electrical and physical properties of the DWDS bacterial biofilms. The composition of these microorganisms varies from location to location and season to season. The microorganisms composition is also influenced by the rainfalls, temperature, and many other factors [87], [88]. Thus the bio-organism composition varies year by year even at the same location in the same season. The bacteria composition change can be enormous, for example, the acidovorax ratio in the total bacteria varies from 0 to 40 % in Ann Arbor in just a year [88]. Martiny et al performed a long-term research claiming the biofilm thickness in DWDS is about 25 μm after three years [89], but some claimed this research hardly reflect the real situation in DWDS [87]. Generally the biofilms in DWDS are considered electrically insulating [90], but metal-like conductive biofilms is possible for some species [90], [91]. All in all, since

the composition of the biofilm in DWDS is not consistent in every location, it is almost impossible to predict the biofilm electric properties without the analysis of local bio-film samples.

However, there are some approaches we can do to remove the biofilms from the sensor surface regardless what the species on the biofilms are. The most efficient established method to remove the biofilms in DWDS is chemical treatments, such as chlorine or other strong oxidants. But considering feasibility, high heat and strong electric fields may be the most efficient and approachable methods for our sensor. Research indicates that biofilms are deactivated by putting them in 70-80 ℃ water for 15 to 30 minutes [92] or in around 1000 Vmm^{-1} electric field for 300 pulse [93]. Since the current heavy metal sensors have the same magnitude order of electric field, biofilm may not be possible to attach on the sensor surface. If needed, extra heaters and electrodes can be easily added with little cost. Some research also indicates choosing appropriate substrate materials, such as smooth glass we used in this dissertation, can reduce the formation of biofilms [94].

Based on the research performed in this dissertation, an ideal version of multifunctional water sensor is designed and illustrated in Figure 7.1. The final design includes extra heaters and electric-field electrodes to prevent biofilm formation. The heavy metal sensors are separated from the other sensors, thus the heavy metal sensors can be replaced separately when heavy metals are detected. If needed, the heavy metal sensors and the target conductivity/pH/ORP sensors can be fabricated on silicon wafers instead of the current glass wafer. Silicone wafers have better thermal conductivity, thus are better for thermal cleaning. The flow-rate sensor needs to be on glass wafer to maintain its sensitivity, but extra electrodes can be easily added to provide strong electric fields for cleaning. With these extra electrodes, biofilms should not be a

concern for the temperature, flow-rate, conductivity, and heavy metal sensors. However, the pH and ORP sensors may be interfered by the remaining carbohydrates and protein residues from microorganisms. The other thing should be noted is that the water hardness (calcium and magnesium salts) may precipitate on the sensor surface due to the high heat of thermal cleaning. The water hardness can form a layer that is both thermal and electrical insultaing. This layer may block the thermal transport on flow-rate sensor and the conductive bridge on the heavy metal sensor. Further research on the thermal cleaning is still needed.
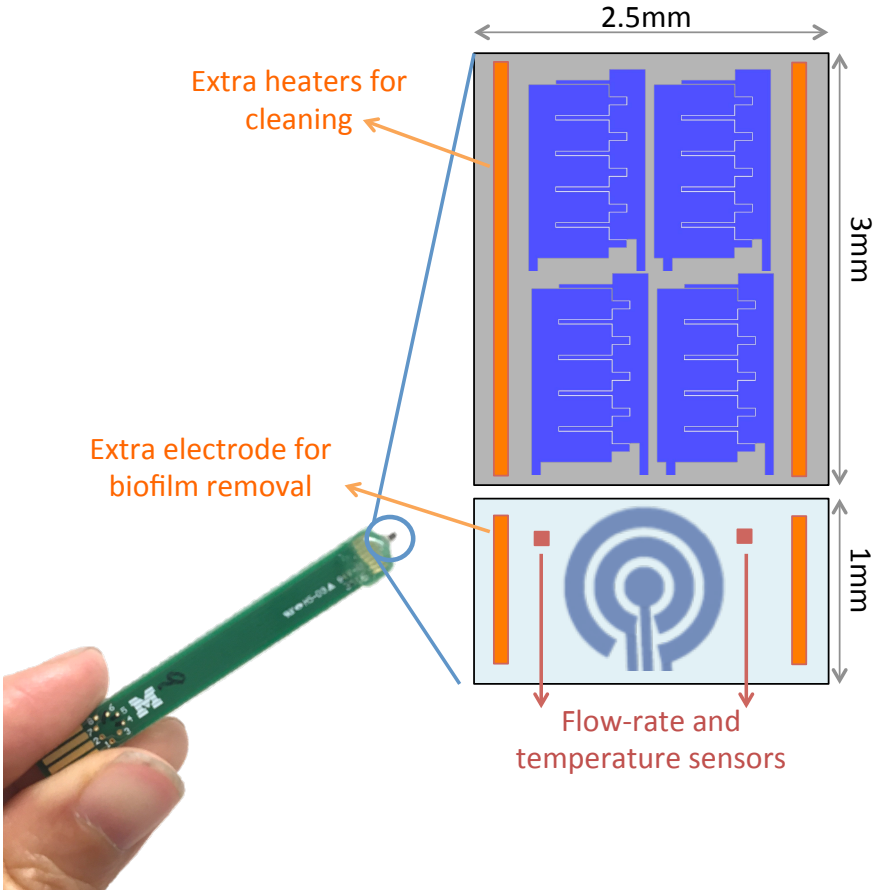
Figure 7.1 Ideal final design of the multifunctional water sensor.

7.3 The Sensor Cost Estimation and Energy Consumption

The estimation of the sensor fabrication cost is only about $0.10 and the PC board cost is $0.50. The PCB was ordered from U&I company of South Korea, and the simple single layer design keeps the cost small. The final integrated sensor are estimated to be around 3 mm by 4 mm, thus more than 800 devices can be fabricated on a 4 in wafer. The cost of the sensor fabrication are listed in Table 7.1, all the cost are calculated with the equipment fee of the LNF lab in University of Michigan. Because of the simple design, the sensors can be fabricated with only one mask and a protection layer on the sensor surface. If we want to produce 14,400 devices (18 wafers) in LNF in a week, with this relatively simple fabrication, each device costs around 10 cents. If fabricated on an industrial-sized 12 in wafer, around 7300 devices can be fabricated per wafer and the cost could be reduced even more.

Table 7.1 Estimation cost of 14,400 devices (18 wafers)

	Items	Cost		Subtotal	Price/device
One-time cost	Chrome Mask Production	$52		$52	$0.0036
	Clean room access/week	$50		$50	$0.0035
	Process name	Cost	Wafers/run	Subtotal	Price/device
	Wafer cost	$7	1	$126	$0.0088
	Lithography	$4	2	$36	$0.0017
Sensor fabrication	PVD	$60	9	$120	$0.0083
	PECVD protection layer	$40	2	$360	$0.0143
	Dicing and integration	$15	1	$270	$0.0188
Labor fee	1.2 hours/ wafer	$40/ hour		$864	$0.0600
Total				$1770	$0.1229

Because the low sensor fabrication cost, the dominant cost of this device is the electronic units including those for energy control and signal reading. Because the operation methods of the flow rate, temperature, and heavy metal sensors are similar to the existed water temperature sensor, the entire electronic module may be able to fabricate at similar cost. All of these sensors read the impedance change across the sensors, and according to our market research listed in Table 7.2, the integrated module for these senor should be able to be fabricated for $5-$20. Extra Bluetooth function may be an extra $2. However, the input energy control for pH/ORP and the conductivity measurement is complicated. The pH/ORP sensor is operated with a very small DC current (0.15 μA), and the conductivity sensor was operated with 6200 Hz 0.5 V square wave and 250 mV offset. All of these operation requirements are challenging to be packed in a small module and further development is necessary to construct robust and affordable electronic units.

Table 7.2 Market research on Bluetooth module and RTD temperature sensor

Category	Item name and series number	Cost
Bluetooth module	NRF51822	$1.92
Integrated water temperature probe	Zacro LCD digital meter	$7.99
	Pentair 520272 with 20-feet cable	$23.85
	URO Parts 9125463	$11.56

Because the significant energy cost and the operation limitation, a plug-in system may be much more suitable than the wireless option. The flow-rate sensor requires 2.75 mW, which equals to 7 kW a month. The heavy metal sensors need 3.2 V, which is a relative high voltage, and two AAA batteries can only supply the heavy metal sensors for about 3 months. Considering

the energy consumption and the need for the input control, we suggest plug-in module may be necessary for commercializing optimization.

7.4 The Contribution of this Dissertation and the Future Direction

This dissertation presents preliminary testing for water quality sensors including flow-rate, temperature, ionic conductivity, pH, ORP, lead, and other heavy metal detection. The results demonstrate possibilities to measure multiple variables with only bare platinum electrodes and without any reference electrode, sample pre-treatment, labeling through chemical reactions, or membrane coating on the sensor surface. The simple structures of these sensors make the sensors cost-efficient, long-lasting, and easy to be integrated. Some of these sensors (pH, ORP, and the heavy metal sensors) are not designed for precise measurement but qualification of water.

For residential water monitoring, contamination-alert by qualification is much more important than precise quantification. Contamination in DWDS often accompanied with sudden decrement of pH, increment of ORP, or the presence of heavy metals ions. The sensors presented in this dissertation are designed to automatically alert users when these situations happen. The contamination-alert sensors presented also satisfy the requirement of practical water monitoring: affordable and long-lasting.

The multifunctional sensors are achieved with both improved previous technology and unique new methods. The heavy metal sensors presented in Chapter 6 and the pH/ORP sensors in Chapter 5 are both very unique methods that are original developed in this dissertation. Both sensors require no specific chemicals to detect certain chemical species. The label-free sensors are achieved by controlling the surface reactions and supplied power on bare platinum electrodes. On the contrast, the thermal flow-rate sensor using RTD and the electrode

conductivity sensor are both studied in previous work of other researchers. This dissertation optimizes both sensors by changing the sensors geometries and the sensor substrates, thus the sensors are ideal for residential water monitoring.

Further research is needed before these sensors can be released for public use. For example, the influence from microorganisms should be studied though theoretically the bacteria biofilm formation can be prevented. Interference from precipitated salts (such as calcium carbonate) in long-term monitoring should also be tested. The pH and ORP measurement should be studied in real samples from different locations to know the influence of major ion concentrations. The response time and sensitivity of the heavy metal sensors can be improved by changing the sensor geometries. In theory, heavy metal sensors with smaller gaps can detect lower concentration in shorter time than the presented sensors. The response time of the heavy metal sensors may also be improved by increasing the length-to-surface-area ratio of the electrodes.

The presented heavy metal sensors and the flow-rate sensor have great possibilities for other applications. Pb sensors with smaller gap may have shorter response time than the current 5-µm-gap sensor, and they may be suitable for Pb concentration range lower than 15 ppb. These improved sensors can be used to detect trace lead in human urine for medical purposes. The heavy metal sensors may also be used for other heavy metal ions detection, such as Cr, Ni, Co, and Hg. The identification between Cr, Cu, and Pb may be improved with precise potential control on the anode. Due to the small feature size, with slight modification, the flow-rate sensor presented in chapter 2 can be used in huge industrial chemical pipes or small micro-channels. The flow sensor is also possible to measure sap flow inside plants. We also have some collaborations working on the applications of the flow-rate sensor: wind speed measurement in

vineyard to prevent the dehydration of plants, and urine flow-rate measurement on flat surfaces to develop a health-monitoring device directly built in the toilet. These applications still need further research but they show the sensors presented in this dissertation have great possibilities.

All in all, this dissertation offers promising results of integrated water sensors measuring seven important variables. Some of the presented sensors are not very precise but have great possibilities for end-point water monitoring and other applications. The major difficulty of water monitoring is to perform long-term qualification under various conditions with little maintenance and small cost. This dissertation presents unique and promising methods to approach the goal.

BIBLIOGRAPHY

[1]   J. Crocker and J. Bartram, "Comparison and Cost Analysis of Drinking Water Quality Monitoring Requirements versus Practice in Seven Developing Countries," Int. J. Environ. Res. Public. Health, vol. 11, no. 7, pp. 7333–7346, Jul. 2014.

[2]   Y. Jeffrey Yang, R. C. Haught, and J. A. Goodrich, "Real-time contaminant detection and classification in a drinking water pipe using conventional water quality sensors: Techniques and experimental results," J. Environ. Manage., vol. 90, no. 8, pp. 2494–2506, Jun. 2009.

[3]   Y. Qin, H.-J. Kwon, M. M. R. Howlader, and M. J. Deen, "Microfabricated electrochemical pH and free chlorine sensors for water quality monitoring: recent advances and research challenges," RSC Adv., vol. 5, no. 85, pp. 69086–69109, Aug. 2015.

[4]   H. Koizumi, "A micro flowmeter based on the measurement of a diffusion temperature rise of a locally heated thermal flow in a Hagen–Poiseuille flow," Flow Meas. Instrum., vol. 34, pp. 19–26, Dec. 2013.

[5]   H. Berthet, J. Jundt, J. Durivault, B. Mercier, and D. Angelescu, "Time-of-flight thermal flowrate sensor for lab-on-chip applications," Lab. Chip, vol. 11, no. 2, pp. 215–223, Jan. 2011.

[6]   A. S. Cubukcu, D. F. R. Romero, and G. A. Urban, "A dynamic thermal flow sensor for simultaneous measurement of thermal conductivity and flow velocity of gases," Sens. Actuators Phys., vol. 208, pp. 73–87, Feb. 2014.

[7]   A. S. Cubukcu, E. Zernickel, U. Buerklin, and G. A. Urban, "A 2D thermal flow sensor with sub-mW power consumption," Sens. Actuators Phys., vol. 163, no. 2, pp. 449–456, Oct. 2010.

[8]   H. Ernst, A. Jachimowicz, and G. A. Urban, "High resolution flow characterization in Bio-MEMS," Sens. Actuators Phys., vol. 100, no. 1, pp. 54–62, Aug. 2002.

[9]   T. H. Kim, D.-K. Kim, and S. J. Kim, "Study of the sensitivity of a thermal flow sensor," Int. J. Heat Mass Transf., vol. 52, no. 7–8, pp. 2140–2144, Mar. 2009.

[10]   S.-C. Roh, Y.-M. Choi, and S.-Y. Kim, "Sensitivity enhancement of a silicon micromachined thermal flow sensor," Sens. Actuators Phys., vol. 128, no. 1, pp. 1–6, Mar. 2006.

[11]   B. Ma, J. Ren, J. Deng, and W. Yuan, "Flexible thermal sensor array on PI film substrate for underwater applications," in 2010 IEEE 23rd International Conference on Micro Electro Mechanical Systems (MEMS), 2010, pp. 679–682.

[12]   M. Shikida, K. Yoshikawa, S. Iwai, and K. Sato, "Flexible flow sensor for large-scale

air-conditioning network systems," Sens. Actuators Phys., vol. 188, pp. 2–8, Dec. 2012.

[13]   M. Shikida, Y. Yamazaki, K. Yoshikawa, and K. Sato, "A MEMS flow sensor applied in a variable-air-volume unit in a building air-conditioning system," Sens. Actuators Phys., vol. 189, pp. 212–217, Jan. 2013.

[14]   R.-H. Ma, D.-A. Wang, T.-H. Hsueh, and C.-Y. Lee, "A MEMS-Based Flow Rate and Flow Direction Sensing Platform with Integrated Temperature Compensation Scheme," Sensors, vol. 9, no. 7, pp. 5460–5476, Jul. 2009.

[15]   O. S. Aleksic, M. V. Nikolic, M. D. Lukovic, S. O. Aleksic, and P. M. Nikolic, "Analysis and optimization of a thermal sensor system for measuring water flow," Sens. Actuators Phys., vol. 201, pp. 371–376, Oct. 2013.

[16]   F. Laugere, G. W. Lubking, A. Berthold, J. Bastemeijer, and M. J. Vellekoop, "Downscaling aspects of a conductivity detector for application in on-chip capillary electrophoresis," Sens. Actuators Phys., vol. 92, no. 1–3, pp. 109–114, Aug. 2001.

[17]   P. M. Ramos, J. M. D. Pereira, H. M. G. Ramos, and A. L. Ribeiro, "A Four-Terminal Water-Quality-Monitoring Conductivity Sensor," IEEE Trans. Instrum. Meas., vol. 57, no. 3, pp. 577–583, Mar. 2008.

[18]   A. J. Fougere, "New non-external field inductive conductivity sensor (NXIC) for long term deployments in biologically active regions," in OCEANS 2000 MTS/IEEE Conference and Exhibition. Conference Proceedings (Cat. No.00CH37158), 2000, vol. 1, pp. 623–630 vol.1.

[19]   J. G. Webster, The Measurement, Instrumentation and Sensors Handbook. CRC Press, 1998.

[20]   M. W. Shinwari, D. Zhitomirsky, I. A. Deen, P. R. Selvaganapathy, M. J. Deen, and D. Landheer, "Microfabricated Reference Electrodes and their Biosensing Applications," Sensors, vol. 10, no. 3, pp. 1679–1715, Mar. 2010.

[21]   T. Y. Kim, S. A. Hong, and S. Yang, "A Solid-State Thin-Film Ag/AgCl Reference Electrode Coated with Graphene Oxide and Its Use in a pH Sensor," Sensors, vol. 15, no. 3, pp. 6469–6482, Mar. 2015.

[22]   B. Huber and B. Roling, "Development of a Ag/Ag+ micro-reference electrode for electrochemical measurements in ionic liquids," Electrochimica Acta, vol. 56, no. 19, pp. 6569–6572, Jul. 2011.

[23]   R. Mamińska, A. Dybko, and W. Wróblewski, "All-solid-state miniaturised planar reference electrodes based on ionic liquids," Sens. Actuators B Chem., vol. 115, no. 1, pp. 552–557, May 2006.

[24]   P. J. Kinlen, J. E. Heider, and D. E. Hubbard, "A solid-state pH sensor based on a Nafion-coated iridium oxide indicator electrode and a polymer-based silver chloride reference electrode," Sens. Actuators B Chem., vol. 22, no. 1, pp. 13–25, Oct. 1994.

[25]   H. Yang et al., "An iridium oxide reference electrode for use in microfabricated biosensors and biochips," Lab. Chip, vol. 4, no. 1, pp. 42–46, Feb. 2004.

[26]   J. Noh, S. Park, H. Boo, H. C. Kim, and T. D. Chung, "Nanoporous platinum solid-state reference electrode with layer-by-layer polyelectrolyte junction for pH sensing chip," Lab. Chip, vol. 11, no. 4, pp. 664–671, Feb. 2011.

[27]   "Focused ion beam generated antimony nanowires for microscale pH sensors," Appl. Phys. Lett., vol. 95, no. 22, p. 223106, Nov. 2009.

[28]   W.-D. Huang, H. Cao, S. Deb, M. Chiao, and J. C. Chiao, "A flexible pH sensor based on the iridium oxide sensing film," Sens. Actuators Phys., vol. 169, no. 1, pp. 1–11,

Sep. 2011.

[29]   S. O. Belostotskaya, O. V. Chuyko, A. E. Kuznetsov, E. V. Kuznetsov, and E. N. Rybachek, "Silicon nanowire structures as high-sensitive pH-sensors," J. Phys. Conf. Ser., vol. 345, no. 1, p. 12008, 2012.

[30]   S. Choi, I. Park, Z. Hao, H.-Y. N. Holman, and A. P. Pisano, "Quantitative studies of long-term stable, top-down fabricated silicon nanowire pH sensors," Appl. Phys. A, vol. 107, no. 2, pp. 421–428, May 2012.

[31]   I. Park, Z. Li, A. P. Pisano, and R. S. Williams, "Top-down fabricated silicon nanowire sensors for real-time chemical detection," Nanotechnology, vol. 21, no. 1, p. 15501, 2010.

[32]   Y. T. Lee, E. Lee, J. M. Lee, and W. Lee, "Micro-sized pH sensors based on patterned Pd structures using an electrolysis method," Curr. Appl. Phys., vol. 9, no. 4, Supplement, pp. e218–e221, Jul. 2009.

[33]   W. S. Lee, Y.-S. Park, and Y.-K. Cho, "Hierarchically Structured Suspended TiO2 Nanofibers for Use in UV and pH Sensor Devices," ACS Appl. Mater. Interfaces, vol. 6, no. 15, pp. 12189–12195, Aug. 2014.

[34]   K. P. K. Olympio, C. Gonçalves, W. M. R. Günther, and E. J. H. Bechara, "Neurotoxicity and aggressiveness triggered by low-level lead in children: a review," Rev. Panam. Salud Pública, vol. 26, no. 3, pp. 266–275, Sep. 2009.

[35]   B. P. Lanphear, K. Dietrich, P. Auinger, and C. Cox, "Cognitive deficits associated with blood lead concentrations <10 microg/dL in US children and adolescents," Public Health Rep. Wash. DC 1974, vol. 115, no. 6, pp. 521–529, Dec. 2000.

[36]   S. Triantafyllidou and M. Edwards, "Lead (Pb) in Tap Water and in Blood: Implications for Lead Exposure in the United States," Crit. Rev. Environ. Sci. Technol., vol. 42, no. 13, pp. 1297–1352, Jul. 2012.

[37]   M. Kumar and A. Puri, "A review of permissible limits of drinking water," Indian J. Occup. Environ. Med., vol. 16, no. 1, p. 40, Apr. 2012.

[38]   O. US EPA, "Table of Regulated Drinking Water Contaminants." [Online]. Available: https://www.epa.gov/ground-water-and-drinking-water/table-regulated-drinking-water-contaminants. [Accessed: 18-Jan-2017].

[39]   O. US EPA, "Secondary Drinking Water Standards: Guidance for Nuisance Chemicals." [Online]. Available: https://www.epa.gov/dwstandardsregulations/secondary-drinking-water-standards-guidance-nuisance-chemicals. [Accessed: 18-Jan-2017].

[40]   R. Levin et al., "Lead Exposures in U.S. Children, 2008: Implications for Prevention," Environ. Health Perspect. Res. Triangle Park, vol. 116, no. 10, pp. 1285–93, Oct. 2008.

[41]   A. Dudi, M. Schock, N. Murray, and M. Edwards, "Lead leaching from inline brass devices: A critical evaluation of the existing standard," Am. Water Works Assoc. J. Denver, vol. 97, no. 8, p. 66–78,12, Aug. 2005.

[42]   Y. S. Tam and P. Elefsiniotis, "Corrosion control in water supply systems: Effect of pH, alkalinity, and orthophosphate on lead and copper leaching from brass plumbing," J. Environ. Sci. Health Part A, vol. 44, no. 12, pp. 1251–1260, Sep. 2009.

[43]   S. Laschi, I. Palchetti, and M. Mascini, "Gold-based screen-printed sensor for detection of trace lead," Sens. Actuators B Chem., vol. 114, no. 1, pp. 460–465, Mar. 2006.

[44]   J. Wang and B. Tian, "Mercury-free disposable lead sensors based on potentiometric

stripping analysis of gold-coated screen-printed electrodes," Anal. Chem., vol. 65, no. 11, pp. 1529–1532, 1993.

[45]   M. Guziński, G. Lisak, J. Kupis, A. Jasiński, and M. Bocheńska, "Lead(II)-selective ionophores for ion-selective electrodes: A review," Anal. Chim. Acta, vol. 791, pp. 1–12, Aug. 2013.

[46]   M.-R. Huang, Y.-B. Ding, and X.-G. Li, "Combinatorial Screening of Potentiometric Pb(II) Sensors from Polysulfoaminoanthraquinone Solid Ionophore," ACS Comb. Sci., vol. 16, no. 3, pp. 128–138, Mar. 2014.

[47]   Y.-L. Hung, T.-M. Hsiung, Y.-Y. Chen, and C.-C. Huang, "A label-free colorimetric detection of lead ions by controlling the ligand shells of gold nanoparticles," Talanta, vol. 82, no. 2, pp. 516–522, Jul. 2010.

[48]   W. Chu, Y. Zhang, D. Li, C. J. Barrow, H. Wang, and W. Yang, "A biomimetic sensor for the detection of lead in water," Biosens. Bioelectron., vol. 67, pp. 621–624, May 2015.

[49]   R. Mohd and A. Nur, "Sensors for Detecting Heavy Metals," WO/2013/141692, 27-Sep-2013.

[50]   D. N. Pagonis, G. Kaltsas, and A. G. Nassiopoulou, "Fabrication and testing of an integrated thermal flow sensor employing thermal isolation by a porous silicon membrane over an air cavity," J. Micromechanics Microengineering, vol. 14, no. 6, p. 793, 2004.

[51]   P. Bruschi, D. Navarrini, and M. Piotto, "A flow sensor for liquids based on a single temperature sensor operated in pulsed mode," Sens. Actuators Phys., vol. 110, no. 1–3, pp. 269–275, Feb. 2004.

[52]   N. Okulan, H. T. Henderson, and C. H. Ahn, "A pulsed mode micromachined flow sensor with temperature drift compensation," IEEE Trans. Electron Devices, vol. 47, no. 2, pp. 340–347, Feb. 2000.

[53]   J. Janouš, P. Beránek, M. Přibyl, and D. Šnita, "Development of a conductivity microsensor considering electric double layer capacity," Microelectron. Eng., vol. 97, pp. 387–390, Sep. 2012.

[54]   M. Hayashi, "Temperature-electrical conductivity relation of water for environmental monitoring and geophysical data inversion," Environ. Monit. Assess., vol. 96, no. 1, pp. 119–128, 2004.

[55]   D. A. Stern et al., "Characterization of single-crystal electrode surfaces as a function of potential and pH by Auger spectroscopy and LEED: Pt (111) in aqueous CaCl2 and HCl solutions," J. Electroanal. Chem. Interfacial Electrochem., vol. 217, no. 1, pp. 101–110, Jan. 1987.

[56]   E. Zoulias, E. Varkaraki, N. Lymberopoulos, C. N. Christodoulou, and G. N. Karagiorgis, "A review on water electrolysis," TCJST, vol. 4, no. 2, pp. 41–71, 2004.

[57]   S. A. Vilekar, I. Fishtik, and R. Datta, "Kinetics of the Hydrogen Electrode Reaction," J. Electrochem. Soc., vol. 157, no. 7, pp. B1040–B1050, Jul. 2010.

[58]   N. Li and J. Lipkowski, "Chronocoulometric studies of chloride adsorption at the Pt(111) electrode surface," J. Electroanal. Chem., vol. 491, no. 1–2, pp. 95–102, Sep. 2000.

[59]   N. Garcia-Araez, V. Climent, E. Herrero, J. M. Feliu, and J. Lipkowski, "Determination of the Gibbs excess of H adsorbed at a Pt(1 1 1) electrode surface in the presence of co-adsorbed chloride," J. Electroanal. Chem., vol. 582, no. 1–2, pp.

76–84, Aug. 2005.

[60]   "Adsorption of Na+ and Cl− at the charged water–platinum interface," J. Chem. Phys., vol. 98, no. 3, pp. 2283–2290, Feb. 1993.

[61]   C. A. Lucas, N. M. Markovic-acute, and P. N. Ross, "Adsorption of halide anions at the Pt (111)-solution interfacestudied by in situ surface x-ray scattering," Phys. Rev. B, vol. 55, no. 12, p. 7964, 1997.

[62]   Electrochemistry - The Basics, With Examples | Christine Lefrou | Springer. .

[63]   D. R. Lide and W. M. Haynes, CRC handbook of chemistry and physics: a ready-reference book of chemical and physical data. Boca Raton, Fla.: CRC Press, 2009.

[64]   M. D. Arning and S. D. Minteer, "18 - Electrode Potentials," in Handbook of Electrochemistry, C. G. Zoski, Ed. Amsterdam: Elsevier, 2007, pp. 813–827.

[65]   J. K. Nørskov et al., "Origin of the Overpotential for Oxygen Reduction at a Fuel-Cell Cathode," J. Phys. Chem. B, vol. 108, no. 46, pp. 17886–17892, Nov. 2004.

[66]   A. Hickling and W. H. Wilson, "Increase of Oxygen Overpotential at a Platinum Anode by Reducing Agents," Nature, vol. 164, pp. 673–673, Oct. 1949.

[67]   Principles of Physics – Saunders Golden Sunburst Series [Saunders College Publishing: Second edition]. .

[68]   S. G. Bratsch, "Standard Electrode Potentials and Temperature Coefficients in Water at 298.15 K," J. Phys. Chem. Ref. Data, vol. 18, no. 1, pp. 1–21, Jan. 1989.

[69]   X. Li, D. Pletcher, and F. C. Walsh, "Electrodeposited lead dioxide coatings," Chem. Soc. Rev., vol. 40, no. 7, p. 3879, 2011.

[70]   J. P. Carr and N. A. Hampson, "Lead dioxide electrode," Chem. Rev., vol. 72, no. 6, pp. 679–703, 1972.

[71]   A. Azoulay, P. Garzon, and M. J. Eisenberg, "Comparison of the Mineral Content of Tap Water and Bottled Waters," J. Gen. Intern. Med., vol. 16, no. 3, pp. 168–175, Mar. 2001.

[72]   C. E. Harvie, N. Møller, and J. H. Weare, "The prediction of mineral solubilities in natural waters: The Na-K-Mg-Ca-H-Cl-SO4-OH-HCO3-CO3-CO2-H2O system to high ionic strengths at 25 C," Geochim. Cosmochim. Acta, vol. 48, no. 4, pp. 723–751, 1984.

[73]   S. L. Goss, K. A. Lemons, J. E. Kerstetter, and R. H. Bogner, "Determination of calcium salt solubility with changes in pH and P CO2 , simulating varying gastrointestinal environments," J. Pharm. Pharmacol., vol. 59, no. 11, pp. 1485–1492, Nov. 2007.

[74]   S. Teir, S. Eloneva, C.-J. Fogelholm, and R. Zevenhoven, "Stability of calcium carbonate and magnesium carbonate in rainwater and nitric acid solutions," Energy Convers. Manag., vol. 47, no. 18–19, pp. 3059–3068, Nov. 2006.

[75]   W. Stumm and G. F. Lee, "The chemistry of aqueous iron," Schweiz. Z. Für Hydrol., vol. 22, no. 1, pp. 295–319, 1960.

[76]   J. O. Bockris, D. Drazic, and A. R. Despic, "The electrode kinetics of the deposition and dissolution of iron," Electrochimica Acta, vol. 4, no. 2–4, pp. 325–361, Aug. 1961.

[77]   M. Cohen and K. Hashimoto, "The Cathodic Reduction of Gamma-FeOOH, Gamma-Fe2 O 3, and Oxide Films on Iron," J. Electrochem. Soc., vol. 121, no. 1, pp. 42–45, 1974.

[78]   P. H. Holloway, "Fundamentals and Applications of Auger Electron Spectroscopy," in Advances in Electronics and Electron Physics, vol. 54, L. M. and C. Marton, Ed.

Academic Press, 1980, pp. 241–298.

[79]   "Quantitative Auger electron spectroscopy using elemental sensitivity factors," J. Vac. Sci. Technol., vol. 13, no. 1, pp. 214–218, Jan. 1976.

[80]   F. Peeters and A. J. Slavin, "A comparison between the oxidation of bulk lead and that of lead deposits on Au(111): An auger study," Surf. Sci., vol. 214, no. 1–2, pp. 85–96, Apr. 1989.

[81]   C. Argile, "Chemical effects in the Auger spectrum of lead, deposited on nickel oxide––an indirect characterization of the NiO growth mode on Ni(1 0 0)," Surf. Sci., vol. 517, no. 1–3, pp. 1–7, Oct. 2002.

[82]   Charles Kittel-8th Edition, Introduction to Solid State Physics. .

[83]   P. Vikas, J. Pradeep, C. Manik, and S. Shashwati, "Synthesis and Characterization of Co3O4Thin Film," Soft Nanosci. Lett., vol. 2012, Dec. 2011.

[84]   "Production and magnetotransport properties of CrO2 films," J. Appl. Phys., vol. 81, no. 8, pp. 5774–5776, Apr. 1997.

[85]   M. Guziewicz et al., "Electrical and optical properties of NiO films deposited by magnetron sputtering," Opt. Appl., vol. Vol. 41, no. nr 2, 2011.

[86]   N. E. Makori et al., "Optical and Electrical Properties of CdO: Sn Thin Films for Solar Cell Applications," Int. J. Optoelectron. Eng., vol. 4, no. 1, pp. 11–15, 2014.

[87]   K. Fish, "The Impact of Hydraulic Regime upon Biofilms in Drinking Water Distribution Systems," phd, University of Sheffield, 2013.

[88]   A. J. Pinto, J. Schroeder, M. Lunn, W. Sloan, and L. Raskin, "Spatial-Temporal Survey and Occupancy-Abundance Modeling To Predict Bacterial Community Dynamics in the Drinking Water Microbiome," mBio, vol. 5, no. 3, pp. e01135-14, Jul. 2014.

[89]   A. C. Martiny, T. M. Jørgensen, H.-J. Albrechtsen, E. Arvin, and S. Molin, "Long-Term Succession of Structure and Diversity of a Biofilm Formed in a Model Drinking Water Distribution System," Appl. Environ. Microbiol., vol. 69, no. 11, pp. 6899–6907, Nov. 2003.

[90]   X. Muñoz-Berbel, F. J. Muñoz, N. Vigués, and J. Mas, "On-chip impedance measurements to monitor biofilm formation in the drinking water distribution network," Sens. Actuators B Chem., vol. 118, no. 1–2, pp. 129–134, Oct. 2006.

[91]   N. S. Malvankar et al., "Tunable metallic-like conductivity in microbial nanowire networks," Nat. Nanotechnol., vol. 6, no. 9, pp. 573–579, Sep. 2011.

[92]   H.-C. Flemming, "Biofouling in water systems--cases, causes and countermeasures," Appl. Microbiol. Biotechnol., vol. 59, no. 6, pp. 629–640, Sep. 2002.

[93]   S. I. Khan et al., "Eradication of multidrug-resistant pseudomonas biofilm with pulsed electric fields," Biotechnol. Bioeng., vol. 113, no. 3, pp. 643–650, Mar. 2016.

[94]   N. B. Hallam, J. R. West, C. F. Forster, and J. Simms, "The potential for biofilm growth in water distribution systems," Water Res., vol. 35, no. 17, pp. 4063–4071, Dec. 2001.